HIGH POROSITY REDUCED GRAPHENE OXIDE ELECTRODE PREPARED BY LANGMUIR-BLODGETT TECHNIQUE FOR APPLICATION IN BIO-PHOTOVOLTAICS

MUHAMMAD MUSODDIQ BIN JAAFAR

FACULTY OF SCIENCE
UNIVERSITY OF MALAYA
KUALA LUMPUR

2017

HIGH POROSITY REDUCED GRAPHENE OXIDE ELECTRODE PREPARED BY LANGMUIR-BLODGETT TECHNIQUE FOR APPLICATION IN BIO-PHOTOVOLTAICS

MUHAMMAD MUSODDIQ BIN JAAFAR

THESIS SUBMITTED IN FULFILLMENT OF THE REQUIREMENT OF THE DEGREE OF MASTER OF SCIENCE

DEPARTMENT OF PHYSICS
FACULTY OF SCIENCE
UNIVERSITY OF MALAYA
KUALA LUMPUR

2017

UNIVERSITI MALAYA

ORIGINAL LITERARY WORK DECLARATION

Name of Candidate: **Muhammad Musoddiq Bin Jaafar**

Registration / Matric No.: **SGR130079**

Name of Degree: **Master of Science**

Title of Project Thesis:

HIGH POROSITY REDUCED GRAPHENE OXIDE ELECTRODE PREPARED BY LANGMUIR-BLODGETT TECHNIQUE FOR APPLICATION IN BIO-PHOTOVOLTAICS

Field of Study: **Experimental Physics**

I do solemnly and sincerely declare that:

(1) I am the sole author/writer of this Work;
(2) This Work is original;
(3) Any use of any work in which copyright exist was done by way of fair dealing and for permitted purposes and any excerpt or extract from, or reference to or reproduction of any copyright work has been disclosed expressly and sufficiently and the title of the Work and its authorship have been acknowledged in this Work;
(4) I do not have any actual knowledge nor do I ought reasonably to know that the making of this work constitutes an infringement of any copyright work;
(5) I hereby assign all every rights in the copyright to this Work to the University of Malaya ("UM"), who henceforth shall be owner of the copyright in this Work and that any reproduction or use in any form or by any means whatsoever is prohibited without the written consent of UM having been first had and obtained;
(6) I am fully aware that if in the course of making this Work I have infringed any copyright whether intentionally or otherwise, I may be subject to legal action or any other action as may be determined by UM.

Candidate's Signature: Date:

Subscribed and solemnly declared before,

Witness's Signature: Date:

Name:

Designation:

ABSTRACT

Traditional Langmuir-Blodgett (LB) method has proven versatile in fabrication of two-dimensional (2D) film structures of thin films. This thesis meanwhile presents a study of developing three-dimensional (3D) structures of functional materials using unconventional LB methodologies. A detailed discussion of how 3D thin films of reduced Graphene Oxide (rGO) can be fabricated using dipping process post collapse pressure or breaking point, thus providing highly porous 3D surface topographies. Porosity could be optimized from nanometer to micrometer dimensions by varying the number of deposition with constant pressure. The 3D rGO thin film has been studied in applications for microbial fuel cells (MFCs) to provide improved biofilm formation and biocompatibility compared with the traditional 2D surfaces used as bioelectrodes. Furthermore, the inherent porosity of the deposited rGO films also improves the mass transport of materials; hence increase the charge-sustaining capacity and sensitivity. It was shown that the sixth deposition of rGO allowed the film to gain pore sizes between 1.2 to 3.8 μm, which is similar to the size of algae (2.0 – 3.5 μm). This feature of the rGO film accommodates an ideal surface for the anchoring of algae cells within the pores increasing surface contact and improves electron transfer efficiency. The rGO-algae thin film as electrodes in biophotovoltaic (BPV) systems have been studied and higher efficiency reported due to its intrinsic electrical properties and biological compatibility.

ABSTRAK

Kaedah tradisional Langmuir-Blodgett (LB) telah membuktikan ianya sinonim dengan kebolehan fabrikasi filem nipis yang berstruktur dua dimensi. Tetapi, tesis ini membentangkan hasil kajian mengenai pembangunan struktur tiga dimensi (3D) untuk bahan fungsian dengan menggunakan teknik LB yang tidak lazim buat kali pertama. Penerangan secara teliti mengenai bagaimana filem nipis 3D Graphene Penurunan Oksida (GPO) telah dihasilkan dengan melakukan mekanisma salutan celup selepas tekanan runtuh atau titik pecah, seterusnya menghasilkan keliangan tinggi di permukaan topografi tiga dimensi. Keliangan filem ini dapat dikawal daripada saiz nanometer kepada mikrometer dengan membezakan jumlah mendapan dengan tekanan malar. Filem nipis tiga dimensi GPO telah diukaji sebagai bioelektrod di dalam aplikasi bahan api mikrob bagi meningkatkan formasi filem-biologi dan keserasian biologi berbanding permukaan filem nipis dua dimensi. Seterusnya, kewujudan keliangan oleh GPO dapat meningkatkan pengangkutan jisim bahan dan meningkatkan kapasiti dan sensitiviti caj elektrik yang lebih mapan. Juga, enam lapisan pemendapan GPO filem nipis mempunyai saiz liang (1.2 – 3.8 μm), dan ianya hampir sama dengan saiz alga (2.0 – 3.5 μm). Oleh kerana persamaan ini, filem nipis tiga dimensi GPO menyediakan permukaan ideal untuk alga bertaut dan menetap di dalam liang dan meningkatkan sentuhan permukaan bagi meningkatkan kecekapan permindahan elektron. GPO-alga filem nipis sebagai elektrod di dalam sistem biofotovolta telah dikaji dan dilaporkan memberi kecekapan yang lebih tinggi kerana disebabkan oleh sifat elektrik intrinsik dan keserasian bahan biologi.

ACKNOWLEDGEMENTS

I would like to express my gratitude and thank you to my family especially my mother, Rosmawati binti Ghazali, who continuously inspired, encouraged and supported me in every single moment I have gone through in my whole life. It is really valuable not only just having their financial assistance, but constantly receiving moral and spiritual support as well. Not to forget to mention my wife, Ili Nur'Izzati binti Abdul Rahman who has been there for me through thick and thin in the journey and adventure towards completion of my master's degree.

This great opportunity has been given to me by my supervisor, Assoc. Prof. Dr. Vengadesh Periasamy, and my co-supervisor, Dr. Kamran Yunus, who receives my utmost grateful acknowledgement for what I have achieved until now. They have put their own sweat for me and other group members in providing us guidance, support, and concern until the completion of this work. Special thanks to Prof. Dr. Phang Siew Moi, Dr. Victoria Ng Fong Lee, Mr. Chris Chan Zhijian, Ms. Siti Aisyah Ibrahim, and other group members and mentors.

I also would like to express my thank you to my lab members who have always helped me in my theoretical studies and experimental work. They are Ms. Mazlinda Zainy, Ms. Nor Khairiah, Mr. Syed Hafiz, Mr. Shahino Mah, and Ms. Siti Hajar Basri. Low Dimensional Materials Research Centre (LDMRC) staffs, Mr. Mohamad Aruf, Mrs. Norlela Mohd Shahardin, and Mr. Mohd Arif Mohd Sarjidan, thanks for the administrative assistance that has eased my task in the laboratory.

Furthermore, I would like to thank LDMRC, Institute of Ocean and Earth Science (IOES), Institute of Biological Sciences (ISB), from University Malaya, and Centre for Research in Electrochemical Science and Technology (CREST) Department of Chemical

Engineering and Biotechnology, University of Cambridge for providing me the facilities to do my research.

It is very priceless to have financial assistance for my research work granted from the Postgraduate Research Grant (PG111-2014A), and most importantly for my research assistantship from my supervisor's grants, including those with project number RG321-15AFR, FP004-2013A, KPT1059-2012, and HIR: J-21002-73823.

Last but not least, thank you so much to anyone who I did not mention their names here for any direct or indirect contributions until the completion of my research work.

TABLE OF CONTENTS

LIST OF FIGURES

LIST OF SYMBOLS

A	Absorbance
I	Ampere
A	Area
cm	Centimetre
K	Compression Modulus
$\|E\|$	Gibbs Elasticity
I	Intensity
F	Intermolecular Force
μm	Micrometer
mm	Millimetre
Ω	Ohm
pH	Potential of Hydrogen
R	Reflection
μ	Room Temperature Mobility
s	Seconds
ρ_s	Sheet Resistance
π	Surface Pressure
γ	Surface Tension
sq	Square
T	Transmission
V	Voltage
w	Wavenumber

LIST OF ABBREVIATIONS

AEM	Anion-Exchange Membrane
AFM	Atomic Force Microscopy
BESs	Bioelectrochemical Systems
BPV	Biophotovoltaics
CNT	Carbon Nanotube
CEM	Cation-Exchange Membrane
CV	Cyclic Voltammetry
DI	Dionized
EFC	Enzymatic Fuel Cell
FESEM	Field Emission Scanning Electron Microscope
FOM	Forward Osmosis Membrane
FC	Fuel Cells
GPO	Grafin Penurunan Oksida
GO	Graphene Oxide
HOMO	Highest Occupied Molecular Orbital
ITO	Indium Thin Oxide
kWp	Kilowatts
LB	Langmuir-Blodgett
LUMO	Lowest Unoccupied Molecular Orbital
MDC	Microbial Desalination Cell
MEC	Microbial Electrolysis Cell
MFCs	Microbial Fuel Cells
MSC	Microbial Solar Cell
PSII	Photosystem II
PDMS	Polydimethylsiloxane

PEM	Proton Exchange Membrane
QD	Quantum Dots
QHE	Quantum Hall Effect
rGO	Reduced Graphene Oxide
SHE	Standard Hydrogen Electrode
SEM	Scanning Electron Microscope
SEP	Standard Electrode Potential
3D	Three-dimensional
TFCs	Transparent Conductive Films
2D	Two-dimensional
UMACC	University of Malaya Algae Culture Collection

CHAPTER 1

INTRODUCTION

1.1 A Brief Introduction of Biophotovoltaics

It is well understood that the limitless supply offered by solar radiation has the potential to fulfil energy demand in the future (Almasoud et al., 2015; Burnett et al., 2014; Kannan et al., 2016; Sindhu et al., 2016). This has emboldened scientists to develop strategies and technologies to enable the harvesting of energy from the sun (Kannan et al., 2016). A variety of technologies have been introduced to convert solar radiation into energy, which includes photovoltaics (El Chaar et al., 2011; Mazzio et al., 2015; Parida et al., 2011), solar heating-cooling (Lake et al., 2017; Mugnier et al., 2015) and concentrating solar power (Kandilli et al., 2017; Vieira De Souza et al., 2016). Conversion of solar radiation into energy by using solar heating and cooling can be described as the process of collecting solar energy from the sun and convert it into thermal energy by using solar roof collector, solar chimney, Trombe wall, and others (Chan et al., 2010). It is typically to provide thermal energy for hot water, space heating, and pool heating for residential, commercial and industrial applications (Chan et al., 2010). This technology is used to save electricity and natural gas for heating (Lake et al., 2017). The concentrating solar power is referred to as concentrating solar radiation into small area by using mirror or lens (Liu et al., 2016). The concentrated solar radiation will heat up the fluid in solar power plant and move the steam turbine to generate electricity (Lake et al., 2017). In addition, the heat collected can also be stored in either sensible, latent, or thermochemical storage (Liu et al., 2016).

Photovoltaics mechanism can be explained by the photovoltaics effect. Energy from photons are absorbed, ejecting the electron from lower-energy state to higher-energy state that allows them to act as carrier charge for electric current (Zambari et al., 2013). The photovoltaics solar generation system may contain multiple components such as solar cells, mechanical and electrical connection, mounting, and more. The part is important to regulate or modify the electrical output of the systems. These system is rated in peak kilowatts (kWp), meaning the amount of electrical power that a system is estimated to deliver when solar radiation is directly overhead on a clear day (Parida et al., 2011).

In recent times, the development of methodologies for converting solar radiation to energy is rapidly transforming and the need to understand and mimic how nature has evolved to harvest solar energy is becoming increasingly important (Bradley et al., 2012). This is because it offers the possibilities of inexpensive light energy capture technologies. In addition, it also comes with the added benefits of being carbon-neutral to produce and run (or possibly even carbon-negative if biomass is harvested and sequestered), and having natural ability to store energy (Mccormick et al., 2015). The inherent abilities of certain microorganisms for exoelectrogenic activity, which is a direct and/or indirect electron transfer outside the cell membrane has prompted the development of a range of technology platforms to generate electrical power (Logan, 2009; Mccormick et al., 2015). The use of metabolic activity of theses certain types of microorganisms have led to the potential means for energy harvesting in fuel cells (FC) becoming the pioneer in the development of microbial fuel cells (MFCs) (Bombelli et al., 2011). The potential of exploiting photosynthetic microorganisms in MFCs have given rise to a novel class of technology known as biophotovoltaics (BPV). The principle behind BPV-based-devices is producing electricity from light energy via light-harvesting apparatus of photosynthetic organisms, instead of traditional MFCs, which requires a carbon source fed to the microorganisms to generate electricity (Mao et al., 2013).

Figure 1.1 provides a schematic illustrating the working principles behind a typical BPV device. The capture of light in photosynthesis leads to the process of water splitting into oxygen, protons and electrons. During this process any electrons captured at the anode surface can be transferred to the cathode surface due to a potential difference setup between the two electrodes (Mccormick et al., 2015). In order to advance higher power output in BPV systems, a mechanism for reducing internal potential losses and internal resistance has to be developed. Furthermore, effective electrochemical communication between the biological component and the anode surface is essential. Recent studies of biofilm formation at the anode surface have allowed the possibilities to increase the power output by reducing the internal potential energy losses due to the direct contact between cell and electrode (Ng et al., 2014; Sauer et al., 2007).

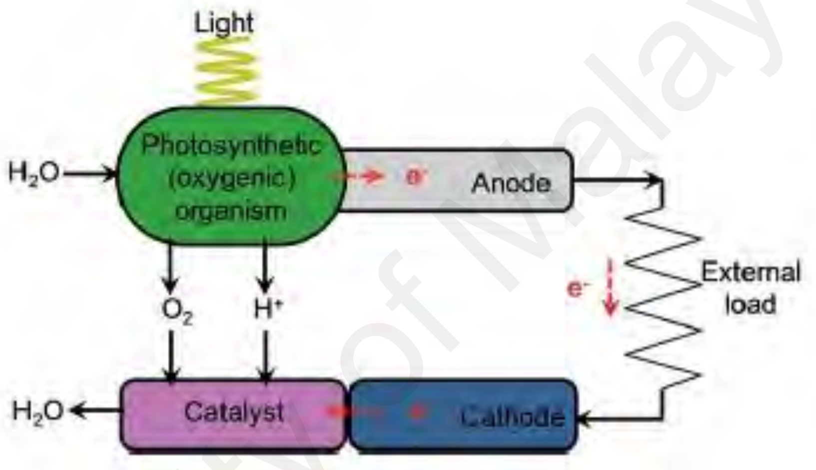

Figure 1.1: Biophotovoltaics System (Mccormick et al., 2015).

1.2 Motivations and Objectives

The demand for energy has increased with continuing growth in technology and human population. Current global population of 7.3 billion is predicted to reach 11.2 billion by 2100 (Berker, 2015). Hence, global energy demand will be increased by 37% between 2013 to 2035 (Dudley, 2015), and can no longer be sustained by fossil fuels such as coal, petroleum, and natural gas. Despite having many alternative renewable energy solutions, the cost in terms of specific construction and energy generation is far higher compared with the conventional resources such as fossil fuels (Sovacool, 2010). Furthermore, renewable energy solutions come with a number of added complications such as irregular production and in some cases requirements for large areas of arable land (Keong et al., 2008; Li, 2007). Therefore, organizations, governments, and corporations have intensive research initiatives for a more effective, efficient green power plants, clean fuel technology and novel green energy sources (Sovacool, 2010). In addition, the increasing costs and limited supply of fossil fuels and renewable energy require the development of sustainable secure energy markets that can define a balanced techno-economic model.

Over the centuries, nature has evolved to develop highly efficient means for harvesting and cultivating solar radiation. Exoelectrogenic behaviour found in microorganisms and plants have led to the development of a range of devices based on electrochemical technologies. The ability of exoelectrogenic bacteria to have redox activity close to its cell wall have lead to the development of a range of devices such as microbial fuel cells and photosynthetic MFCs. Current studies of photosynthetic MFCs have shown poor device performance, which have been mainly due to certain limitations in the device design and choice of electrode material for the anode surface. In this report a detailed study of algae biofilms formed on a range of anode surfaces will be investigated. In particular the use of functionalised rGO surfaces will be compared with ITO electrodes, to observe if improved biofilms formed on rGO could lead to a lower internal resistance in the device and ultimately a more efficient photomicrobial fuel cell device.

From previous studies, surface topography has proven to play an essential role in biocompatibility and cell efficiency (Bobyn et al., 1982; Brauker et al., 1995; Singhvi et al., 1994). Thus, a method for re-engineering surface profile at molecular level is needed to provide an enhanced topography for the algae biofilm formation. In this report, a thorough study of how Langmuir-Blodgett (LB) techniques can be used to create homogeneous and controlled rGO film techniques on a molecular level will be reported (Schwartz, 1997).

The objectives of this research are divided into three parts.

(i) To obtain and study the characteristics of high porosity rGO film.

(ii) To study the parameters required in developing the LB rGO layers suitable for algae biofilm growth.

(iii) rGO-algae film was investigated and its characteristics were studied to ensure that the film is able to replace the anode material in BPV.

1.3 Overview of the Thesis

This thesis contains five chapters. The introduction in chapter 1 explains the history and motivation behind the development of anode electrodes for BPV. The literature review, written in chapter 2 gives an overview analysis of previous progress in the BPV and electrode technologies. This section also reviews the LB mechanism, graphene as the vital material used in this thesis, electrochemical study, and development of the BPV itself. In chapter 3, preparation of the high porosity rGO and algae-rGO biofilm as the anode electrode in a BPV is explained thoroughly. Chapter 4, meanwhile discuss in detail the various experimental results obtained in this work. Finally, chapter 5 lists out the major conclusions and future research with pertaining to the electrode technology for application in BPV platforms.

CHAPTER 2

LITERATURE REVIEW

2.1 Langmuir-Blodgett Film

In 1174, Benjamin Franklin discovered that a little drop of oil tends to spread spontaneously covering a large area of the pond at Clapham Common, London.

"At length being at Clapham where there is, on the common, a large pond, which I observed to be the one day very rough with the wind, I fetched out a cruet of oil, and drop a little of in on the water. I saw it spread itself with surprising swiftest upon the surface.

In the experiments, one circumstance struck me with particular surprise. This was the sudden wide, and forcible spreading of a drop of oil in the face of water, which I do not know that anybody has hitherto considered. If a drop of oil is put on the polished marble table, or on the looking glass that lies horizontally; the drop remain in the place, spreading very little. But when put on water it spreads instantly many feet round becoming so thin as to produce the prismatic colors, for considerable space, and beyond the so much thinner as the to be invisible, expect in its effect of smoothing the waves at a much greater distance." (Franklin et al., 1774).

By assuming that the oil form a monomolecular layer, the thickness of the film should agree with the height of the molecule of triolein on top of the water surface. Franklin estimated that; one teaspoonful of olive oil will cover half an acre of the pond's surface. Half of an acre is about 2420 yd^2, which is equivalent to 2212.848 m^2. Assuming that one teaspoonful is about 2 $cm^3 = 2 \times 10^{-6}$ m^2, the thickness of the film that covers half of an acre is $(2x10^{-6})$ $(2212.848\ m^2) = 9.9 \times 10^{-10}$ m^2 which corresponds to monomolecular thickness. Franklin then reported his findings to the British Royal Society in 1774 (Franklin et al., 1774).

Seven centuries later in 1800, Agnes Pockels investigated the monomolecular film in her kitchen with a very simple homemade trough of 70 m long, 5 cm wide, and 2 cm high. By using a floating button, she studied the changes of surface tension when the molecular film was compressed on top of water. Her findings from the experiment was sent to Lord Rayleigh in the form of a letter and published in Nature on March 12, 1891 (Pockels, 1891). The work was then continued by Rayleigh, Devaux, and Hardy who confirmed the monomolecular nature of such films.

The investigation of monolayer properties continued for years after that and in 1934 Irving Langmuir made an astounding discovery in monolayer surface effects. His paper "*The Constitution and Fundamental Properties of Solids and Liquids*" in 1917 demonstrated the pressure-area relation of molecules on the water surface. Irving Langmuir discovered the method of transferring the floating monolayer onto solid substrates (Langmuir, 1916). Together with Katherine Blodgett, they discovered the potential to deposit mono and multilayer films and thus invented the LB method. For this discovery, Irving Langmuir was awarded the Nobel Prize and became America's first industrial scientist to win it.

2.1.1 Langmuir Film.

Langmuir film or sometimes denoted as Langmuir monolayer film can be well defined as the formation of a monolayer of atom or molecules between liquid-gas interfaces. It has an amphiphilic nature, which consists of the hydrophilic part and hydrophobic part (Letchford et al., 2007). Hydrophobicity is a property of a non-polar substance describing a component that does not easily dissolve in water while hydrophilicity is of a polar substance that upon contact with water, it interacts easily (Chandler, 2005). The hydrophobic part commonly consists of hydrocarbon or fluorocarbon chains and the hydrophilic part contains a polar group (or carboxyl group) such as –OH, -COOH, -NH_3^+, -PO_4, -($(CH_2)_2NH_3^+$ and others (Laughlin, 1994) as shown in Figure 2.1.

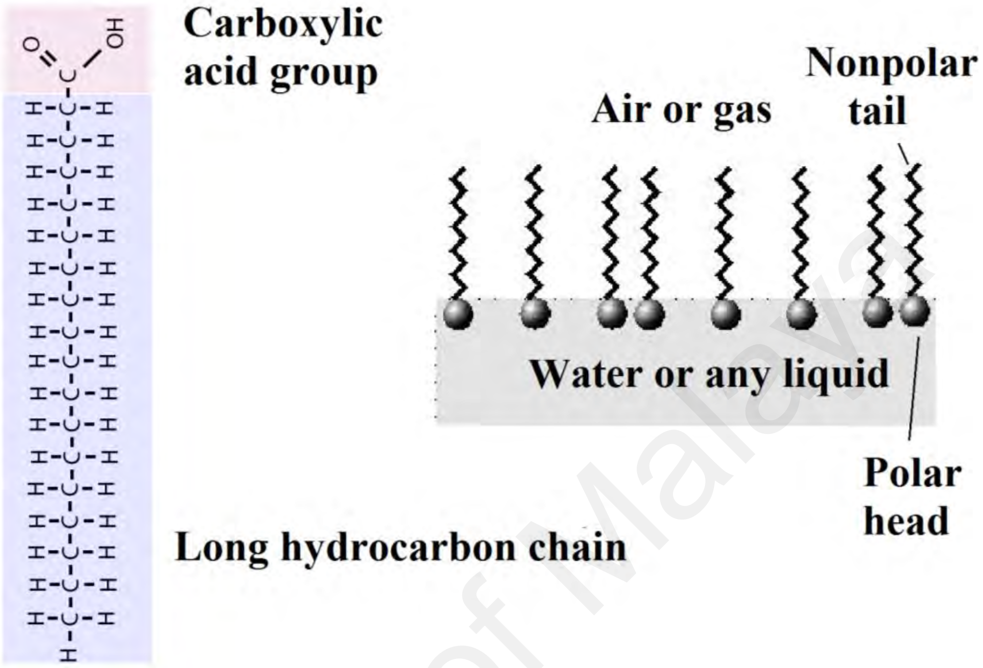

Figure 2.1: Illustration of amphiphilic component structure (left) and the orientation at air-water interface (right) (*Biochemistry: The chemistry of life*, 2015; *History of langmuir and langmuir-blodgett films*, 2014).

A monolayer of insoluble amphiphiles at the air/water interface has become known as a Langmuir monolayer, although the controlled and sophisticated experiments on these films existed over several decades before Langmuir. Films of amphiphilic molecules known as LB films are built-up by passing a solid substrate through a Langmuir monolayer. These can be single layers or multilayers depending on the number of passes made through the water surface.

2.1.2 Surface Tension of Water and Surface Pressure

The phenomenon of surface tension is due to the cohesive force among the molecules of liquid. In the bulk of the liquid, every molecule is pulled equally in every direction resulting in zero net force on the neighboring liquid molecules. However, a molecule at the surface does not have neighboring molecules at their top and therefore the forces are pulled towards the gas phase. This creates some internal pressure and forces liquid surface to diminish to the minimal area and contract.

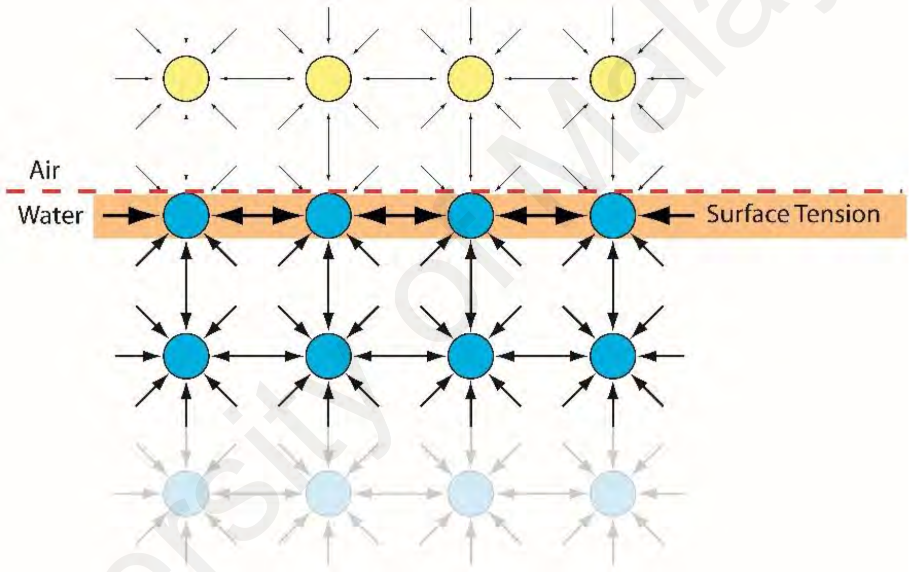

Figure 2.2: Schematic illustration of the interaction of molecules at an interface and interface bulk (Fuchs, 2013).

In the microscopic model of the real interface, the dynamic molecular motion moves in and out of it. For the interface to stay at equilibrium, the number of molecules that diffuse from the bulk to the surface per unit time must be same as the molecules leaving the surface for the bulk. The means atomic separation between surface molecules (which is the intermolecular force) will increase as more molecules diffuse initially from the surface. The activation energy of surface molecules escaping into the bulk will increase until it equals to the molecule diffusing from the bulk to the surface, and a state of equilibrium is achieved. The force acting on the surface molecules is the surface tension and is denoted as γ.

The presence of Langmuir film or monomolecular layer on top of the liquid surface will affect the surface tension. Normally, in LB experiment, the measurement of the surface pressure, π is used, which is equal to the reduction of the pure liquid surface tension by the film. This is given as below;

$$\pi = \gamma_o - \gamma \tag{2.1}$$

where γ_o is the surface tension of the pure liquid, and γ is the surface tension of the film covered surface. Many studies have been done with a variety of subphase such as water, mercury and hydrocarbons. However, in most cases, work involving transfer of monolayer on top of subphase onto solid substrate concentrate on aqueous deionized (DI) water subphase. Generally, the value of the deionized water surface tension is 72.8 mN m^{-1} at 20°C (Petty, 1996).

2.1.3 Surface – Pressure Isotherm

The significant development in LB technique is that it further elicits interest in the field by successful observation of the surface pressure-area (π – A) isotherm graph. This isotherm graph denoted as the physical background is deeply related to the molecular structure of the monolayer films. The thermodynamical phase transition in the monolayer is commonly mirrored in an isotherm as singularities such as flat regions (plateaus) or kinks (change in slope). A typical π – A isotherm is shown in Figure 2.3. Surface pressure at the beginning (region 1) is almost zero and the interaction of the monolayer can be significantly small. The monolayer in this region is considered to be in gaseous state where the molecules are apart from each other. As the molecules are being compressed, the surface pressure starts to increase as the molecule begins touching each other which is similar to gas molecule arrangement. The monolayer is considered being transformed from gaseous to liquid state (region 2). As expected, the molecules now behave as liquid particles in two dimensions.

Upon further compression, the monolayer will be in close-pack arrangement and the surface pressure will undergo a huge change in surface pressure (region 3). If further compression are carried-out, the monolayer will collapse as the molecules will be pushed on top of each other, sink, or collapse into a multilayer structure (region 4). The boundaries of the four regions have been previously determined by molecular, positional and orientational packing by using fluorescence microscopy and Brewster angle measurement (Schwartz, 1997).

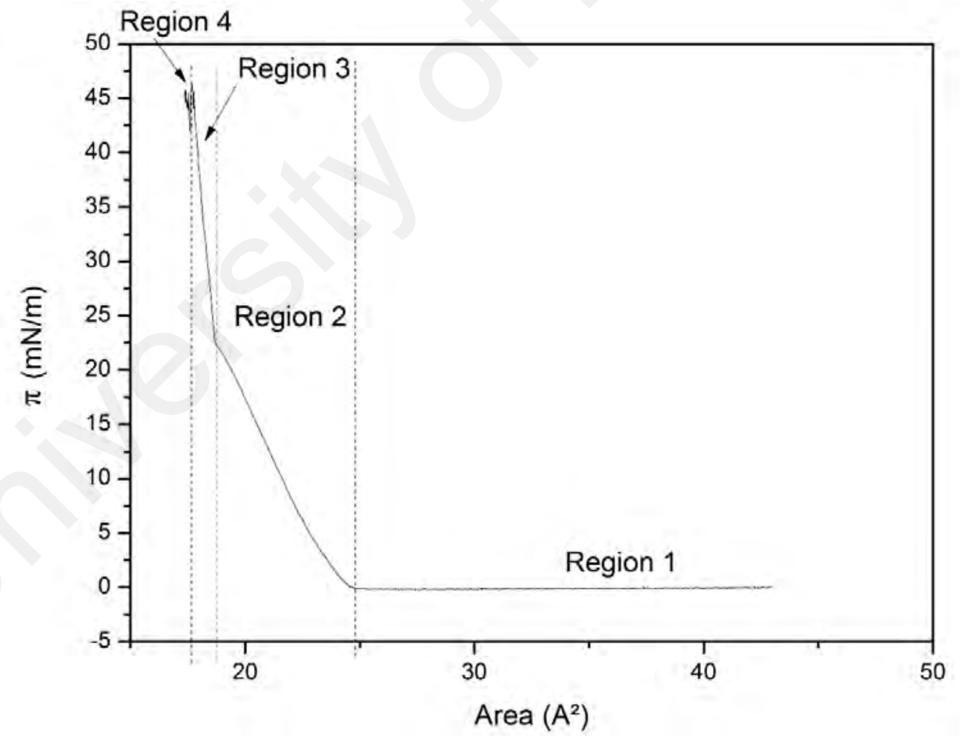

Figure 2.3: A surface pressure-area isotherm graph of arachidic acid at 25°C.

2.1.4 Intermolecular Force

Mechanical properties at the molecular level are influenced by compressibility between the molecules in an equilibrium situation. Hence, the insoluble monolayer characterization of the elastic modulus of the film is due to a strong force between the molecules. The Gibbs elasticity was noted as the degree of compressibility for a different phase of the monolayer. Thus, Gibbs elasticity, E is the degree of compressibility for a different phase of rGO monolayer. The elasticity of the monolayer is important for learning the process of generation of defects and disruption accomplished using round-type (NIMA LB trough model 2200), as used in this work.

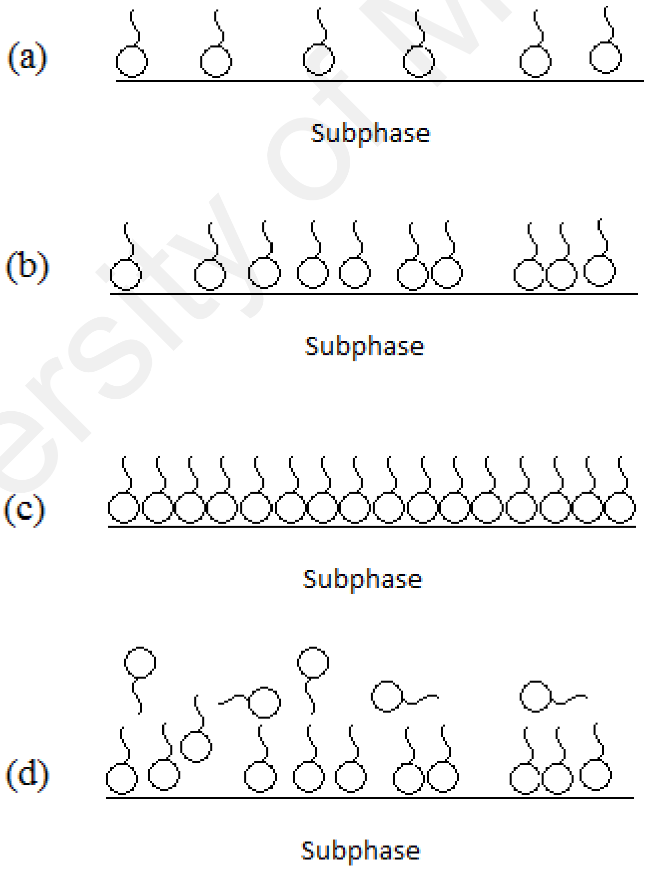

Figure 2.4: The orientation of molecular arrangement in different phase compression; a) in region 1, b) in region 2, c) in region 3, and d) in collapse state, region 4.

The compression modulus, K is given by;

$$K= -A\left(\frac{\Delta\pi}{\Delta A}\right)_{HC} \tag{2.2}$$

where A is the area per molecule or molecular area, π is the surface pressure and the subscript represents hydrostatic condition. Gibbs Elasticity corresponds to K [3], hence;

$$|E|=-A\left(\frac{\partial\pi}{\partial A}\right) \tag{2.3}$$

Intermolecular force, *F* between the molecules can be estimated by the value of elastic modulus that has been calculated before. This equation is written as;

$$F=2\times0.02\times[E] \tag{2.4}$$

2.1.5 Langmuir-Blodgett Film Deposition

LB deposition technique can be summarized as transferring monolayer film from the top of a subphase onto the solid substrate. Traditionally, LB deposition is carried-out in the solid region, with the surface pressure of the monolayer film maintained in a condensed and stable state. The LB film can be deposited alternately upwards or downwards trough the Langmuir monolayer. Due to the nature of polar head facing towards the liquid (bottom) and nonpolar tail facing upward or away from the liquid, the arrangement of the film can be manipulated. If the dipping of the solid substrate is the upward ("upstroke") movement, their polar heads are arranged towards the substrate as shown in Figure 2.5. While dipping a solid substrate downward (the "downstroke"), the nonpolar head will be arranged towards the solid substrate as shown in Figure 2.6.

A continuous repetition of dipping will create a multilayer film. The multilayer film has three types of deposition arrangements; namely the X-type, Y-type, and Z-type. The X-type deposition is denoted repeating the downward deposition, which creates a tail-head-tail-head multilayer film as illustrated in Figure 2.7 (a). The Y-type deposition meanwhile involves repeated downward and upward depositions, which creates a head-tail-tail-head multilayer film or simply summarized as "head to head" and "tail to tail" arrangement as illustrated in Figure 2.7 (b). Finally the Z-type deposition involves a repeating upward deposition, creating a head-tail-head-tail multilayer film as shown in Figure 2.7 (c).

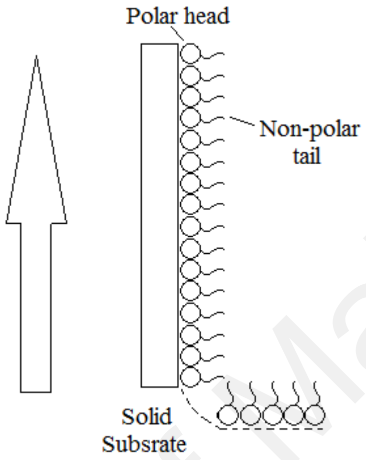

Figure 2.5: The arrangement of monolayer film by upwards (upstroke) dipping technique.

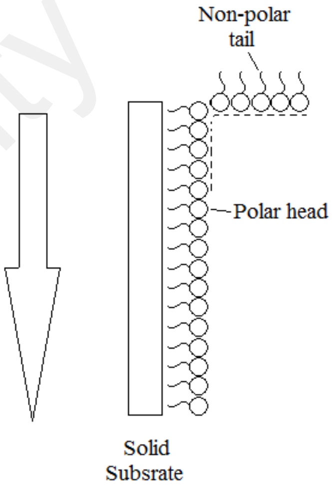

Figure 2.6: The arrangement of monolayer film by downwards (downstroke) dipping technique.

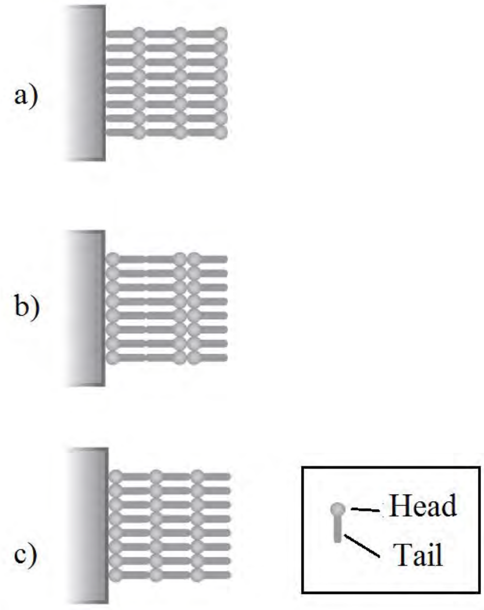

Figure 2.7: Three types of the multilayer films by different arrangements. (a) X-type deposition is the tail-head-tail-head arrangement. (b) Y-type deposition is the head-tail-tail-head arrangement, and (c) Z-type deposition is the head-tail-head-tail arrangement.

2.1.6 Deposition Speed

In the process of LB deposition technique, deposition speed needs to be carefully monitored for it cannot move faster than the speed of draining of water from the solid substrate. The drainage of the water while dipping does not occur because of gravity itself. It is also influenced by the adhesion between the monolayer and material of substrate while being transferred from the top subphase to the solid substrate. The deposition speed for monolayer transfer onto the solid substrate normally starts at a relatively slow speed of 10 μms^{-1} to a few mms^{-1}. A faster speed up to cms^{-1} is possible once the initial layer has been transferred. For improvement in the film deposition, it is advisable to allow the film on the solid substrate after dipping for a period of time for complete drying before continuing the deposition cycle.

2.2 Graphene

2.2.1 Introduction to Graphene

Graphene was first prepared by Brodie in 1859 (Brodie, 1859), and since 1935, graphene have been studied theoretically and was commonly used for interpreting properties of various carbon-based materials. 20 years later, it was recognized that graphene might offer an excellent condensed matter analogue of (2+1)-dimensional quantum electrodynamics (Fradkin, 1986; Haldane, 1988; Semenoff, 1984). This drove graphene into a flourishing theoretical toy model. In the beginning, graphene was known as an integral part of 3D materials and were assumed to not exist in a free state (Geim et al., 2007).

Graphene as 2D material was initially denoted as an unstable material that should not have existed as Landau and Pierls argues that 2D crystals will be thermodynamically unstable (Landau, 1937; Peierls, 1935). Due to it having a divergent contribution of thermal fluctuation in low dimensional crystal lattices, it should lead to such displacement of atoms that they become equivalent to interatomic distance at any finite temperature (Landau et al., 1957). The statement was also supported by Mermin (Mermin, 1968), due to the various experimental observation. The melting temperature of thin film sill rapidly decreases when thickness is decreased. Hence, the film becomes unstable (segregates into islands or decompose) at a typical dozens of atomic layers thickness (Evans et al., 2006; Venables et al., 1984). Hence, the atomic monolayers should be integral part of a larger 3D structure, and grown epitaxially on top of a monocrystal with matching crystal lattice (Evans et al., 2006; Venables et al., 1984). With this reason, 2D materials were assumed not to be able to exist without 3D base.

It is later that the discovery of the unexpected vintage free-standing graphene (Novoselov et al., 2005; Novoselov et al., 2005) has shown that graphene is now represented as a new class of materials composed of a periodic array of carbon atoms densely packed in a very regular 2D honeycomb structure (Geim et al., 2007). The very first theoretical description of graphene was only reported in 2003 (Sluiter et al., 2003). One year later, Geim and Novoselov successfully synthesized the 2D structure of graphene using a simple "peeling" technique (Novoselov et al., 2004). Since the discovery in 2004, the material has became an instant "star" in material science due to its enormous impact in the material science discipline. Furthermore, graphene has been widely used due to its chemical and physical properties that came from its highly hybridized sp^2 bonds resulting in a strong mechanical resistance, as well as heat and electrical properties and high optical transmittance (Zhu; et al., 2010). Graphene also finds use in non-volatile memory applications (Jeong et al., 2010), infrared optoelectronic sensors (Gilgueng et al., 2009), thin film transistors (He et al., 2011), transparent solar cells (Wang et al., 2012), and biosensors (Liu et al., 2012).

2.2.2 Structure

Graphene has been denoted as the first 2D material ever discovered by mankind (Gibney, 2015). The structure is composed by two equivalent sub-lattice of carbon atom bonded together with σ bonds shape arranged in the structure of a honeycomb lattice as shown in Figure 2.8 (Zhu; et al., 2010).

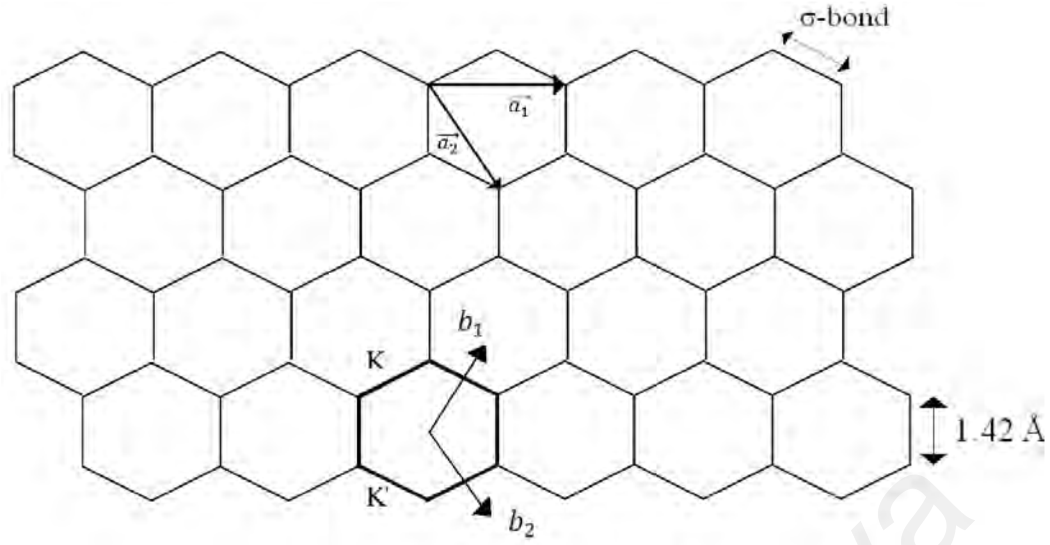

Figure 2.8: The honeycomb lattice of graphene and the lattice information (Castro Neto et al., 2009).

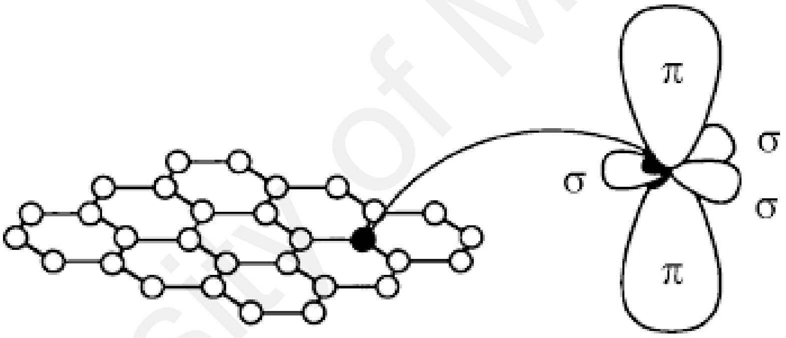

Figure 2.9: Structure of sp^2 hybridize with sigma bond and π bond of graphene (Jorio et al., 2011).

Each carbon atom of graphene undergoes a sp^2 hybridization between one 2s and the 2p orbitals resulting in three sp^2 hybridized orbitals (Lemme, 2009). In elaboration, the electron in each carbon atom is organized in different orbitals, where two electrons fill the inner shell of 1s orbital. The remaining four electrons occupy the outer shells of 2s and 2p orbital. In the presence of another carbon atom, it is favourable to excite one electron from the 2s to the third 2p orbital in order to form a covalent bond, hence creating the sp^2 hybridization. Thus, it creates three equal parts pointing outward in a planar plane called the σ bonds. The remaining electrons create half-filled π bands and were constructed by the unaffected p-orbital, which is perpendicular to its planar plane as shown in Figure 2.9 (Chen et al., 2011).

As described before, graphene was considered to exist as a honeycomb lattice. Furthermore, graphene structure is also tight binding, having the basic unit cell in the rectangle that contain two equivalent carbon atoms. In the case of the real space lattice vectors, it is described as (Castro Neto et al., 2009);

$$a_1 = \frac{a}{2}(3, \sqrt{3}),\ a_2 = \frac{a}{2}(3, -\sqrt{3}) \tag{2.5}$$

where a=1.42 Å is the carbon-carbon length.

Furthermore, the reciprocal lattice vectors are also given as;

$$b_1 = \frac{2\pi}{3a}(1, \sqrt{3}),\ b_2 = 2\pi\ (1, -\sqrt{3}) \tag{2.6}$$

The corresponding space lattice of a_1, a_2, b_1, and b_2 are described to be in the first Brillouin zone for grapheme and is hexagonally arranged (Figure 2.8) (Castro Neto et al., 2009). The first Brillouin zone is described as the primitive cell in reciprocal lattice. Furthermore, the structure of C-C bond between the four valence electrons confer the high mechanical strength of graphene despite being only of atomic layer thickness (Sheka, 2014). Moreover in the microscopic observation of graphene, it is estimated that graphene exhibits a lateral dimension of about 8 to 10 nm. The height displacement of graphene meanwhile has a value of about 0.7 to 1 nm (Zhu; et al., 2010). Observation of single-atom-thick plane of graphene was acknowledged by optical microscope using a mechanical exfoliation process. The success of the observation is by placing the graphene on top of a silicon wafer, and the feeble interference-like contrast with respect to an empty wafer was measured and concluded (Zhu; et al., 2010).

2.2.3 Properties of Graphene

2.2.3.1 Electrical Properties

Graphene has an extraordinary band structure to its crystal arrangement. From Figure 2.9, it is shown that graphene contain pair π-orbitals oriented in z-axis direction. It is referred as π-band or sometimes as π^*-bands. These bands are responsible for the unusual electronic properties of graphene (Cooper et al., 2012). Due to the 2D structure of graphene, the first Brillouin zone has two non-equivalent points of K and K' (called Dirac points) (shown in Figure 2.10), which is where a band crossing occurs. Dirac point is the location in momentum space, located on the edge of the Brillouin zone. It is the place of transition between valence band and the conduction band. It is also described as the location in momentum space, located on the edge of the Brillouin zone as shown in Figure 2.10.

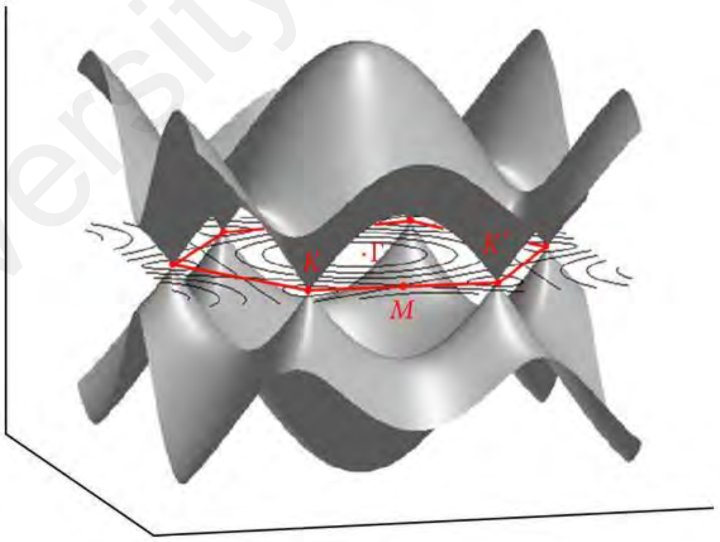

Figure 2.10: First Brillion zone and band structure of graphene (Cooper et al., 2012).

The vertical axis in Figure 2.10 is energy while the horizontal axes are the momentum space on the graphene lattice. The first Brillouin zone of graphene is illustrated in the horizontal plane and labelled with some points of interest. K and K' are the two non-equivalent corners of the zone, while M is the midpoint between adjacent K and K’ points. Γ is the zone centre (Cooper et al., 2012). Furthermore, the tight-binding for the first nearest neighbour may offer dispersion relation of the electrons near K/K’ point (Castro Neto et al., 2009; Wallace, 1947).

Graphene has also been acknowledged to have zero-gap semiconductor due to the conduction and valence band meeting at the Dirac points (Cooper et al., 2012). Therefore, graphene is a perfect conductor. In Hubbard model, an approximation model is used to describe the interacting particle in the lattice. The Hubbard model is based on tight-binding approximation, which states that the electron occupies standard orbitals of the constituent atom and then transfer or “hops” between atom during conduction. It is calculated that the magnitude of hopping energy for graphene is about 2.8 eV (Castro Neto et al., 2009; Wallace, 1947).

One of the important aspects for understanding the electrical properties of a material is by understanding the Fermi velocity. The Fermi velocity, V_F is associated with the kinetic energy in Fermi energy, E_F and corresponds to the specific number of particles in specific systems at specific temperature. The Fermi energy corresponds to the energy that would be associated with the next highest energy rung in the system if one electron were to jump to that energy level. In addition, the Fermi energy gives us the information of the velocities of the electron that participate in ordinary electrical conduction. The amount of the energy that can be given to an electron in such conduction processes is in the order of micro-electron volt. V_F calculation is expressed by $V_F=\sqrt{(2E_F/m)}$, where m is the mass. It is calculated that graphene has a Fermi velocity value of 1 x 10^6 ms^{-1} (Zhu; et al., 2010), which is lower than copper (1.57 x 10^6 ms^{-1}) (Rambaut et al., 1989), silver (1.39 x 10^6 ms-1) (Gijs et al., 1989), and gold (1.40 x 10^6 ms^{-1}) (Tuersun et al., 2015). This means that graphene has better conductivity than copper, gold, and silver.

As a material that has zero band gap due to its unique band structure, graphene also displays an ambipolar electric effect (a transport properties). The charge carrier can be modified continuously between the electrons and holes in concentrations as high as 10^{13} cm^{-2}, with room temperature mobility, μ going up to 15 000 $cm^2V^{-1}s^{-1}$ even under ambient conditions (Novoselov et al., 2005; Novoselov et al., 2004; Zhang et al., 2005). Observed mobility tends to depend weakly on temperature, signifying that ultrahigh mobility could be realized at room temperature. The mobilities of suspended graphene can be in excess of 200 000 $cm^2V^{-1}S^{-1}$ by minimizing impurity scattering (Dürkop et al., 2004). It remained high even at a high carrier density in both electrically and chemically doped devices, which demonstrates evidence of ballistic transport on the sub-micrometer scale (Schedin et al., 2007).

The electronic superiority of graphene can be concluded if the Quantum Hall Effect (QHE) could be witnessed at room temperature. The QHE is the quantum mechanical description of Hall Effect. Hall Effect is described as the production of a voltage difference (the Hall voltage) across an electrical conductor, transverse to an electric current in the conductor and a magnetic field perpendicular to the current. QHE is observed in 2D electron systems that are subjected to low temperature and strong magnetic fields. In the case of low temperature and high magnetic field, it is observed that QHE is exhibited for both electrons and holes indicating that graphene display an exceptional mobility due to its unique band structure (Novoselov et al., 2005).

2.2.3.2 Mechanical Properties

Elasticity of graphene in a perpendicular direction is vastly different from the elasticity along the basal plane. The Young’s modulus of graphene and fracture strength has been studied with various simulations. For example, molecular dynamics and experimental investigations using force-displacement measurement by Atomic Force Microscopy

(AFM) has been carried-out (Rasuli et al., 2010). The mechanism of using AFM involves the strip of graphene being suspended over trenches for the mechanical investigation as shown in Figure 2.11, therefore the Young Modulus value of the substrate can be discarded (Frank et al., 2007). It is described that the defect-free graphene has a Young's modulus of 1.0 TPa and a fracture strength of 130 GPa (Gómez-Navarro et al., 2008).

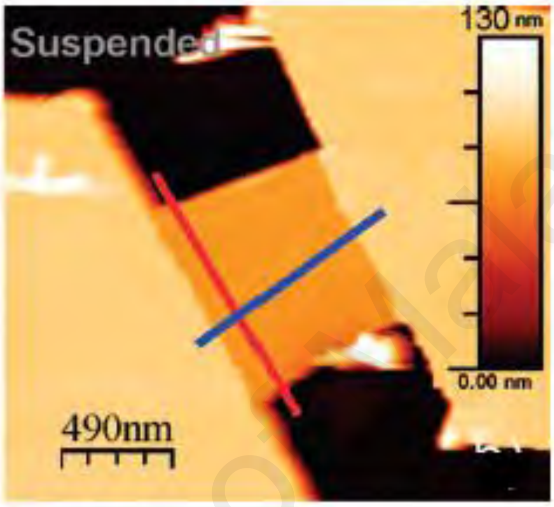

Figure 2.11: AFM image of graphene suspended over trench (Gómez-Navarro et al., 2008).

A chemically modified graphene is acquired by reducing GO with hydrogen plasma. The mean elastic modulus acquired from the chemically modified graphene has a value of 0.25 TPa (with standard deviation reported to be 0.15 TPa) (Zhu; et al., 2010). The fracture strength however was not stated. A test to measure spring constant was developed by suspended graphene SiO_2 cavities and the AFM tip was used to apply a stress to the sheet. The spring constant was measured to be in the range of 1-5 N/m, while the stiffness value was 0.5 TPa, which is different from the bulk of graphite (Frank et al., 2007).

2.2.4 Oxidation of Graphene and its Reduction

One of the most exciting researches in graphene materials is the establishment of GO. Staudenmaier's method has always been utilized for more than 60 years for making GO sheet. However, two chemists by the name of Hummers and Offeman developed a method that produces a higher degree of oxidation compared with Staudenmaier's method (Hummers et al., 1958). Nonetheless, the method has been reported to yield incompletely oxidized graphite core with GO shells, and the pre-expansion process is helpful to achieve a higher degree of oxidation. In response to this, several methods have been developed to overcome the problem. Kovtyukhovra in 1999 introduced a modification of Hummer's method and was widely used by many researchers to produce high quality graphene (Kovtyukhova et al., 1999).

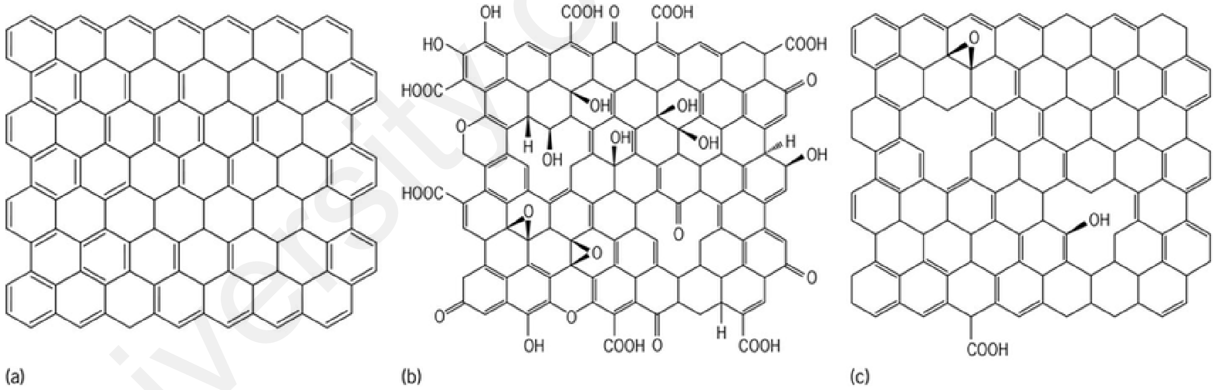

Figure 2.12: Structure of graphene (a), GO (b), and rGO (c). (Griggs et al., 2016).

Typically, GO products from the modified Hummer's method contain thin flakes with 1 nm thickness and have a lateral dimension of 1 micron on average. The chemical composition is determined to be C:O:H = 4:2.95:2.5 (Kovtyukhova et al., 1999). The oxygen functional group have been recognized commonly as hydroxyl and epoxy groups on the basal plane, and together with a smaller amount of carboxy, carbonyl, phenol, lactone, and quinone at the sheet edges (Eda et al., 2008; Kim et al., 2010; Wang et al., 2011). Nevertheless, the precision of the atomic structure of the GO proposed is still unclear and remain to be fully elucidated due to the uncertainty pertaining to both the nature and distribution of the oxygen-containing functional groups (Compton et al., 2010). Various other applications have led to the development of rGO. rGO is a chemically reduced GO that still contains the latter's properties but the functional group of GO was reduced as shown in Figure 2.12 (Chen et al., 2012).

Shao et al reported that rGO displays a greater electrochemical capacitance with cycling durability than carbon nanotubes (Chen et al., 2012). The rGO-based electrode exhibits fast electron-transfer kinetics and possesses excellent electrocatalytic activity towards oxygen reduction (Wang et al., 2010). Chen and co-workers reported that fabrication of rGO-Co(OH)^2 nanocomposites in water-isopropanol system demonstrated a significant improvement of electrochemical performance after deposition on rGO sheets.

rGO can also be used to functionalize quantum dots (QD) for electrochemical application. QD can be referred to as the semiconductor crystal of nanometer dimensions with distinctive conductive properties as determined by its size. To visualize this, imagine that there are many balls in nanometer dimensions on the floor exhibiting quantum properties. In addition to metal and metal oxide nanoparticles, QD has also been used to functionalize GO with a view to create other possible electrochemical applications. Moreover, the QD-sensitized rGO nanocomposites could be prepared by in-situ growth if QDs nanocovalently functionalized rGO. It is reported that QD-sensitized rGO photoelectrons were an efficient platform for photoelectrochemical sensors (Chang et al., 2010).

2.2.5 Graphene-based Electrode Films

There are various methods reported to produce graphene, GO, and rGO for electrode film. For example, GO platelets can be deposited via spin coating (Becerril et al., 2008; Watcharotone et al., 2007) dip coating (Wang et al., 2008), vacuum filtration (Goki et al., 2008), and LB assembly (Cote et al., 2009). Other than that, numerous methods have been developed to obtain graphene or rGO suspensions for the preparation of transparent conductive films (TFCs) that can to use as electrode surfaces (Park et al., 2009). Examples such as, spray-coating techniques to deposit TFCs from aqueous dispersion of rGO nanoplatelets can be obtained by altering the pH to 10 prior to it’s reduction with hydrazine (Li et al., 2008).

Moreover, the LB-assembled films consisting of overlapped and stacked chemically modified graphene have resulted in sheet resistance of around 8 k Ω/sq with the value of transparency at 84% (1000 nm) (Li et al., 2008). Assembly methods at liquid interfaces with a range of densities, known as liquid-liquid assembly method has been used to prepare highly hydrophobic films that consist of multilayer graphene platelets. These liquid-liquid assemblies have been reported using a H_2O-chloroform interface (Biswas et al., 2009).

Furthermore, randomly stacked layers of graphene platelets can form disordered multilayer films, which can be made by directly sonicating graphite in organic solvents and vacuum filtration (Hernandez et al., 2008). Other than that, the fabrication of graphene electrode films based on the chemical reduction of GO platelets in a liquid dispersion has allowed their spin-assisted assembly to occur in a one-step fabrication process (Zhu et al., 2009). Moreover, chemical vapour deposition on metals offers the opportunity of growing high quality graphene electrode films over a large surface area (Kim et al., 2009; Li et al., 2009; Reina et al., 2009).

However, among the listed methods to fabricate graphene-base electrode films, LB assembly methodologies offer numerous advantages in producing high quality monolayer with large areas (Cote et al., 2009). In addition LB assembly has become one of the most promising techniques for preparing and re-engineering nanometer-ordered thin films due to its efficient control of the film thickness. Moreover, it also offers large-area homogenous deposition, and the opportunity to deposit multilayer films (Petty, 1996; Schwartz, 1997; Zheng et al., 2012).

For electrochemical sensing in biological systems, carbon based electrodes have been reported to enhance sensitivity. Examples are seen in studies related to enzyme metabolism utilized in the detection of proteins in biosensor applications (Shao et al., 2010). Moreover, due to their inherently abundant functional groups, graphene-based electrode materials have established unique capabilities for electrical sensing of biological systems (Geim et al., 2007; Singh et al., 2014).

Also, graphene and GO layers have been in the mainstream for material science and widely explored to substitute and form new composite materials (Eda; et al., 2010) due to its biocompatible properties. Biocompatibility behaviour in GO is due to the existence of the oxygen-containing functional groups, which have been extensively reported on the surface of rGO or functionalized graphene sheets (Eda; et al., 2010; Fan et al., 2010; Singh et al., 2014) and vital for the fabrication of electrochemical devices.

2.3 Electricity from Biomaterial

2.3.1 Bioelectrochemical System

In 1911, M. C. Potter published a remarkable discovery titled *"Electrical effects accompanying the decomposition of organic compounds"* that indicate the fact that certain bacteria can transfer their electron extracellularly while degrading organic waste (Potter, 1911). A maximum voltage of 0.3 to 0.5 V was recorded simply by using *Saccharomyces cerevisiae* as the test organism, platinum as electrode, and glucose as substrate. The ability of microbes to transfer electrons extracellularly or outside of the cell by direct and/or indirect process can be referred to as exoelectrogenic activity (Logan, 2009).

This has driven the development of a variety of devices since the exoelectrogenic process can be harvested for reductive power which the living organism directly generate electrical energy (Mccormick et al., 2015). These are known as bioelectrochemical systems (BESs) (Hamelers et al., 2009; Rosenbaum et al., 2014). This development is one of the most promising technologies for future renewable energy. Production of BESs has driven new technology involving systems powered by light energy from the sun (Lewis et al., 2006). Depending on the biocatalyst, BESs can also be classified as MFC or Enzymatic Fuel Cell (EFC) (Osman et al., 2011). BES can be sub-divided into MFC, Microbial Electrolysis Cell (MEC), Microbial Desalination Cell (MDC), and Microbial Solar Cell (MSC) (Pant et al., 2012). The concept of MFCs will be explained in subtopic 2.3.2.

2.3.1.1 Microbial Electrolysis Cell

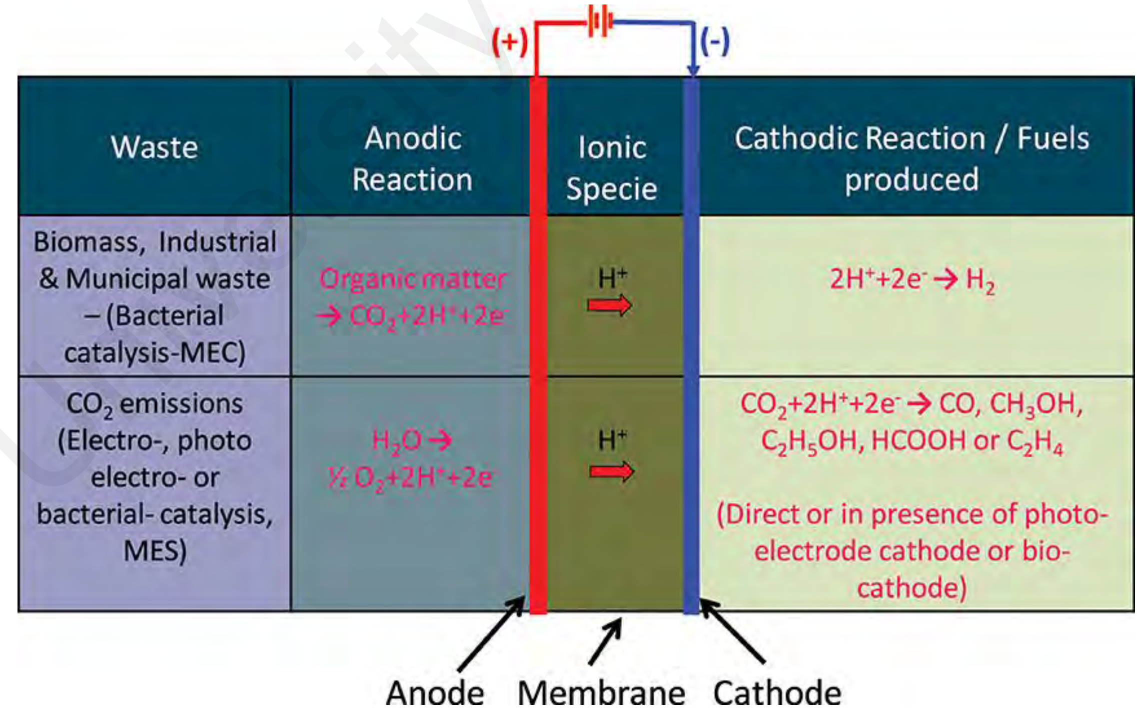

Figure 2.13: Electrochemical reactions involved in various processes in MED for producing fuels and value-added chemicals from waste (Badwal et al., 2014).

MEC is a technology that harvests electricity from the microbial decomposition of organic compound. Moreover, the MEC is a technology converting carbon dioxide, CO_2 into methane by using electricity as the energy source while the microorganisms act as the catalyst (Pant et al., 2012). Figure 2.13 illustrates the working principle of a typical MEC where the anode chamber of the device contains organic and inorganic waste, which is oxidized with the help of the microorganisms (electrochemically active bacteria). The process of charge transfer and energy production is illustrated in the diagram, to either produce hydrogen (as a fuel) or other value added chemicals such as biofuels (Badwal et al., 2014).

2.3.1.2 Microbial Desalination Cells

MDC is a technology developed from the integration of MFC process and electrodialysis. It can also be used for wastewater treatment, water desalination, and production of renewable energy. MFC can operate with or without mediator (which involve the addition of external bacteria to oxidize substrate) (Torres, 2012). A typical MDC consist of anode and cathode chambers. It has an additional desalination chamber in the centre, which is created by inserting an anion-exchange membrane (AEM) and a cation-exchange membrane (CEM) on each side. The anode chamber is accountable for organic degradation and electricity production, whereas the central chamber is accountable for removing salt from seawater. Cathode chamber meanwhile is responsible to complete the electrical loop (Luo et al., 2012). The structure of MDC is illustrated in Figure 2.14.

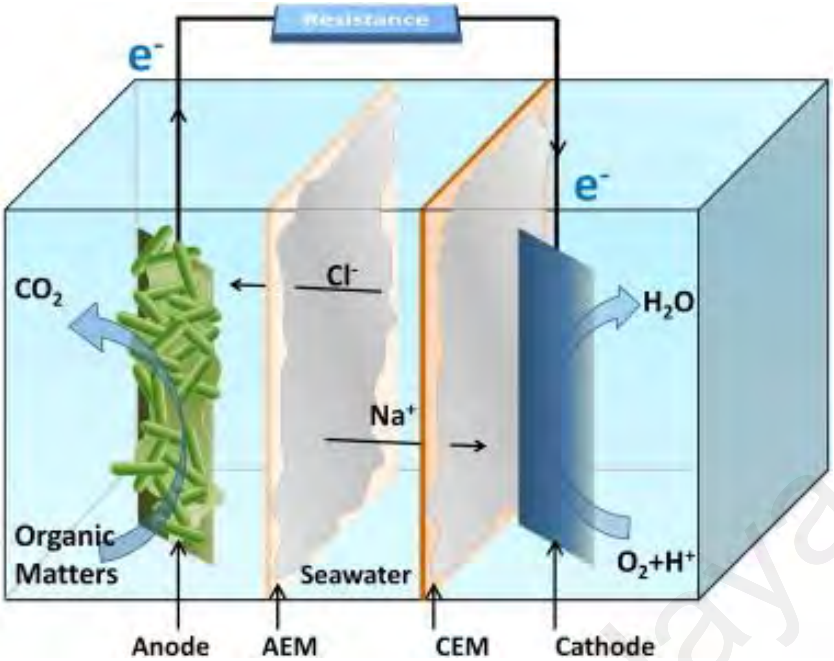

Figure 2.14: Schematic of an osmotic microbial desalination cell consisting of forward osmosis membrane (FOM) and cation exchange membrane (CEM) (Ping et al., 2013).

2.3.1.2 Microbial Solar Cells

MSC is a technology that utilizes in-direct solar energy to produce electricity or chemicals and is considered a light harvesting autotrophic system. The basic principles of MSC can be divided into four parts as illustrated in Figure 2.15. MSC involve photosynthesis mechanism (a) that uses water and carbon dioxide to produce glucose and oxygen gas. Next, it transports the organic matter to anode compartment (b). Then the process of oxidation of organic matter by electrochemically active bacteria occurs in the anode compartment (c). Glucose and water produce bicarbonate, hydroxide, and electrons. Then in the cathode compartment, the reduction of oxygen to water takes place (d) (Strik et al., 2011).

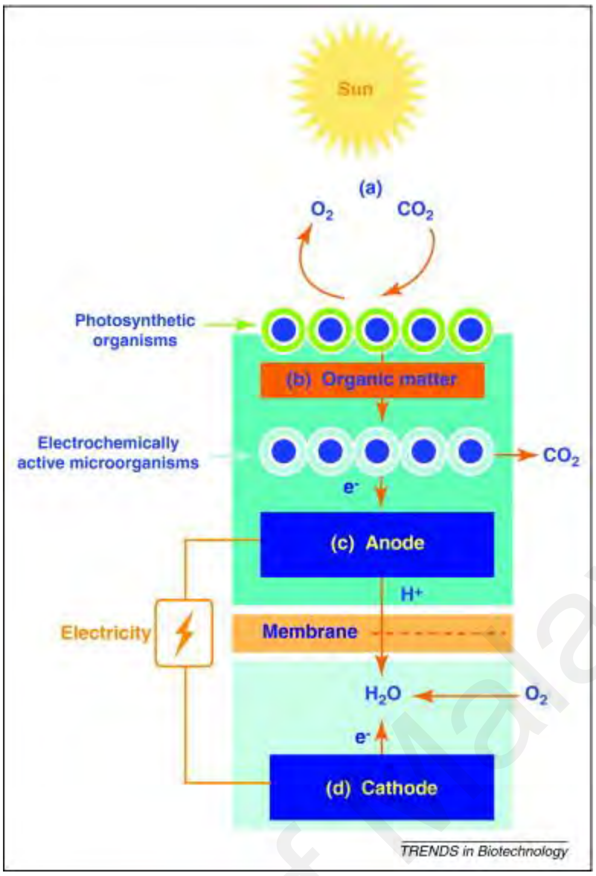

Figure 2.15: Model of a microbial solar cell including the basic principles; (a) photosynthesis, (b) transport of organic matter to the anode compartment, (c) anodic oxidation of organic matter by electrochemically active bacteria and (d) cathodic reduction of oxygen to water (Strik et al., 2011).

MSC is a technology that utilizes in-direct solar energy to produce electricity or chemicals and is considered a light harvesting autotrophic system. The basic principles of MSC can be divided into four parts as illustrated in Figure 2.15. MSC involve photosynthesis mechanism (a) that uses water and carbon dioxide to produce glucose and oxygen gas. Next, it transports the organic matter to anode compartment (b). Then the process of oxidation of organic matter by electrochemically active bacteria occurs in the anode compartment (c). Glucose and water produce bicarbonate, hydroxide, and electrons. Then in the cathode compartment, the reduction of oxygen to water takes place (d) (Strik et al., 2011).

2.3.2 Microbial Fuel Cell

The most common area of BESs is in the development of MFCs, which is considered the oldest studied group in BESs (Potter, 1911). MFCs are devices that uses bacteria as the catalyst (biocatalyst) to oxidize organic and inorganic matter and generate current (Berk et al., 1964; Davis et al., 1962; Rao et al., 1976). Electron generation in anode MFCs can be reached through indirect extracellular electron transfer and/or by direct electron transfer known as direct extracellular electron transfer (Lovley, 2011). MFCs contain of anode and cathode chambers divided by a proton exchange membrane (PEM) (Ghasemi et al., 2013). An active biocatalyst in anode compartment oxidize the organic substrates and produce electrons and protons (Antonopoulou et al., 2010). The electrons are transported through the external circuit, and the protons are conducted to the cathode compartment by passing through PEM (Rahimnejad, 2011). Protons and electrons will react in the cathode compartment and along with the reduction of oxygen produces water (Sharma et al., 2010).

The active biocatalyst in anode compartment oxidizes the carbon source (typically from substrate), and generates the electrons and protons. Oxygen in the anode chamber will prevent the production of electricity. Hence, the bacteria must be keep separated from oxygen (Najafpour et al., 2011). The MFC device is illustrated in Figure 2.16.

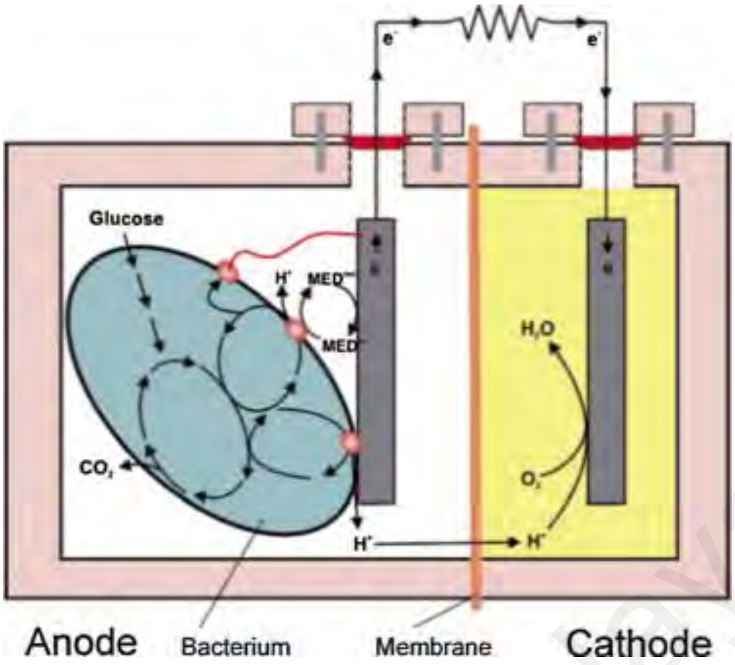

Figure 2.16: The MFC system is consisted of anode and cathode compartments (Logan et al., 2006).

2.3.3 Biophotovoltaics

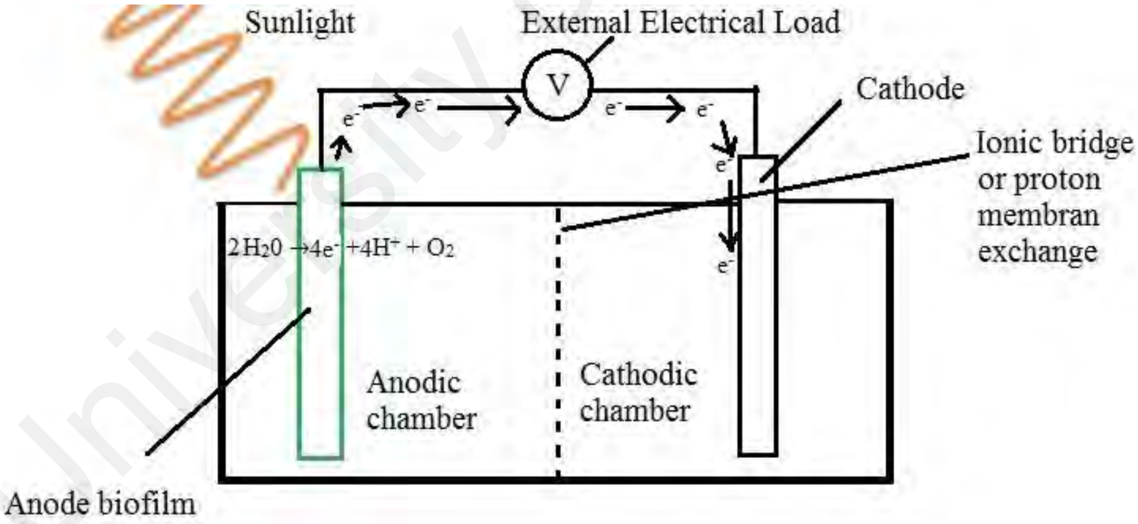

Figure 2.17: Schematic diagram of a BPV platform.

The development of MFCs has driven the development of novel systems that do not require an organic substrate. A typical BPV device uses oxygenic photosynthetic organisms and part of the oxygenic photosynthesis apparatus (Mccormick et al., 2015). The oxygenic photosynthesis organism is used to capture light, carry-out photolysis for splitting water, and supplying a source of electrons to the anode using indirect extracellular or direct extracellular electron transfer (Bradley et al., 2012).

The design of a BPV system typically consists of two sealed compartments; the anodic and the cathodic cell compartments (Figure 2.17). Photosynthetic materials, such as purified oxygenic photosynthetic reaction centres (Photosystem II, PSII), (Gerster et al., 2012; Yehezkeli et al., 2012) thylakoid membranes, (Calkins et al., 2013) cyanobacteria (Bombelli et al., 2011) or green algae (Ng et al., 2014) are inoculated and cultivated in the anodic compartments. It uses the energy of light to split water into oxygen, protons, and electrons. In principle, the initial process involved in the generation of electrons is usually related to an oxygenic photosynthetic reaction centre such as the PSII. This is where the electrons are generated by light-driven oxidized water. The pathway of electron flow from PSII to external circuit depends on the biological material used (Mccormick et al., 2015). Thus, a potential difference between two electrodes results in the current flowing from anode to the cathode.

BPV system offers an inexpensive technology that provides energy from light. It also has value added benefits such as being carbon-neutral, and having the essential ability to store energy. BPV technology may offer valuable incentives to enable the change from carbon-based primary energy production that would harm the environment. As such, BPV technology offers a solution for a greener alternative energy, besides promising as a carbon negative solution.

CHAPTER 3

EXPERIMENTAL METHODS AND ANALYTICAL TECHNIQUES

In this chapter, the methodology to fabricate high porosity rGO film is listed and described step by step. The preparation of rGO suspension, cleaning protocol, and the dip-coating of rGO film by using LB technique is discussed. Furthermore, this chapter also explains in detail the methodology for obtaining rGO-algae anode electrode used in the BPV. It involves culturing *Chlorella sp*. on top of rGO and ITO electrodes. The chapter also explains in detail the electricity generating BPV device developed and fabricated in this work. Finally, all the analytical techniques used in this thesis is also discussed. Characterization studies involve morphology, optical and electrical properties, and surface chemistry of the rGO film. This is followed by an in-depth discussion to understand the charge transfer mechanism involved.

3.1 Preparation of rGO Film Suspension

rGO was bought from Graphene Supermarket USA (High Surface Area rGO 75 mg). The rGO has a specific surface area of 833 m^2/g and average thickness of one layer (0.7~1 nm). Carbon and oxygen ratio of the rGO has a ratio 10 to 5 and the average particle (lateral) size is 3 to 5 µm.

2.0 mg of high surface rGO was prepared and mixed with 1.0 mL methanol, (CH_3OH) in a 5 mL vial and sealed with a parafilm. After that, the vial was sonicated using a frequency of 40 kHz in the water medium. As a precaution, the sonication cannot be carried out for more than one hour because it will cause the methanol temperature to rise and may lead to evaporation. Evaporation of methanol will cause the cap to become loose and might cause contamination in the vial by a foreign material such as water due to sonication in water bath. Other than that, it may also reduce the total volume of methanol. Continuously operating the sonicator will overheat and damage it. As such, rest periods of 15 to 30 minutes and changing the water in the bath ensures that the temperature is not too hot. The sonication was carried-out for another hour before allowing to rest. The protocol was repeated until the total time of sonication is up to 10 hours. After completion of the sonication process, the solution was stored in a 1K-cleanroom facility until it reaches thermal equilibrium.

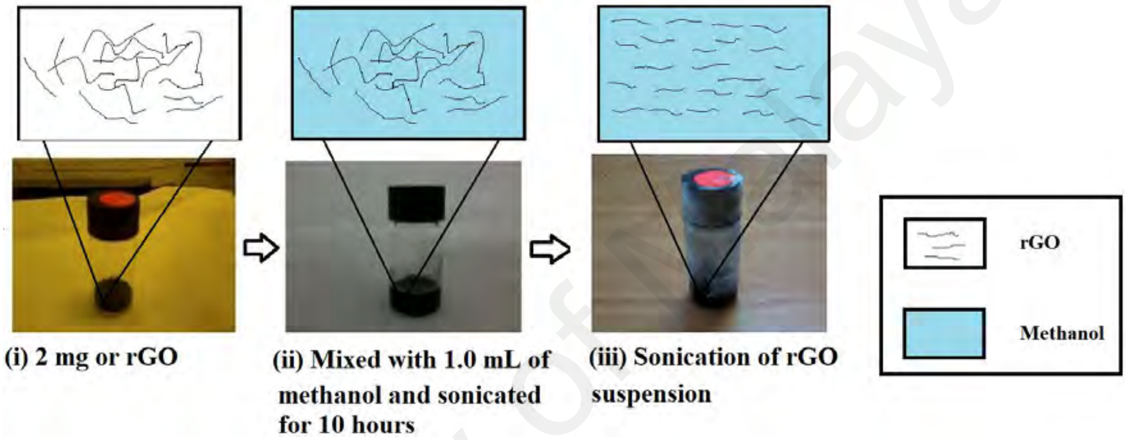

Figure 3.1: Process of preparing rGO film suspension.

3.2. Film Deposition

This section will discuss the strict cleaning protocol that is very crucial to obtain clean rGO films. It discusses the mechanism to obtain π-A isotherm graph that is important for understanding rGO at air-water interface characteristics. The understanding of surface pressure versus area will provide the information regarding the air-water interface such as gaseous state, liquid state, and breaking point. This will enable the determination of the suitable target pressure that will be used in the deposition process. It will also provide useful information for multilayer deposition and allow the control of surface morphology, thickness, and film orientation.

3.2.1 Cleaning Protocol

Experimental environment for achieving π-A isotherm graph and film deposition were maintained in a class 1K-cleanroom (Low Dimensional Research Centre, LDMRC, Department of Physics, Faculty of Science, University of Malaya). rGO LB film deposition is achieved using a round type NIMA LB trough model 2200 (NIMA Technology U.K). Ultra-cleaning protocol was performed before commencing this experiment. For typical LB experiment, chloroform is used as the cleaning reagent. However, in this experiment, the cleaning reagent used was methanol. rGO will not be removed properly from the surface of Polytetrafluoroethylene (Teflon) if chloroform was used. The LB trough was cleaned using dust free tissue (Kimpwipes, KIMTECH) moistened with methanol. A micro syringe (± 2 μL) was cleaned by filling and expelling it with methanol. This step was repeated three times to ensure the syringe was properly cleaned. Filtered deionized (DI) water as subphase was used to fill the LB trough until meniscus of water can be seen. The meniscus of water is essential to prevent the monolayer on top of subphase from passing under the barrier. DI water was used to minimize dust and other contamination. To further clean the surface, aspiration technique was used to clean the water surface. This was done by simply vacuuming out the free standing dust particles and other contaminants on the water surface through a pipette tip attached to a silicon tube connected to the aspirator pump.

Next, the barrier was opened up to an area of 500 cm^2 and the pressure sensor reading zeroed. The latter process is to adjust the current surface tension to be defined as zero surface pressure to eliminate the water surface pressure. Hence, the data recorded during the compression experiment is the actual surface pressure of the monolayer only. π-A isotherm was then taken without any surfactants at the air-water interface with the barrier speed of 100 cm^2/min. If the surface pressure is increased, the water surface is not thoroughly clean and the aspiration technique is repeated until an almost flat isotherm graph at abscissa is obtained.

3.2.2 Isotherm Graph and Dip-coating Mechanism

This section is divided into two parts. First is the protocol to obtain the π-A isotherm graph. Second part involves the process of dip-coating. Information obtained from the isotherm graph in the first part was used in the second part for determining the target pressure, enabling the process of dip-coating to be carried-out.

For monitoring the pressure changes of the monolayer during compression, a Whatman filter paper attached to a tensiometer with a dimension of (1.0 x 2.2) cm^2 was dipped about ½ or ¾ into the water. An aliquot of 1000 μL of rGO and 99% pure methanol solvent (Chromasolv HPLC, Germany) were spread on the DI water surface by using a clean micro syringe to form a monolayer. The monolayer was left to self-stabilize for about 15 minutes. During the period of self-stabilization, sometimes it is observed that smaller rGO flakes get attached or stacked to form larger area rGO flakes creating a clouded area on the Langmuir film. Hence, a dust free tissue (Kimwipe, USA) was wetted with methanol and its vapour spread against the monolayer from a distance of 0.5 cm from the monolayer surface. This helps to reduce the clouded area of the rGO Langmuir film at the water surface, assisting in the uniform distribution of the rGO layers. The barriers were then set to compress at a speed of 15.0 cm^2/min. Upon compression, the isotherm graph was continuously recorded until the barriers haveclosed to the determined minimum area to avoid crashing with the filter paper. The generated graph represents the gaseous, liquid, solid, and breaking states of the rGO monolayer and can also be extracted and represented in terms of the intermolecular force between molecules.

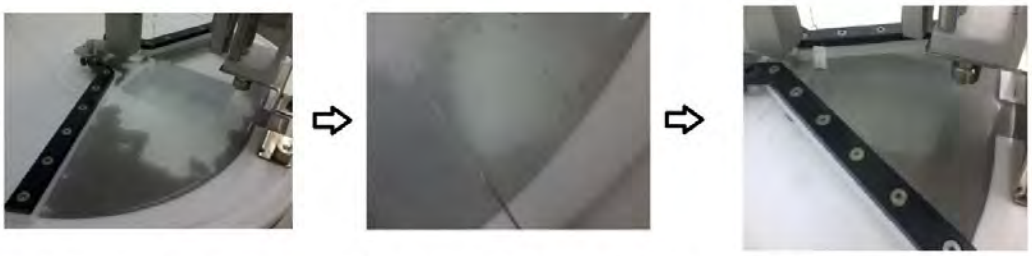

(i) rGO spread on top of water subphase

(ii) Using methanol vapour method to assist spreading of rGO

(iii) Compression mechanism

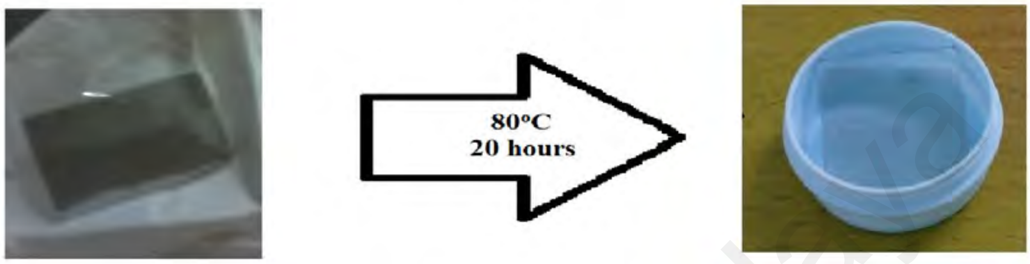

(iv) rGO layer deposited on glass

(v) Thermal heat at 80°C for 20 hours

(vi) rGO thin film final product

Figure 3.2: Dip-coating and annealing process.

For the dipping mechanism, the protocol to obtain isotherm graph is repeated but the compression of the barriers is halted and maintained at the pre-determined target pressure. Then the dip-coating method was applied to deposit a monolayer thin film on the substrate. Traditionally, the pre-determined target pressure was chosen and carried-out at the solid-state region as the deposition after breaking point does not allow formation of true monolayer. However, for obtaining 3D rGO layer, an unconventional protocol was developed by carrying-out the dipping process after the collapse pressure or breaking point. At the target pressure of 15 mN/m, a glass substrate (2.5 × 2.5) cm^2 was vertically dipped at a speed of 20 mm/min. If the dipping speed is faster than this, then the film is not attached effectively to the glass. The rGO layer was then transferred onto the substrate during the dip-coating process. The prepared substrate with rGO layer was dried in an oven overnight (8-20 h) at 80°C to remove water and to stabilize the adhesion of the rGO layer. Subsequent layer deposition was achieved after overnight air-drying to prevent peeling off of the underlying rGO layers. This process was repeated for another 10 times of dipping.

3.3 Preparation of rGO-Algae Biofilm

Chlorella sp. from University Malaya Algae Culture Collection (UMACC 313) was grown in Bold's Basal Medium. The culture was placed into a 200 mL sterile jar glass, which has 100 ml of exponential phase cultures of 0.5 ($OD_{620\ nm}$). ITO (KINTEC, Hong Kong) with thickness of 100 nm, 3770 Ω/sq sheet resistance, and 104 S/sm of conductivity were used for comparison. ITO and rGO on glass substrate was prepared in dimensions of (3.5 x 3.5) cm. Both electrodes were prepared in triplicates and sterilized using UV light for two hours.

The ITO and rGO substrate were placed in a staining jar with the microalgae and transferred into an incubator at 24°C and illuminated with white fluorescent lamps (30 $\mu mol.m^{-2}.s^{-1}$) on a ratio of 12:12 hours of light-dark cycle. This process will allow algae biofilms to form on the substrate. The algae biofilms on rGO and ITO were then left to grow for 15 days and achieve complete optimum surface area coverage.

3.4 BPV Devices Set-up and Electrical Measurement

A single chamber of BPV consists of (50 x 50) mm platinum-coated carbon as the cathode. The cathode was placed parallel with the ITO or rGO coated with the algae biofilm as shown in Figure 3.3. Body of the chamber were made of Perspex and sealed with polydimethylsiloxane (PDMS). The cavity in the middle was filled with Bold's Basal Medium together with algae. Copper wires were attached to both electrodes (anode and cathode) as the connection to the external circuit.

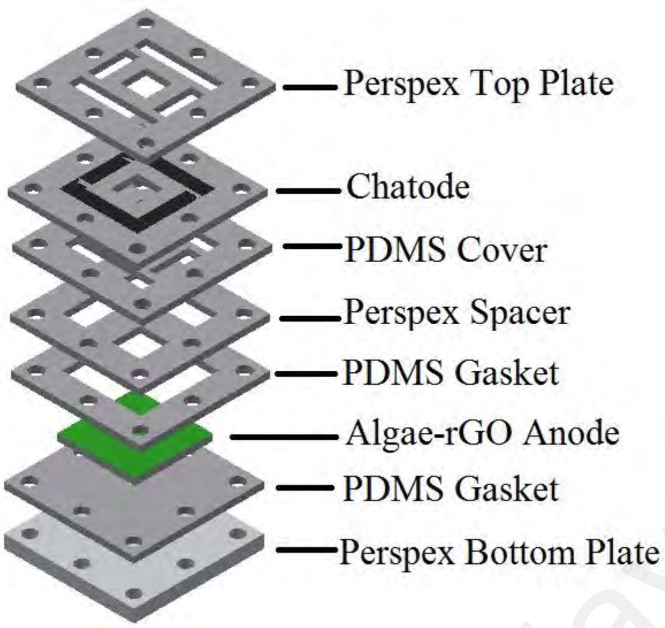

Figure 3.3: Exploded diagram of the BPV platform.

The chamber was filled with a fresh medium, maintained at 25°C, and placed under a fluorescent lamp irradiance of 30-μmol.m^{-2}s^{-1} was used for the duration of light cycle of the experiment. For the dark cycle experiment, the BPV devices were placed in a dark room without any light source. For confirmation, a light meter (LI-250A, Licor) was used to measure the light intensity to confirm that the reading is zero. Current measurement meanwhile was carried-out by using a multimeter (Agilent U1251B). Polarization curve was plotted for each anode by applying different resistances (10 MΩ, 5.6 MΩ, 2 MΩ, 560 KΩ, 240 KΩ, 62 KΩ, 22 KΩ, 9.1 KΩ, 3.3 KΩ and 1.1 KΩ) loaded to the external circuit.

3.5 Structural Characterization

A Field Emission Scanning Electron Microscope (FESEM, Quanta FEG-450, and Hitachi S-4500) was used to study the surface morphology and structure of rGO LB film. Atomic Force Microscopy (AFM) and Scanning Probe Microscope-Nanoscope in non-contact mode (AMBIOS v5.0.0) were used to study the thickness and the porosity value of the film. Transparency of the film was measured using a UV-Vis spectroscopy (Perkin Elmer Lambda 750), while sheet resistance was measured by the four-point probe method (Jandel Universal Probe Station).

Electrochemical measurements were performed in a 30 ml single compartment electrochemical cell containing three electrodes, using a micropotentiostat (µAUTOLABIII/FRA2, Metrohm Autolab B.V., UK) connected to a computer. The 3D rGO film deposited with 6 deposition layers on a glass slide was used as the working electrode while a (5.0 x 5.0) cm platinum foil was used as the counter electrode. A silver chloride ($Ag/AgCl/Cl^-$) electrode immersed in a compartment containing saturated potassium chloride from Bioanalytical Systems, Inc., USA, was used as a reference electrode. The solution used for these experiments was a 0.1 M potassium phosphate buffer solution at pH 7.0 prepared with potassium phosphate monobasic and potassium phosphate dibasic trihydrate (Sigma-Aldrich, UK).

3.5.1 Field Emission Scanning Electron Microscopy

Scanning Electron Microscope (SEM) is a technique to study the structure of molecular surface by scanning it with a focused beam of electrons. While the electron beam traces over the object, it interacts with the atom at the surface and forces out the secondary electrons scattering them. The secondary electron detector attracts the scattered electron and the level of brightness of the image depends on the number of the electrons that reaches the detector.

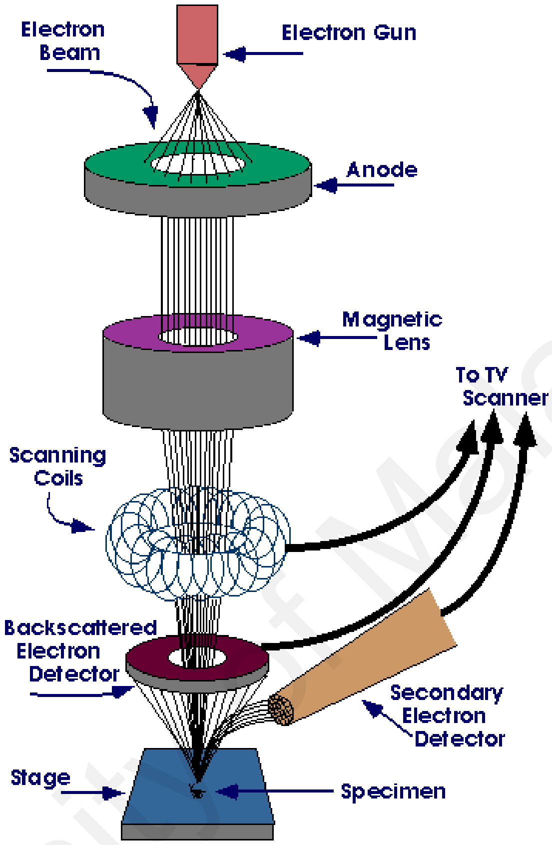

Figure 3.4: A schematic diagram of FESEM device (Tloughran, 2011).

The source of electrons in SEM is produced from a field emission gun consisting of a sharp tip (<0.1 µm), and usually made from tungsten as the cathode and two anodes (which is the extraction and acceleration anodes). A high voltage is applied across both the cathode and anode, which will affect the electrons through the energy barrier of tungsten tip into the vacuum. Extraction anode (0 – 5 kV) extracts the electron and acceleration anode (1 – 50 kV) accelerates the electron depending on the applied voltage. The electromagnetic lens are operated and focused on the electron beam by applying magnetic field to a horizontal radical path. The scanning coil by adjusting current through radially oriented coils deflects the electron beam to the sample. A digital format or image is interpreted by detecting and measuring the signal by using the electron detector in the system. The signal that interact with the sample atoms originate from the incident beam with energy of few hundred eV to 50 keV. A few examples of the FESEM images generated in these studies are shown Figure 3.5.

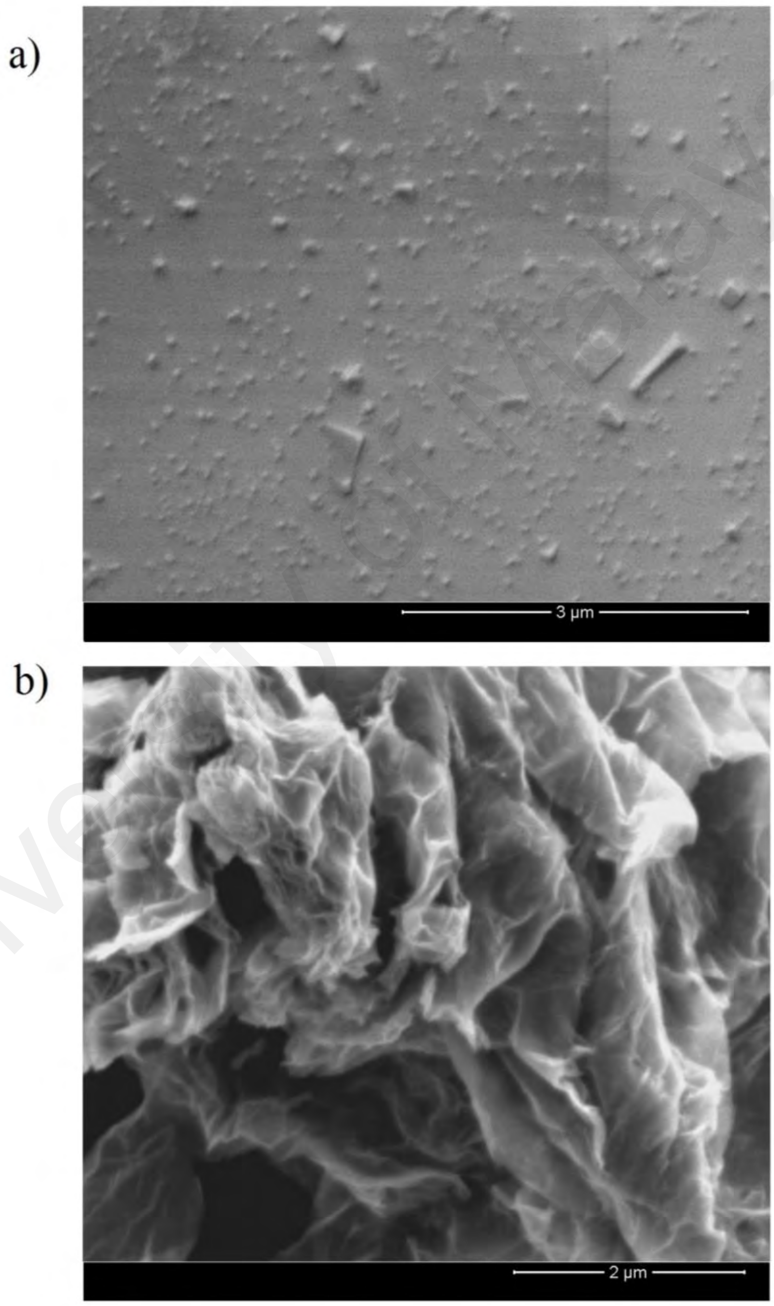

Figure 3.5: Typical FESEM images of (a) treated glass and (b) rGO flakes.

3.5.2 Atomic Force Microscopy

AFM is a high-resolution type of scanning probe microscopy technique that will resolve up to a fraction of a nanometer. It consists of a cantilever with a sharp tip (probe) that is used to scan the sample surface. Typically, the cantilever is silicon or silicon nitride with the tip radius of curvature on the order of nanometers. The mechanism of the measurement is according to Hooke's law. That is, when the tip is bought into proximity to a sample surface, the force between the tip and the sample will cause a deflection of the cantilever.

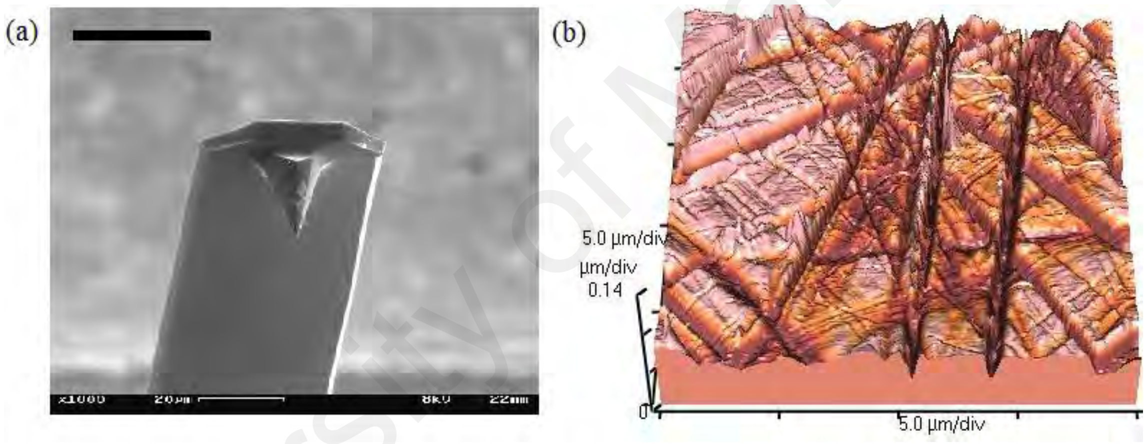

Figure 3.6: (a) Image of AFM cantilever with a width of ~100 micrometers. (b) Typical AFM topographical scan of a glass surface (*Atomic-force microscopy*, 2008).

Typically, a laser is used to spot the deflection and measure the reflection from the top surface of the cantilever by arrays of photodiodes. Alternative methods for the mechanism are by using optical interferometry, capacitive sensing, or piezoresistive AFM cantilever (which is the cantilever fabricated using piezoresistive element and act as a strain gauge). AFM mode can be described into three modes depending on the nature of the tip motion. It is described as contact, tapping, and non-contact modes.

Contact mode is referred as the mechanism of the tip that is “dragged” across the surface of the sample and the contour of the sample measured either using deflection of the cantilever or feedback signal required to keep the cantilever at a constant position. While tapping mode is developed by driving the cantilever to oscillate up and down near its resonance frequency by a small piezoelectric element mounted at the AFM tip holder, which is similar to non-contact-mode. However in ambient mode, it is highly possible that the sample will develop a liquid meniscus layer. By keeping the probe tip close enough to the sample for the short-range force to become detectable while preventing the tip from sticking to the surface, it presents a major problem for the non-contact dynamic mode in ambient conditions. Furthermore, in tapping mode, the amplitude of the oscillation is greater than 10 nm, typically 100 to 200 nm. Hence, the interaction of force acting (van der Waals forces, dipole-dipole interactions, electrostatic force, etc) on the cantilever when the tip comes close to the surface will cause the amplitude of the oscillation to decrease as the sample and the tip gets closer. Therefore, an image will be produced by determining the force of the intermittent contact of the tip with the sample surface.

For non-contact mode, the tip of the cantilever does not contact the sample surface at all. Instead, the cantilever is oscillated at either its resonant frequency (frequency modulation) or above (amplitude modulation). The amplitude of oscillation is just typically a few nanometers (less than 10 nm) to a few picometers from the sample.

The van der Walls force (being the strongest force at 1 to 10 nm above the surface), or any other long-range force that covers above the surface will act to decrease resonance frequency of the cantilever. Hence, the combination of decrease of resonance and feedback loop system are to maintain a constant oscillation amplitude or frequency by adjusting the average tip to sample distance. From the information of tip-to-sample distance of each (x,y) data points, a topographic image of the sample surface can be constructed. An amplitude modulation, which is also being used in a non-contact method to image with atomic resolution, the change in oscillation amplitude or phase will provide a feedback signal for imaging. Change in the oscillation phase is used to discriminate between different types of materials.

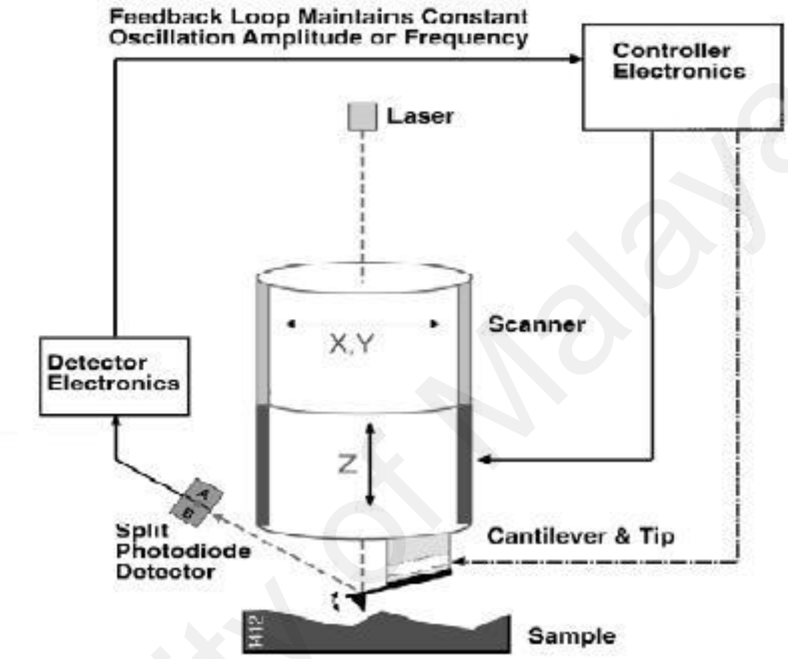

Figure 3.7: Typical set-up of AFM for non-contact mode (*Atomic-force microscopy*, 2008).

3.5.3 Ultraviolet-visible Spectroscopy

UV-Vis is referred to as absorption (and transmission) of spectroscopy or reflection spectroscopy in the UV to the visible spectral region. Both mechanisms of absorption and reflection are invisible ranges that reflect to the colour of the chemical involved and in this region of electromagnetic spectrum, molecules undergo electronic transition. In principle, a molecule containing π-electron or non-bonding (n-electron) may absorb energy from UV and visible light spectrum to excite this electron to higher anti-bonding molecular orbits. An electron that has a lower energy gap between HOMO (highest occupied molecular orbital) and LUMO (lowest unoccupied molecular orbital) is easier to be excited. Hence, it can absorb the longer wavelength of light.

For measurement of absorption, when light passed through a sample (I), the intensity of the light will be measured and compared with the intensity of light before it passed through the sample (I_o). The ratio of the light intensity before and after passing through the sample is measured (I/I_o) and denoted as its transmission commonly expressed as percentage (%T). Absorbance, A is calculated from the transmission values using the equation below;

$$A= -\log (\%T/100\%) \qquad (3.1)$$

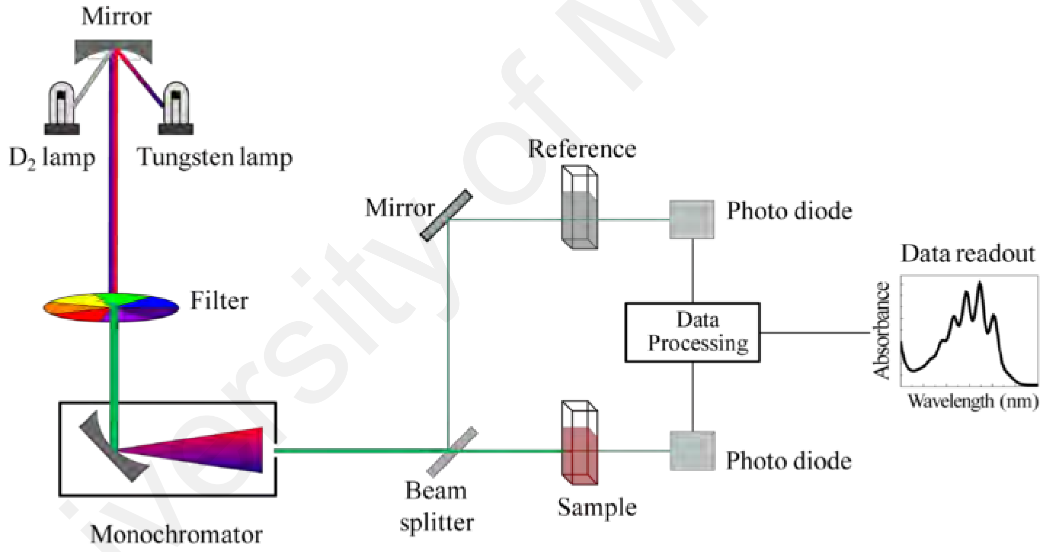

Figure 3.8: Typical schematic set-up of UV-Visible spectrophotometer (*Ultraviolet–visible spectroscopy*, 2005).

For the measurement of reflection, the spectrophotometer measures the intensity of light reflected from the sample (I) and compares to the intensity of light reflected from the sample (I_o). The ratio I/I_o is commonly expressed in percentage and called as reflectance (%R).

3.5.4 Raman Spectroscopy

Raman spectroscopy technique is used to detect vibrational, rotational, and other low-frequency modes in a system and can be used to fingerprint molecules. A typical spectrum is as shown in Figure 3.9, the measurement obtained for one of the samples from the current work. The technique depends on inelastic scattering (Raman scattering) of monochromatic light, which is usually laser in the visible, near infrared, or near ultraviolet range. Typically, a laser wavelength of 632, 514, and 525 nm are commonly used in Raman spectroscopy. The photon (from a laser) interacts with molecular vibrations, or phonon, or other excitation system causing the energy of the photon to be shifted down or up. Generally Argon, Ar^+, or Krypton, Kr^+ ion laser is used for visible range, and yttrium aluminium garnet laser is used for ultraviolet range laser. The shift change of energy provides information about the vibrational modes in the system.

A laser is illuminated at the sample, and electromagnetic radiation from the illumination spot was collected with a lens and guided through a monochromator. The elastically scattered radiation at the wavelength will correspond to the laser line, which is Rayleigh scattering, being filtered out, while the rest of the collected light was spread onto a detector filter (notch filter or band pass filter). A Raman shift is commonly recorded in wavenumbers where the unit is reported as units of inverse length, which is directly related to energy;

$$\Delta w=\left(\frac{1}{\lambda_o}-\frac{1}{\lambda_1}\right) \tag{3.2}$$

The formula (3.3) is used to convert between spectral wavelength and wavenumber, where Δw, is the expression in wavenumber, and λ_1 is the Raman spectrum wavelength. The unit for Raman shift was denoted as inverse centimeters, cm^{-1}. Conversion from wavelength (using units of nm) to the inverse centimeter is given in the formula in next page;

$$\Delta w(\text{cm}^{-1}) = \left(\frac{1}{\lambda_o(\text{nm})} - \frac{1}{\lambda_1(\text{nm})}\right)\left(\frac{10^7\text{nm}}{\text{cm}}\right) \quad (3.3)$$

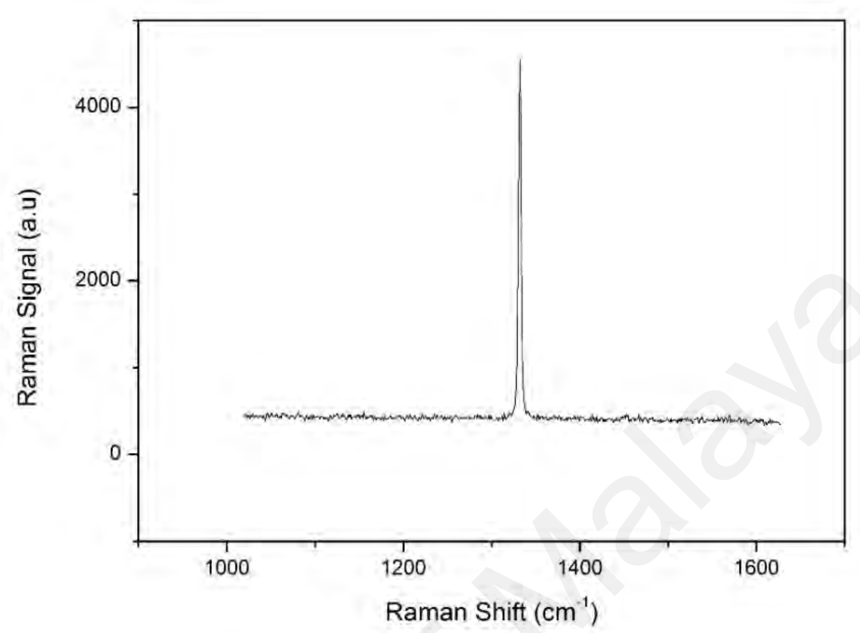

Figure 3.9: Typical image of Raman spectra for glass substance.

3.5.5 Four-Point Probe

A four-point probe as shown in Figure 3.10 is an apparatus for measuring the resistivity of semiconductor type sample. It is a method of the electrical impedance measuring technique where current carrying pairs are separated with voltage sensing pairs. This set-up will allow the electrode sensing to be more accurate than the conventional two terminal sensing. The technique of separation of current and voltage electrodes will eliminate the lead and contact resistance from the measurement making it more precise to measure low resistance values. The mechanism involves simply passing current from the two outer probes and measuring the voltage through the inner probes. This arrangement will allow the measurement of the substrate resistivity. Other than that, it could also measure bulk resistivity and sheet resistant. Four-point probe measurement must be kept in the dark. From resistivity information, the measurement of sheet resistance could be derived according to the equation in next page;

$$\rho_s\left(\frac{\Omega}{\mathrm{sq}}\right)=\frac{\pi}{\ln(2)}\frac{V}{I} \tag{3.4}$$

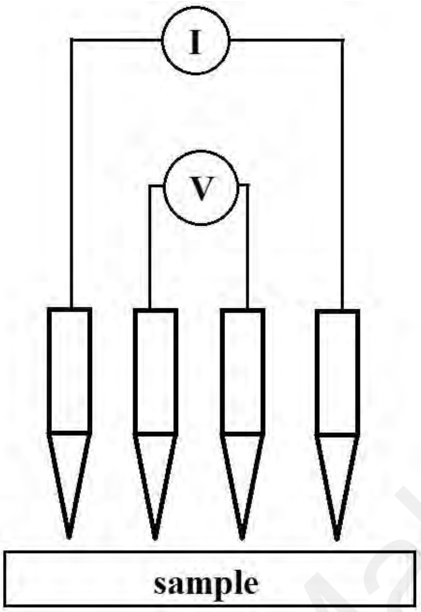

Figure 3.10: A schematic diagram of the four-point probe.

3.5.6 Electrochemistry Analysis

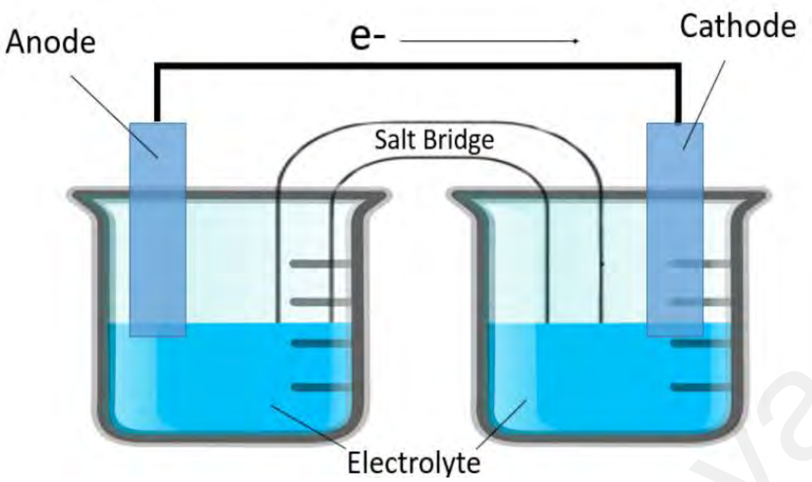

Figure 3.11: Schematic diagram for redox reaction in electrochemical reaction.

Electrochemistry is a study of electricity and it relations to the chemical reaction (Bard; et al., 2001). In the electrochemistry discipline, electricity can be generated by movements of electrons from one element to another in a reaction known as a redox reaction or oxidation-reduction reaction (Figure 3.11). It is illustrated as a process including electron transfer to molecule or ion, or electron transfer from molecule to an ion, which is changing its oxidation state. This reaction can take place by the application of an external voltage or by the release of the chemical energy (Darvas et al., 2014). Typically, the oxidation state is described as the hypothetical charge any atom would take if all the bonds to atoms of the different element were 100% ionic. The oxidation state will increase if the atom or ion transfers its electron to another ion or atom. Hence, the receiver of the negative charge of electron will decrease its oxidation state (ĖVarestov, 2007).

3.5.6.1 Standard Electrode Potential

Standard electrode potential (SEP) is used for prediction of the cell potential. It is referred to as the tabulation of standard hydrogen electrode (SHE). It undergoes the following reaction;

$$2H^+_{(aq)} + 2\ e^- \rightarrow H_2$$

However, the SHE can act either as an anode or cathode as it depends on its oxidation/reduction potential to the other electrode/electrolyte combination. It is required that the SHE obtain a supply of hydrogen gas bubbled trough the electrolyte at a pressure of 1 atm and an acidic electrolyte with H^+ activity equal to 1. Typically, it will be assumed that $[H^+] = 1$ mol/liter (Averill et al., 2013).

SEP for the electrode is measured when the cell potential is at a condition where SHE electron is able to connect to any other electrodes by salt bridge for forming a cell, while the second electrode is maintained at a standard condition. By classification, the SEP for the SHE is zero. Compared to SHE, the polarity of the SEP could provide information about the relative reduction potential of the electrode. Hence an electrode, which has a positive potential with respect to the SHE will be denoted as a strongly reducing electrode forcing the SHE to become an anode. Furthermore, if the potential was measured to be negative, it means that the electrode is oxidizing more than the SHE (Averill et al., 2013).

3.5.6.2 Cyclic Voltammetry

One of the most valuable techniques in electrochemistry is the voltammetric technique, also known as cyclic voltammetry (CV). It is a technique for acquiring qualitative information about the electrochemical reactions involved. It represents the fast identification of redox potentials distinctive of the electroactive species, providing significant information about the thermodynamics of redox process, kinetics of the heterogeneous electron transfer reaction, and study of the coupled electrochemical reactions of adsorption processes. CV technique contains scanning of the potential (linearly) of working electrode using a triangular potential wave form which can be referred in Figure 3.12 (Averill et al., 2013).

A potential is swept from E_1 to E_2 at the rate which is typically measured in V/s. Voltammetric scan rate is also known as the gradient of the line (Figure 3.12). A linear sweep experiment is defined as the potential stops at E_2, while the CV is defined as the scan rise to E_2, and back to E_1, which is a full potential cycle. This experiment can be performed in a single cycle or multiple cycles. During the duration of potential sweep, the potentiostat measures the resulting current that is escalated via the applied voltage (potential). Hence, the graph of the current versus potential (voltage) is designated as CV (Averill et al., 2013).

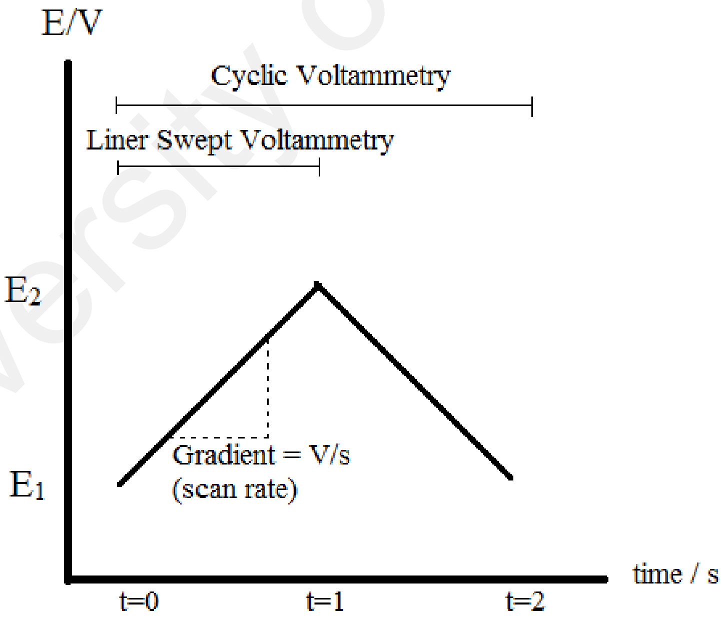

Figure 3.12: Graph of CV from linear current versus potential.

CHAPTER 4

RESULTS AND DISCUSSIONS

4.1 rGO LB Film

4.1.1 Preparation of the rGO LB Film

Generally, chloroform (nonpolar solvent) is the best candidate as a volatile solvent for diluting substance. It is widely used in organic and inorganic substance for spreading the substances on top of the water subphase. However, for rGO flakes, a methanol (polar alcohol) was selected because rGO tends to collapse and adopt 3D compact confirmation in nonpolar solvents (Wen et al., 1992). Apart from that, methanol was also used to assist in the rapid spreading of rGO on top of the water surface (Figure 4.1) (Zheng et al., 2011). The size of rGO flakes varies causing smaller flakes to sometimes get attached or stacked to larger area flakes forming a clouded area on the Langmuir film (Cote et al., 2009; Zheng et al., 2011). Due to the nature of methanol that will evaporate at room temperature (25°C), the vapour mechanism methanol was applied to the clouded areas by using a methanol soaked tissue. The resulting methanol vapour from the tissue uniformly disperses the rGO flakes, which could be due to the effect of nonpolar molecules toward the rGO flakes (Wen et al., 1992).

After the dipping mechanism was achieved, the rGO film needs to be dried at 80°C overnight inside the oven (approximately 8-20 hours) before carrying-out multilayer deposition. A wet rGO film tends to peel off from the glass substrate upon insertion and withdraw into the water subphase. It is because the rGO flakes still contain water and tend to spread back from the substrate into the water following its natural polar behaviour if it was dipped immediately. Heat treatment of rGO film will increase the adhesion. This process of drying and deposition was repeated for each subsequent layer formation until the required number of multilayers was achieved.

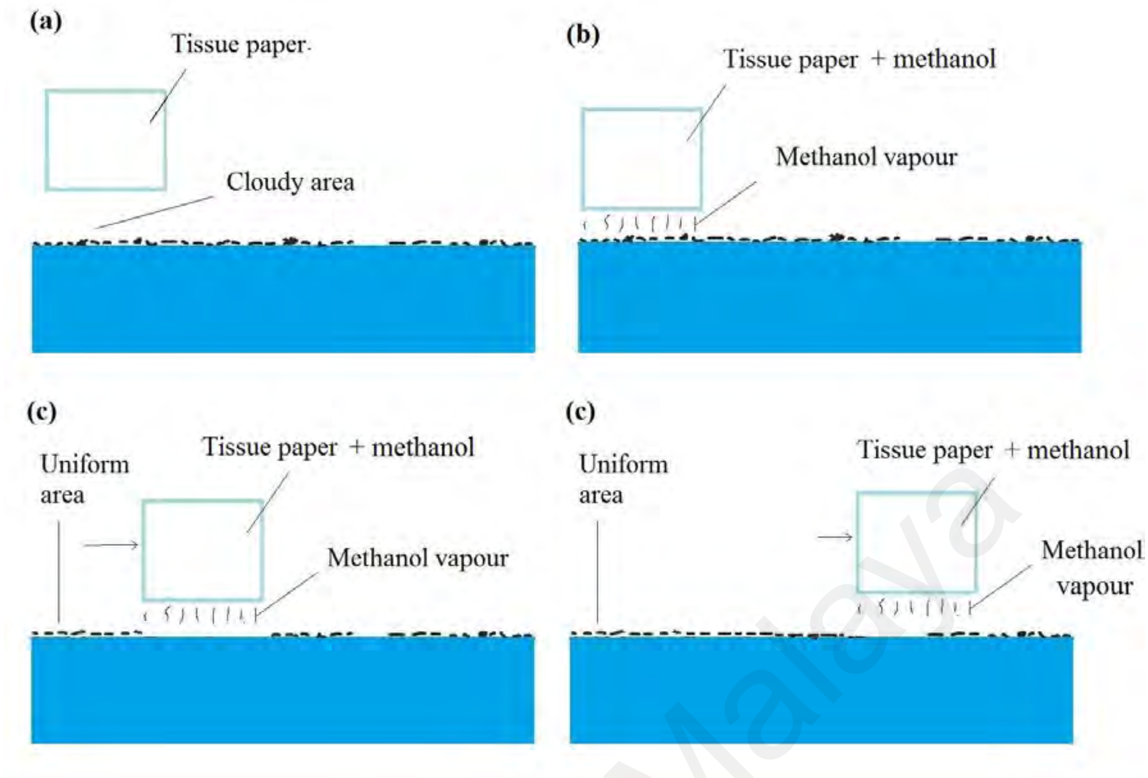

Figure 4.1: Methanol vapour mechanism using a tissue.

4.1.2 Isotherm Analysis

The π-A isotherm recorded three major phase transitions from gaseous into liquid states (Figure 4.2). From the beginning of stage A, the monolayer exists in gaseous state with the rGO flakes dispersed widely on the water surface. Surface pressure remains constant during compression because intermolecular force between them remains zero as the rGO flakes rarely touch each other. The pressure reading starts to increase (stage B) as the rGO layers begin to touch each other and intermolecular forces becomes apparent. In this stage, the monolayer density at the water surface starts increasing. There are two fundamental types of geometric interactions between the rGO layers, namely edge-to-edge and face-to-face (Cote et al., 2009). Upon continuous compression, the liquid phase undergoes a transition to an even higher density and the monolayer reaches the solid state (stage C) as the rGO flakes appear to be in close-pack arrangements.

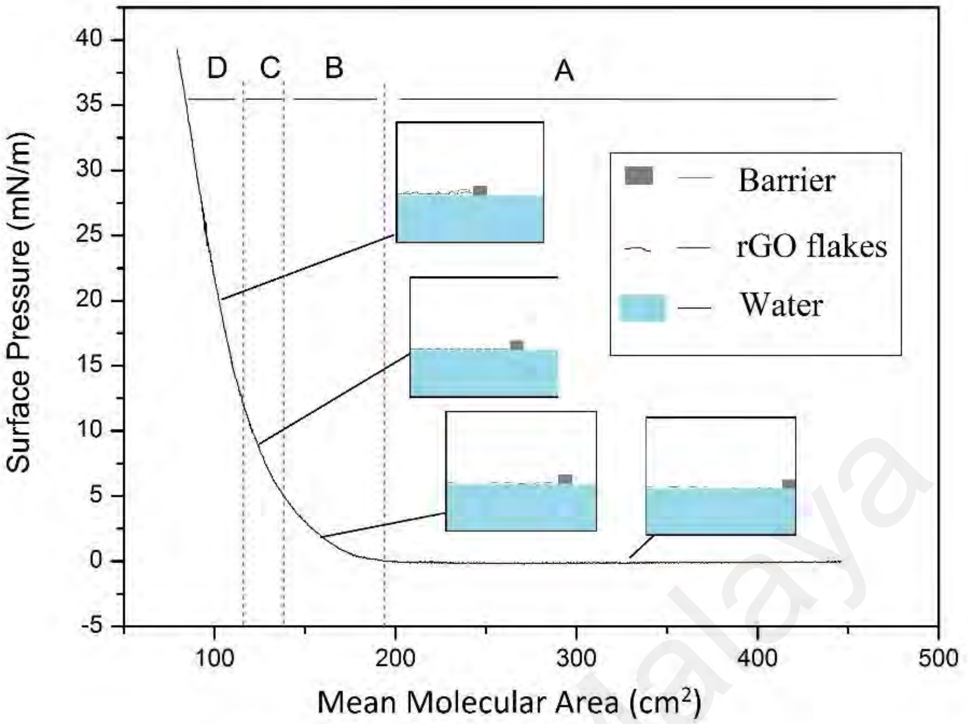

Figure 4.2: Surface pressure versus mean molecular area isotherm showing the four stages of compression; gaseous state (A), liquid (B), solid states (C), and breaking point (D).

At stage D, further compression of rGO monolayer beyond close pack state will cause the density to increase beyond the limit collapsing the monolayer. Collapse of the rGO monolayer creates multilayer formation and wrinkling as shown in Figure 4.5(a). The wrinkling effect in collapsed state was observed to be more significant than wrinkling in the solid state as shown in Figure 4.5(b). Manipulation of 2D structures into the 3D film can be carried-out at this point by performing the dipping process at this collapsed state followed by layer-by-layer deposition.

4.1.3 Analysis of the Intermolecular Force

Even though the π-A isotherm profile in Figure 4.2 did not show any significant difference between the breaking point and solid state regions or showing crashing pattern slope, the rGO layer on top of water can still be seen clearly to collapse at certain pressure using the naked eyes. Hence, the intermolecular force profile for rGO could be used for clearly indicating the difference between these regions.

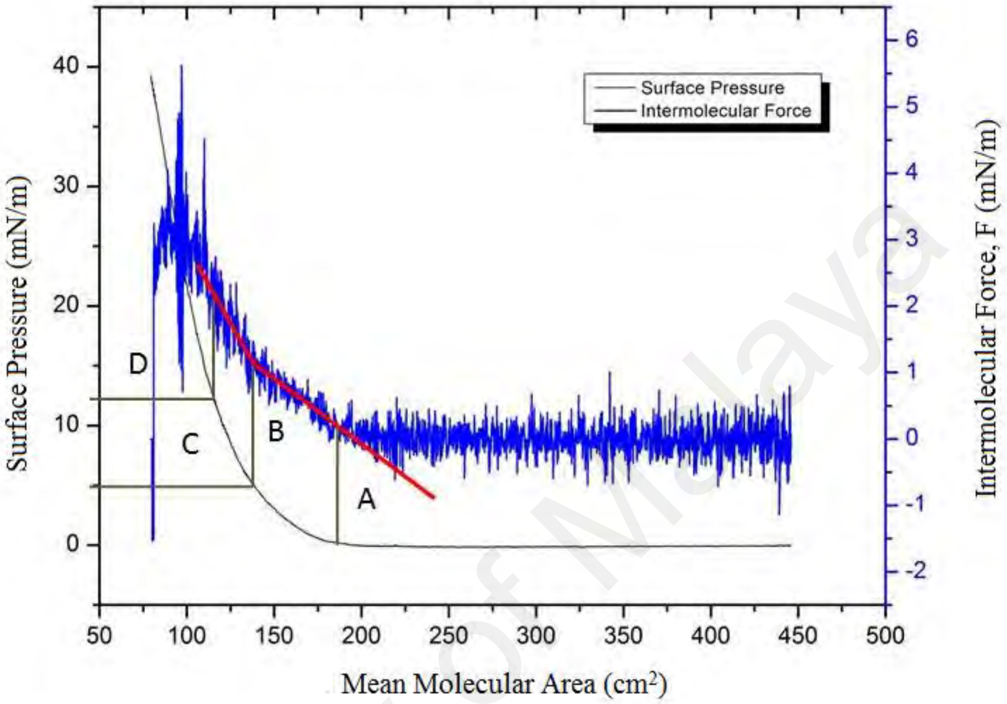

Figure 4.3: Surface pressure-area isotherm and elastic modulus of rGO at air-water interface.

The intermolecular force between molecules could be extracted from the isotherm graph by using equation (2.4) Values of the intermolecular force graph were compared with the isotherm graph providing useful information for determining the phase of the monolayer as shown in Figure 4.3 (Periasamy, 2012). From the intermolecular force pattern, it can be clearly shown that the transition of liquid to solid state region occurs at 5 mN/m. In Figure 4.3, it is represented as the transition of region B to region C. Breaking point around 12.5 mN/m and above are clearly shown in region D. The values obtained in this work also agree well with Yang et al, who also reported similar surface pressure versus area graphs (Cote et al., 2009; Yang et al., 2014; Zheng et al., 2013).

4.2 Surface Morphology Studies

4.2.1 Wrinkling Effect

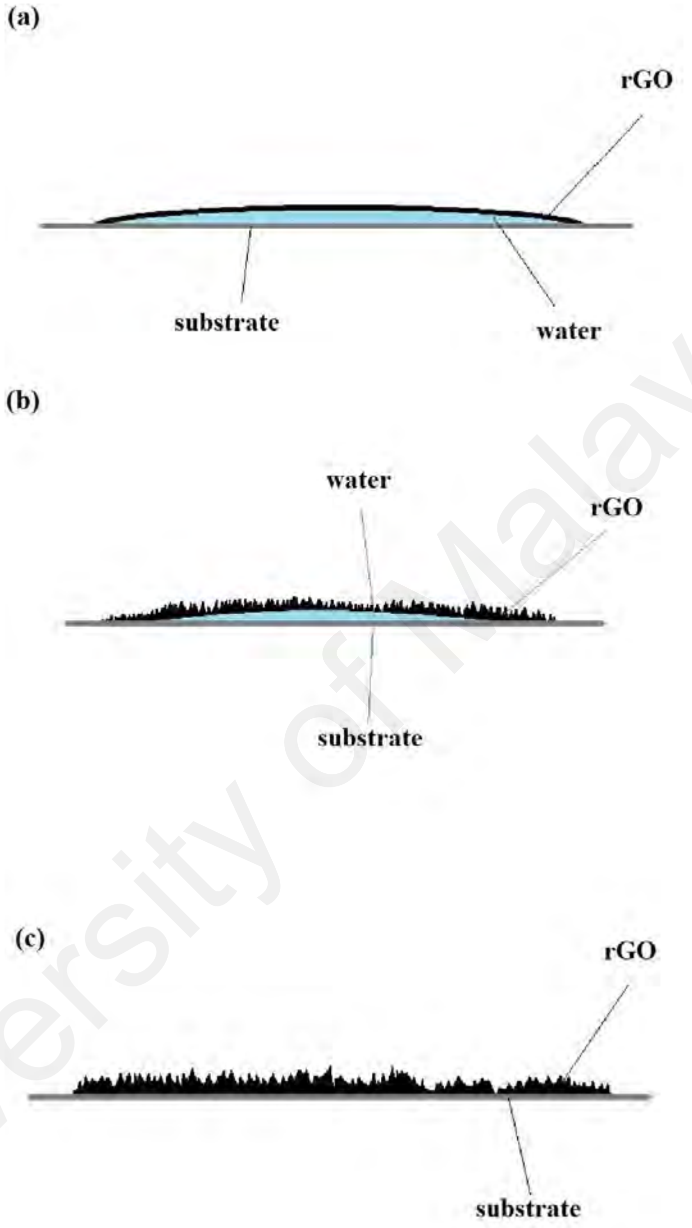

Figure 4.4: Schematic diagram explaining the occurrence of the wrinkling effect due to the capillary and gravitational forces.

A wrinkle occurs during compression at the close pack arrangement (region C) and continuously through the critical point. It is because the electrostatic repulsion between 2D layers (Cote et al., 2009) pushed each other creating wrinkles at the rGO flakes. The effect can be observed clearly on the FESEM image in Figure 4.6(a). Other than that, capillary and gravitational forces also contributed to the wrinkle effects when water evaporates during the drying process (Figure 4.4) (Zheng et al., 2011).

While transferring onto the glass substrate, molecules of water adhere to the glass allowing the rGO monolayer to float as shown in Figure 4.4(a). Water provides higher surface area prior to drying, resulting in more space for the flakes to float and rearrange themselves uniformly as illustrated in Figure 4.4(b). During the drying process, evaporation process occurs from all areas of the water surface. However, water at the edge dries faster than the middle region due to its water level thickness being thinner than at the middle. After complete drying, rGO compresses together and creates wrinkles in nanoscale due to insufficient space and gravitational rearrangement (Zheng et al., 2011) as illustrated in Figure 4.4(c), resulting in surface porosity as seen in the FESEM image (Figure 4.5(b)).

4.2.2 Dipping in Solid and Breaking Point Regions

Since 1935, when Katherine Blodgett (Blodgett, 1953) completed the LB technique, deposition of homogenous LB film has conventionally been carried-out at the solid state region for obvious reasons. Once the over compression of the monolayer reaches a breaking point, the experiment had to be repeated again by replacing and cleaning the water and film layers. It is because, at the breaking point, monolayer tends to stack on top of each other, or sink, or collapse into a multilayer structure.

This state is considered to be the least favorable state due to the non-homogenous film obtained if the dipping was done at this stage. However, the key to obtaining a high porosity rGO film can be achieved by carrying-out the deposition mechanism at this breaking point region.

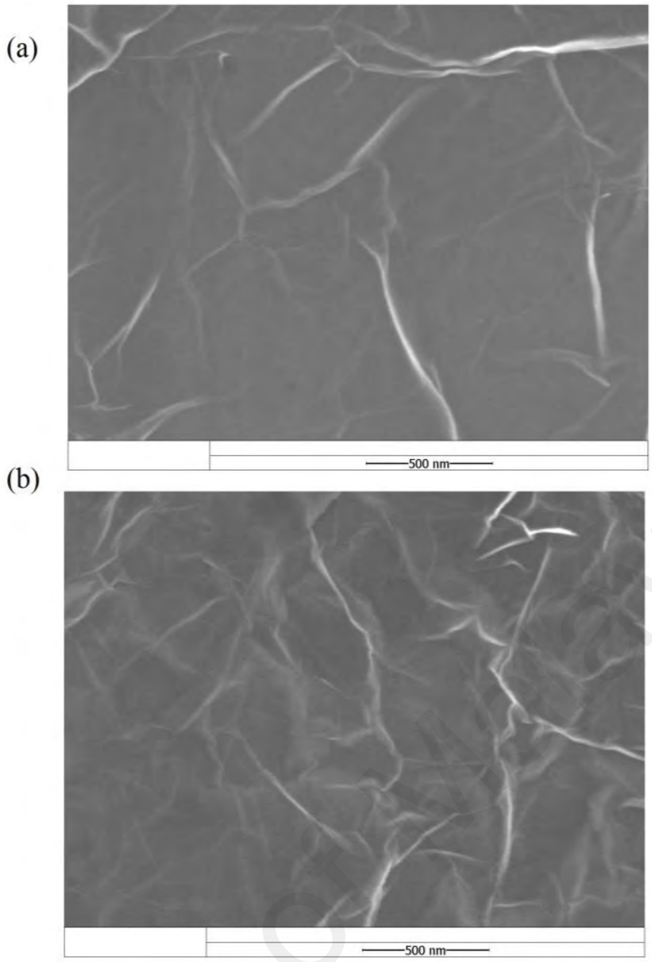

Figure 4.5: The surface morphology of one layer rGO film deposited at the solid state (a), and breaking point (b).

As can be seen from Figure 4.5(a), the film formation shows a very smooth film with less porosity compared to Figure 4.5(b) when the film was obtained at the breaking point. The uniformity of the film can be observed in Figure 4.6(c), while Figure 4.6(a) shows a wrinkle that normally is observed in any graphene (Xiuyi et al., 2012) or GO (Zheng et al., 2012) films prepared using the LB method.

4.2.3 Analysis of rGO Film Deposited at Collapse Pressure

A highly porous rGO film (Figure 4.6(c)) can be instrumental for attachment of biomaterials such as deoxyribonucleic acid (DNA), enzyme and protein molecules (De et al., 2011; Liu et al., 2013; Tan et al., 2013). The uniformity of the micron scale film porosity was observed to be prominent probably due to the manipulation of the compressive pressure. AFM image in Figure 4.6(d) clearly show the 3D wrinkle structure, which results in the increase in the average thickness of a single flake of the graphene film to 6.18 nm compared with the theoretical value, which is 0.5 nm (Cote et al., 2009). Wrinkle effect can be reduced (Figure 4.6(b)) by means of thermal annealing at 350°C for 20 hours under vacuum condition for achieving a flatter film for other applications (Becerril et al., 2008; He et al., 2011; Yang et al., 2013).

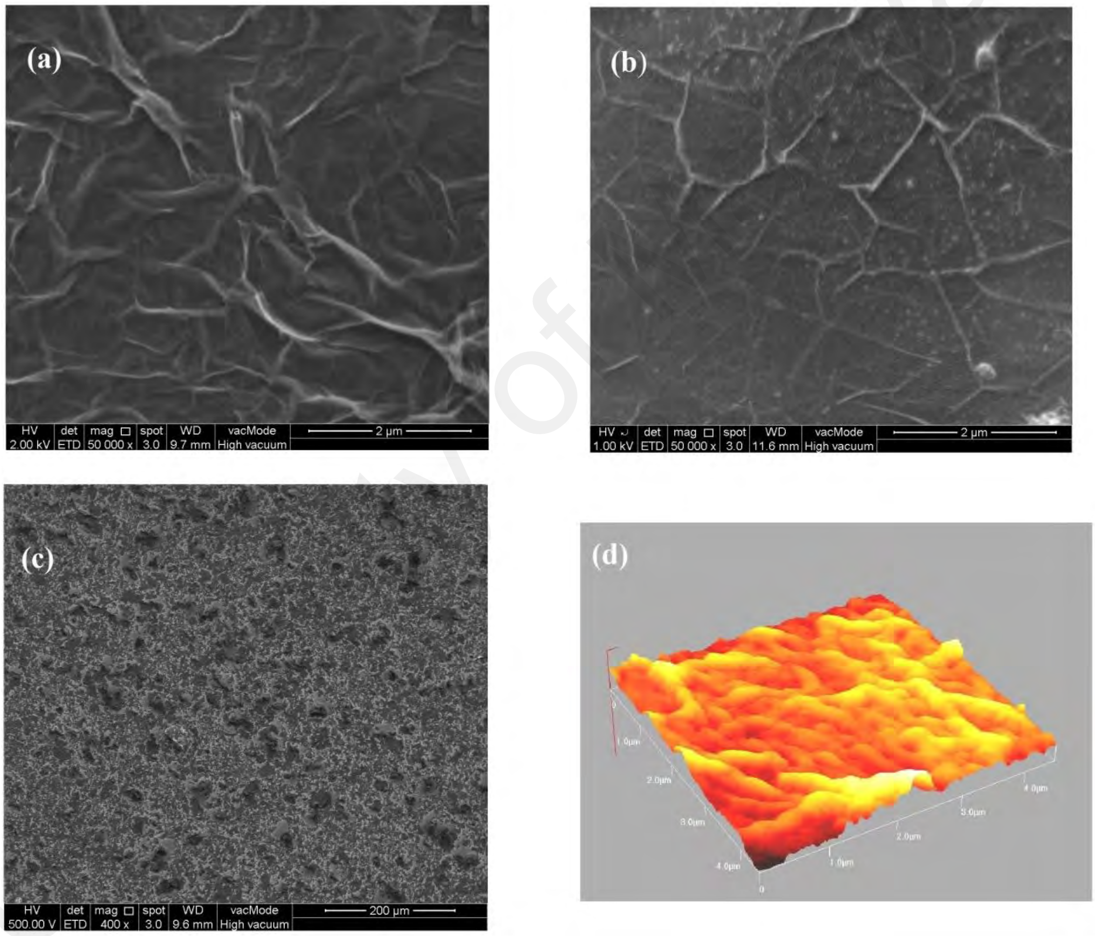

Figure 4.6: FESEM and AFM images of rGO sheet deposited on a glass surface; (a) wrinkle effect of rGO, (b) wrinkle effect after thermal annealing, (c) low magnification of one deposition layer and (d) AFM image of the wrinkle effect with a thickness of 6.18 nm.

4.3 Layer by Layer Deposition

4.3.1 Surface Morphology Analysis

Layer-by-layer deposition using LB technique is capable of producing high porosity rGO films with roughness from nano to macro scales. The average thickness of rGO LB film after one time deposition increased to 89.5 ± 4.43 nm, while the mean roughness of the film was 87.4 nm. Compared to single flakes, the average thickness increases due to patterns of wrinkle at different areas, which could be flat, ripple, standing collapsed, folded, over folded, and scrolled (Zheng et al., 2013). This may affect the average roughness of the sample. The compression of rGO flakes on top of the water will force the flakes to crumble and wrinkle. Upon drying, the wrinkle dimension becomes smaller. The thickness is not only attributed to multilayer deposition, but also due to the wrinkle effect, which increases the thickness as a result of ripple and mountain-like structures on the flakes.

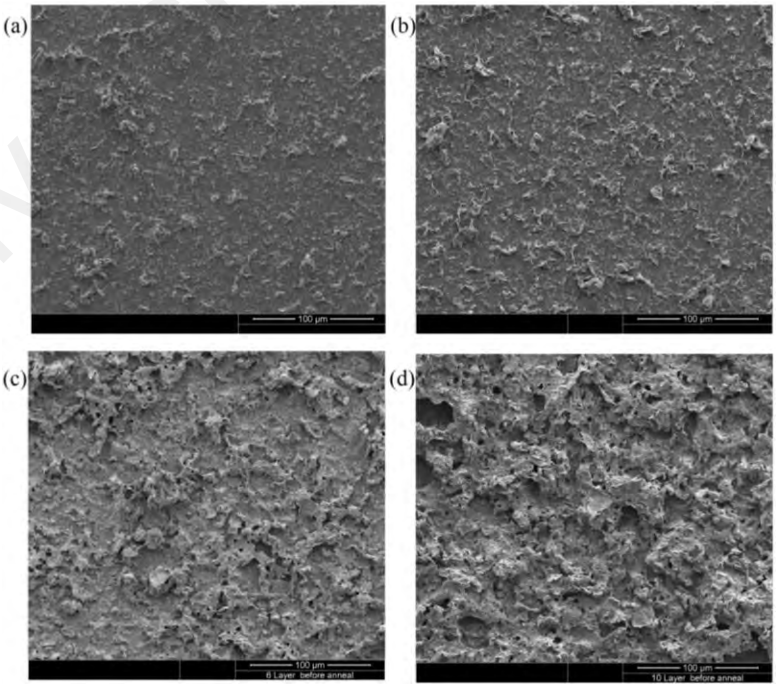

Figure 4.7: The FESEM images of multilayer rGO films show (a) 2, (b) 4, (c) 6, and (d) 10 depositions.

After the second deposition, the roughness and thickness increased to 197.90 and 219.90 ± 13.22 nm, respectively. Surface morphology of the film (Figure 4.7(a)) was observed to be more porous and rougher. Further layers of deposition show quite predictable values, as the slope of the graph, was comparable to each different times of deposition, which shows almost a straight line. As such, it can be concluded that the roughness of each new layer is predictable. Hence, the roughness of the sixth depositions was 489.4 nm with the thickness at (2.24 ± 0.08) µm. For six depositions, micron-scale porous structures could be clearly observed as shown in Figure 4.7(c). This dimension fits various micron-sized biomaterials and organisms such as chloroplast, algae, and most bacteria.

For higher number of layers such as eight deposition layers and above, the porosity reaches sub-micron scale (1.1 µm) with a thickness of (6.40 ± 0.06) µm. For example, 10 layers of deposition are about 1.6 µm. As can be seen in Figure 4.7(d), 10 times deposition of rGO on top of glass shows a bigger value of roughness and porosity in micron-scale (4 µm until > 10 µm). Thus, manipulation of layer-by-layer deposition might be useful for targeting the desired porous and roughness structures for different applications. Overall, thickness values in Figure 4.8 do not follow a linear trend and becomes unpredictable due to over compression of the LB barrier. Even though the barrier compression at a collapsed state was maintained at a constant speed, the control of layer thickness was unpredictable due to different wrinkling mechanism at different times of dipping.

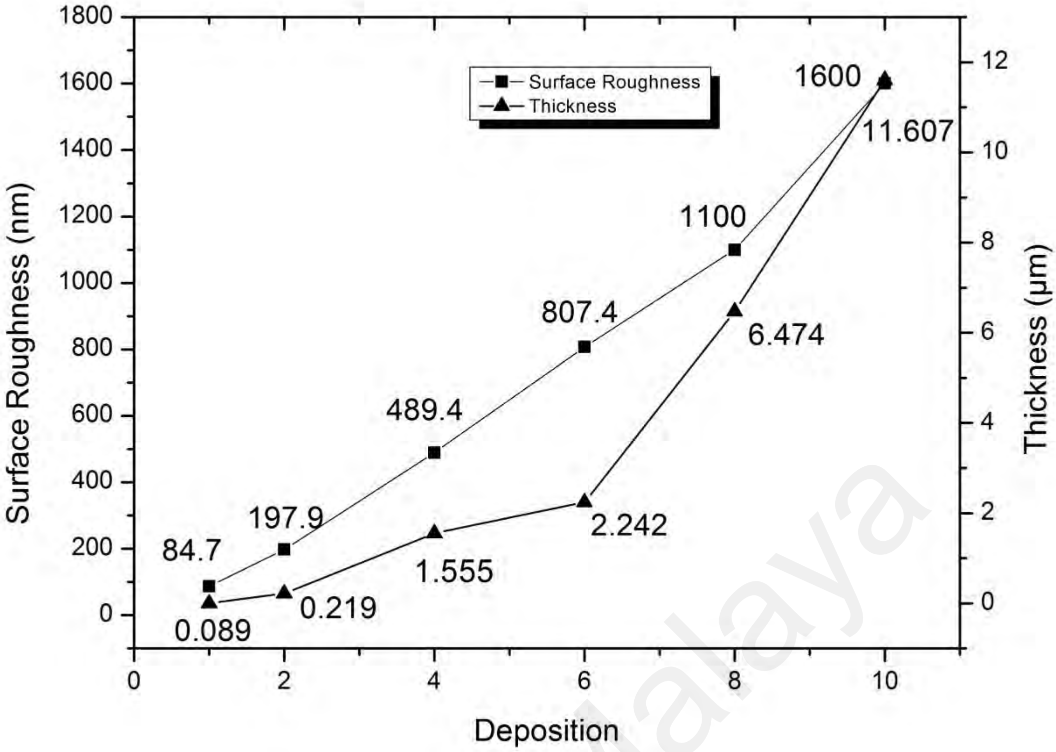

Figure 4.8: Graphs showing a comparison between surface roughness and thickness.

From Figure 4.8, it can be clearly observed that layer-by-layer deposition will increase the surface roughness of the rGO film. The complex 3D structures show interconnected pores, creating microscale cavities suitable for securely harbouring biomaterials within the porous cavities unlike graphene films with relatively 2D smooth surfaces (Li et al., 2013). 2D structures of graphene thin films have narrow bacteria loading capacity and the stacking between individual sheets largely disadvantages the high intrinsic specific area of graphene (Chen et al., 2011). The 3D structures of rGO meanwhile help cellular communication, transportation of oxygen and nutrients, removal of waste, and cellular metabolism more competently than 2D graphene film (Li et al., 2013). Besides that, a lot of evidences suggest that high porosity film platform demonstrates a remarkable positive difference in adhesion and structure for growing biomaterials (Bombelli et al., 2012). Furthermore, for MFC applications, the 3D porous rGO anodes provide a larger surface area to interface with biomaterials compared to the 2D structures. These latter structures may include low specific surface area due to very small pore sizes for bacterial penetration, poor conductivity, disruption of the bacterial membrane or any sharp nanomaterials (Kang et al., 2007). The LB technique employed in this work does not contribute towards such negative influences since in this case; the roughness can be controlled from submicron to micron dimensions. Higher number of depositions, for example, 6 to 10 depositions enable the formation of macro-sized porosity.

4.3.2 Six Deposition of rGO

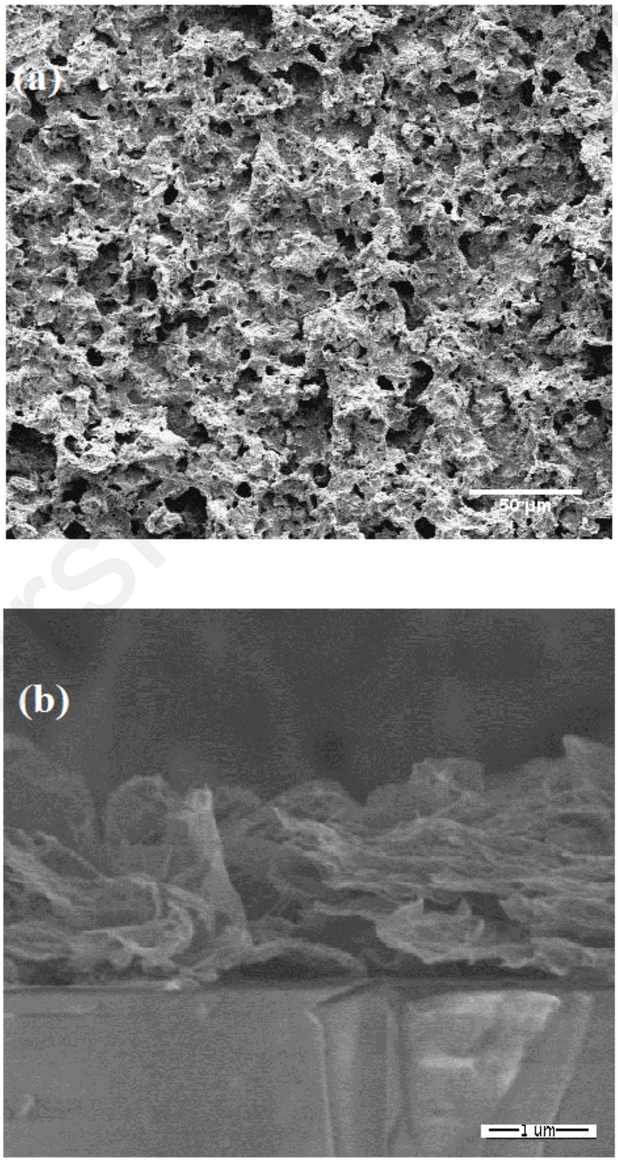

Figure 4.9: The FESEM images at higher magnification of six deposition layers of rGO films (a) and the cross-sectional view of the film (b).

The nature of the porous structure of the six layers of rGO can be clearly observed in Figure 4.9(a). Its shows the 3D surface morphology structure with the porosity measured around 1.207 to 3.810 um with average pore diameter of 2.147 µm (Figure 4.11). These parameters may be the crucial factor for successful encapsulation of the *Chlorella* sp algae or any other biomaterials of similar size (Ng et al., 2014). An analysis of the single pores by AFM measures 2.82 µm x 2.52 µm of diameter with depth of 2.061 µm (Figure 4.10).

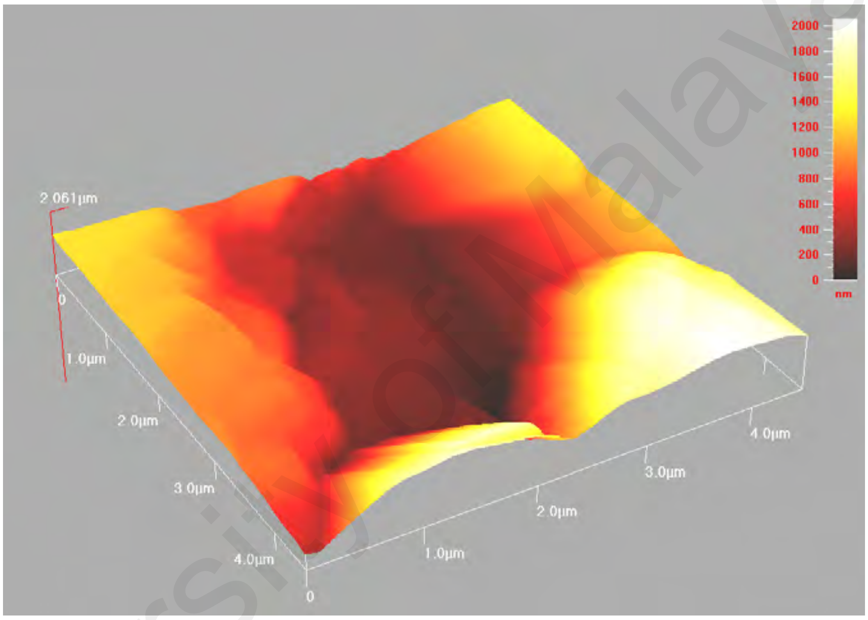

Figure 4.10: AFM image of the single pores from the sixth deposition of rGO LB film.

The image of the surface porosity, roughness, and the cross section of the six deposition rGO LB film from Figure 4.9(a) agrees with the result reported in literature review. Similar observations were observed by Zhang (Zhang et al., 2013), Lili (Jiang et al., 2014) and Jiantong (Li et al., 2013) in describing surface morphology of porous 3D graphene-based materials. The cross-sectional view of graphene foam as reported by Zhiqiang (Niu et al., 2012) also supported the 3D structural view of the rGO LB film (Figure 4.9(b)) prepared in this experiment.

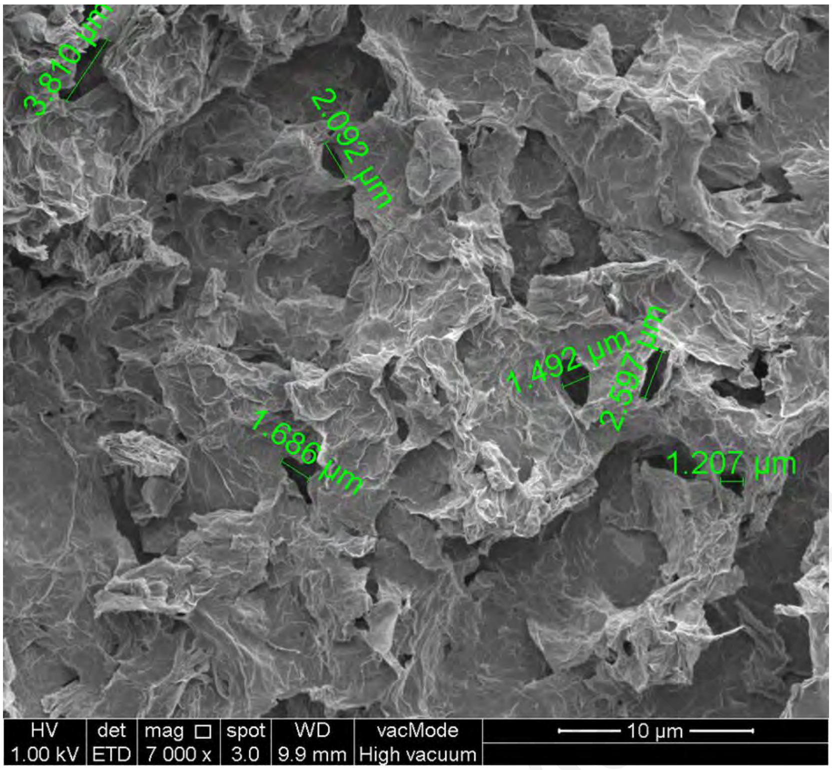

Figure 4.11: FESEM image of highly porous RGO surface in the range of 1.2 to 3.8 µm.

4.4 Optical and Electronic Properties

Comparisons of the slope of the graph in terms of optical and electrical parameters between different numbers of rGO layers demonstrate almost similar patterns (Figure 4.12)). Sheet resistance was improved as the thickness increased but as expected, lowers the optical transmission.

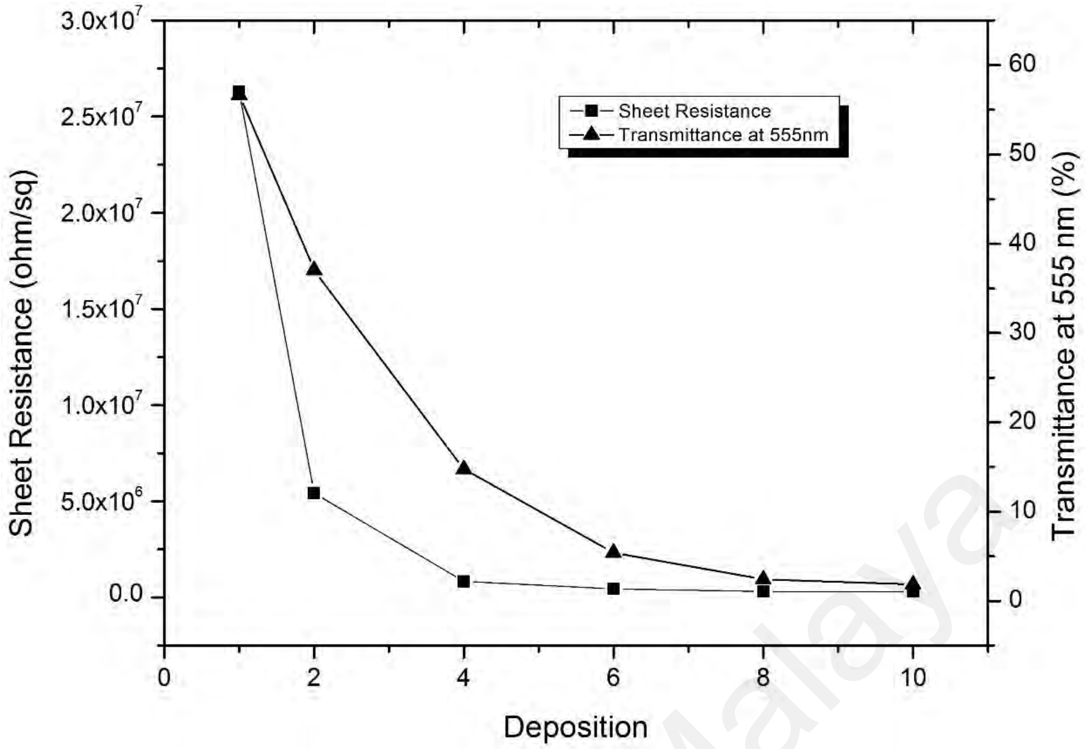

Figure 4.12: Graphs show the comparison of transmittance spectra and sheet resistance for a different time of depositions.

Sheet resistance values of the rGO film were measured in the range of 2.63 x 10^7 to 3.03 x 10^5 Ω/sq for the film thickness of 6.18 to 2700 nm respectively. The presence of functionalized groups in graphene reduced the electron mobility resulting in a more insulating behaviour (Gómez-Navarro et al., 2007). Conductivity was improved by increasing the number of layers. At 87.4 nm, sheet resistance value was 2.63 x 10^7 Ω/sq with 56.66% of transmittance. With a higher number of deposition layers thickness registers increasing sheet resistant and decreasing of transmittance values. A thickness of 555 nm or four layers of deposition, records 438 x 10^6 Ω/sq and 37% corresponding to the thickness and transmittance, respectively.

However for six deposition layers and above, the value of transmittance and sheet resistance were almost saturated. The transmittance values reached 5.4%, while for eight and ten deposition layers it were 2.4% and 1.9%, respectively. Corresponding sheet resistance values for six, eight and ten deposition layers were 4.51 x 10^5, 3.07 x 10^5, and

3.03 x 10^5 Ω/sq, respectively. Due to the deposition at breaking point of the isotherm graph, six deposition layers of the 3D rGO creates pores similar in size to UMACC 313 *Chlorella sp.* algae.

4.5 Surface Chemistry

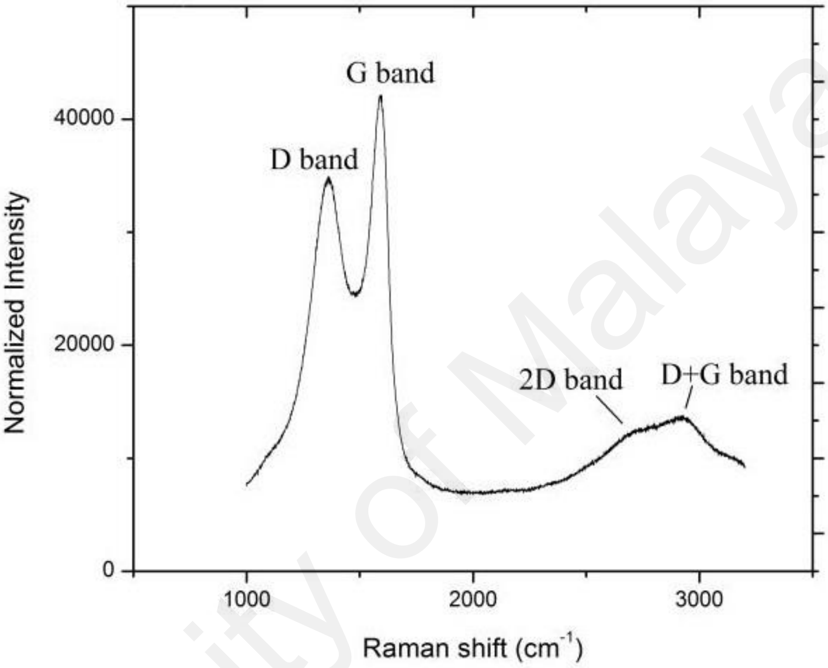

Figure 4.13: The Raman spectra for the deposited rGO film.

Carbon/oxygen ratio of the rGO used in this work according to the manufacturer is 10:5. By using 514 nm wavelength source of the laser in Raman spectroscopy, a typical Raman spectra for rGO was obtained. The G-band of Raman spectra (Figure 4.13) shows the sp2-hybridized carbon-based material. The D-band was stimulated because of participation of the double-resonance Raman scattering near K-point of Brillion zone, indicating the presence of functional groups. The presence of D-band is important because functional groups are needed for detection and attachment of DNA, enzyme, hormone and biomaterial for the colorimetric biosensor. 2D-band is an indicator for crystalline graphitic material and was stimulated because of the π-band in the graphitic electronic structure. Furthermore, the combination peak of D+G was prompted by disorder (Pimenta et al., 2007). From the information provided by Raman spectra, it is agreed that the film is a 2D graphene material with oxide group but maintaining the arrangement of 3D structure as confirmed when viewing the cross-sectional and surface morphology images.

4.6 Electrochemical Properties

This work aims to develop graphene-based novel materials for the assembly of electrodes. The electrodes performance will be improved with active biocatalyst for uses in area of biosensors, as well as for biocathode, biosensor, or bioanodes on biological fuel cells. In line with this aims, it is compulsory to study the electrical characterization and electrochemical properties of the materials that govern the interface between the materials and the electrolyte. The second properties are accountable for the diffusion of species from the bulk solution to the electrolyte surfaces and the succeeding adsorption with the following electrochemistry of these species.

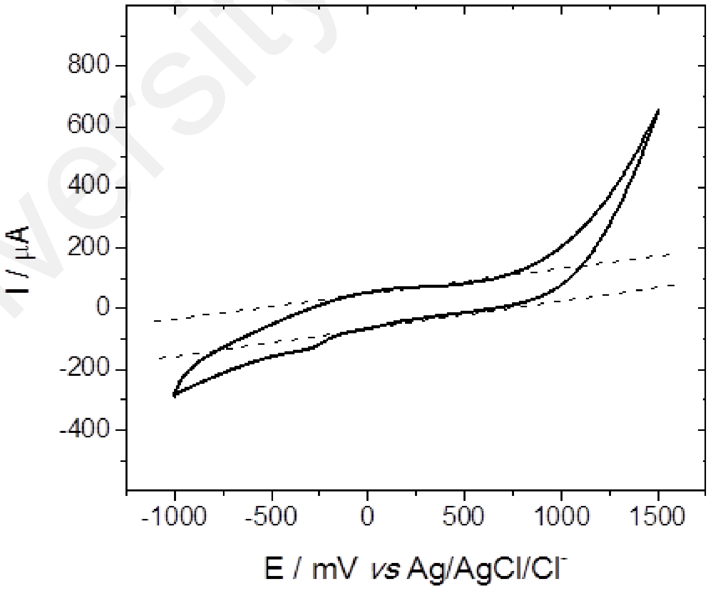

Figure 4.14: Cyclic voltammograms of the 3D rGO in a 0.1 M Potassium phosphate buffer solution at pH 7.0 running at a scan rate of 1 mVs^{-1}

CV profiles were plotted with the 3D rGO film deposited on glass and used as working electrode in the three-electrode electrochemical cell. Ag/AgCl/Cl^- meanwhile was used as the reference electrode and platinum rod as the counter electrode. Six deposition layers were chosen due to the better stability and low resistance compared to the other deposition layers. A pseudo-steady state was reached after the third cycle, which is shown in the shape of the current-potential curve profiles. The 10th cycle was chosen for representation in this experiment. It is because the experimental data show that the shape of the current‒potential curves reaches a pseudo steady state after the 3rd cycle. Figure 4.14 presents results from experiment executed in a very slow scan rate (1 $mV.s^{-1}$). The figure shows that it is possible to spot a quasi-rectangular region (represented as the dashed line) when the potential window was maintained from -100 to 800 mV vs g/AgCl/Cl- electrodes. Furthermore, the figure also shows the distortion in the quasi-rectangular region by the bend in the curve, which results from material electrical resistance. It means that, the region represents that there is no electrochemical reaction that occurs with significant intensity. Also, the dominant effect is the charging of the interfacial double-layer resulting from the adsorption and reorganization of water molecules with charged species present in the electrolyte due to the applied potential.

The measured current, in this circumstance, is intended to be purely capacitive. The symmetrical shape displays characteristics of ideal capacitive behavior. For the development of the biosensors, the best interest region is the potential window at 900 mV where the influence of the materials is minimized. Hence, the acquired signal can be entirely associated to the interaction between the biocatalyst and the analyte of interest. The electrode surface works exclusively as a current collector, or as an electrochemical potential probe. Furthermore, Azhagan et al. suggest that the oxygen groups present at the edges of graphene effect the electric double layer in graphene and similar materials

(Azhagan et al., 2014). These oxygen groups improve the hydrophilicity of the surface in aqueous electrolytes.

From the two extremes outside of this quasi-rectangular region, it is possible to notice the leakage of the current starting from the double layer region, where the potential is high enough for electrochemical reaction to happen. The current acquired, in this case, is considered to be Faradaic. At values of potential around -100 mV *vs* Ag/AgCl/Cl$^-$, it is possible to notice the presence of a first reduction peak. It was demonstrated for a similar condition with electrochemically active rGO, that this Faradaic current is typically associated with the electrochemical oxygen reduction reaction on the surface of rGO. Usually, carbon materials present quinone functional groups that may accountable for the partial reduction involving only two electrons per molecule of oxygen and causing the formation of peroxide. But, the rGO present additional functional groups, such as hydroxyl, carboxylic, and carbonyl groups that may catalyze further reduction of the formed peroxide at more negative potentials (Bikkarolla et al., 2014). The quinone functional group can be described as cyclic array of alternating single and double bonds, example as benzene or naphthalene (Zahid et al., 2010).

Second step for the reduction of the molecular oxygen was observed at potential around -520 mV *vs* Ag/AgCl/Cl$^-$. It is confirmed that the capacity of the 3D rGO to fully reduce the molecular oxygen by a two-step reduction involving two electrons each. The region of the double layers, at the values of potential around 800 mV *vs*Ag/AgCl/Cl$^-$, it is likely to observe the leakage of the current related to a reaction of oxidation occurring on the surface of the 3D rGO. Exponential increase of the Faradaic current, rather than the appearance of a peak-shaped oxidation indicate that this reaction doesn't involve the mass transport of any species present in the solution. Instead, it appears to be related to the oxidation of the material itself or even the oxidation of the solution (electrolysis). Cycle of the 3D rGO does not present any obvious change in this region. It is suggested that the material itself is electrochemically stable and is not consumed or damaged.

Wang et al. showed that this oxidation is associated to a voltage-induced dehydration when using a hydrated GO film as a dielectric spacer for capacitors. This reduces the gap of the GO and assist electron hopping between adjacent GO sheets (Wang et al., 2012). In this experiment, the capacitive current of the hydrated film begin to be partially transformed to resistive current due to the material polarization. This observation recommends that the transport of electrolyte plays a vital role for the electrochemical surface availability and activity of the 3D rGO. For investigating the influence of the electrolyte on the formation of the electrochemical double layer, CV measurements by changing the scan rate and the potential range were accomplished with the 3D rGO. The results obtained were shown in Figure 4.15 and it clearly shows that increasing the scan rate make the CVs of 3D rGO become skewed. This causes the change in the capacitance of the electrochemistry of double layer. This indicates the typical electrochemical behaviour of porous materials (Wang et al., 2014).

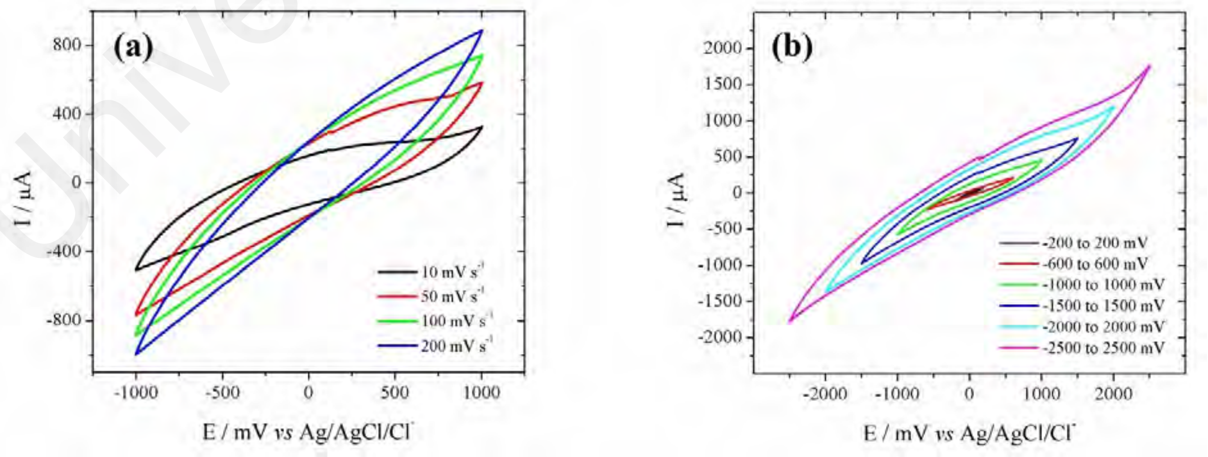

Figure 4.15: Cyclic voltammograms of 3D rGO in 0.1 M potassium phosphate buffer solution (pH 7.0) changing: (a) scan rate and (b) scan size at a fixed scan rate of 10 mV s^{-1}.

Furthermore, at low scan rates (Figure 4.15), ions existing in the solution can easily diffuse into nearly all accessible spaces on the material surface. Meanwhile at high scan rates, ions (mostly cations) can reach only the outer surface of the electrode. Also, material enclosed in the inner space has a smaller influence on the capacitance's behavior, thus deviating from ideal capacitance (Zhu et al., 2012). This mass transport differentiation of the ions present in the solution to the pores cause alterations to the way the double layer is charged. This difference results in the interface of the material to behave as a dielectric interface. This dielectric capacitance behaviour can be artificially made by annealing graphene at high temperatures to help the removal of water molecules from the material interface (Wang et al., 2012).

However, in a different way from what is presented in the literature, our 3D rGO thin film can show the same behaviour as the dielectric but without having the decomposition of oxygen functional groups resulting from the effect of the high-temperature treatment. The high temperature treatment might decrease the lifespan of the electrode. A comparable conclusion can be acquired from Figure 4.15(b), where the increase in the scan size leads to an increase in the concentration of ions at the surface of the electrode resulting in an increase in the dielectric capacitive current. Additionally, the symmetry of the curves, even over a very long range of potentials, from -2.5 to 2.5 V *vs* Ag/AgCl/Cl^- suggests that the charge and discharge of the material occur at a pseudo-constant rate.

These results propose that the developed 3D rGO offers the possibility of application as a material for low-temperature capacitors, where the existence of pores improves the mass transport of materials present in the solution and increases the amount of charges that the material can hold. Furthermore, improved mass transport may increase the amount of substrate to be consumed by biocatalysts immobilized or adsorbed on the 3D rGO surface, leading to the growth of its performance as a bioelectrode for biofuel cells as well as an increase in the sensitivity of the material as a biosensor.

4.7 rGO-Algae and ITO-Algae Bioanode Formation

The following sections (4.7 and 4.8) discusses the collaboration work carried-out with Institute of Ocean and Earth Sciences (IOES), Institute of Biological Sciences, Faculty of Science, University of Malaya and Centre of Research for Electrochemical, Science and Technology (CREST), Department of Chemical Engineering and Biotechnology, University of Cambridge. Furthermore, it also discusses the effectiveness of the rGO film in this work combined with *Chlorella sp*. algae biofilm as anode BPV. The main results of this collaborative research work was published in Scientific Reports by Nature Publishing (Ng et al., 2014).

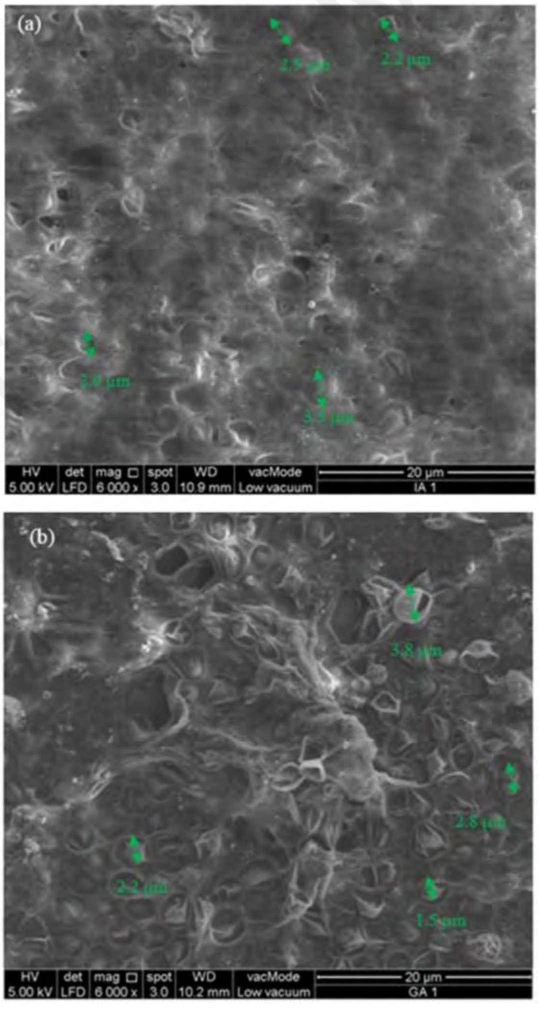

Figure 4.16: FESEM images of *Chlorella sp.* (UMACC 313) biofilms grown on (a) ITO and (b) RGO anodes. The latter image shows high abundance of algae lodged within the correspondingly sized micropores.

FESEM image in Figure 4.16(a) showed the formation of the *Chlorella sp.* from University of Malaya Algae Culture Collection 313 (UMACC 313) on ITO substrate after 15 days of growth. The image reports that the algae size was around 2.0 to 3.5 µm. This information was important for deciding the type of rGO film to be used. Analysis of six deposition of rGO LB assembly shows great potential growing algae on top of it. As shown in recent researches, 3D structure of surface topography such as pore size (Bobyn et al., 1982; Brauker et al., 1995; Singhvi et al., 1994) and surface roughness (Clark et al., 1987) play a vital role in cellular interaction and influence cell behaviour.

The size dimensions can vary from micro to nanometers. Highly porous film of rGO with six deposition layers produced via the LB method created pore sizes between 1.207 - 3.810 µm with average pore diameter of 2.147 µm, fitting well with the dimensions of *Chlorella sp.* used in this work. This will form higher surface area and better attachment of biofilms. The ripple and wrinkle at the surface of 3D rGO improve mechanical interlocking with cells and subsequently improve adhesion with biomaterials and cells (Li et al., 2010).

Furthermore, the presence of the functional groups on the rGO sheets also allows for easier and better attachments of the *Chlorella sp.* to the anode surface due to its superior biocompatibility. As reported by Li et al., the porous structure of rGO could provide 3D microenvironments for cells to be able to resemble their in-vivo counterparts (Li et al., 2013). Compared to 2D graphene-based materials, 3D graphene-based material structure shows more complex structure than smooth 2D films. Hence, communication, transportation of oxygen and nutrients, removal of waste, and cellular metabolism are more efficient with 3D compared to 2D structures of graphene-based film (Li et al., 2013).

4.8 Electrical Study of BPV Device

4.8.1 Polarization Curve

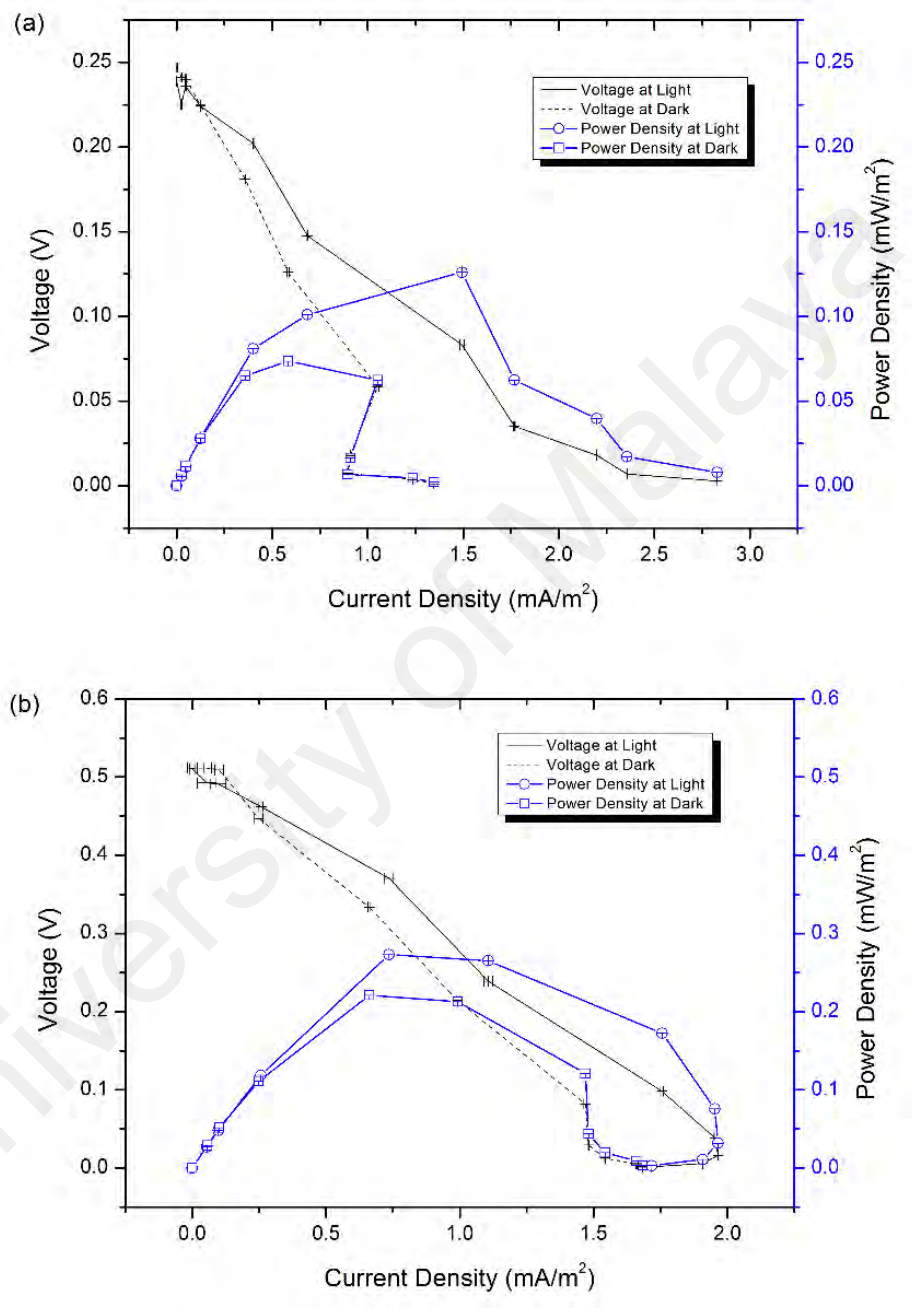

Figure 4.17: Polarization curves for the (a) ITO and (b) RGO based BPV devices.

Figure 4.17 show the polarization curve of ITO and rGO-based BPV devices. During light cycle using ITO-algae anode, maximum current density reaches 2.83 ± 0.1 mA/m^2 and maximum power density was 0.13 ± 0.03 mW/m^2. In the dark cycle, the values obtained was 1.3 ± 0.4 mA/m^2 while the maximum power density was 0.07 ± 0.01 mW/m^2. The open potential result indicates a maximum of 0.239 and 0.247 V corresponding to light and dark cycles, respectively. On the other hand, by using rGO-algae anode BPV devices, the maximum current density reaches until 2.0 ± 0.1 mA/m^2. Maximum power density was increases until 0.27 ± 0.03 mW/m^2 during the light cycle. At the dark cycle, it also shows increasing values of maximum current density with a value of 1.7 ± 0.4 mA/m^2, and 0.21 ± 0.02 mA/m^2 of maximum power density. The open potential demonstrate increasing value of 0.510 V for light cycle, and 0.511 V for the dark cycle. This data displays that the 3D rGO-based device's power density was increased by 118.96% for light cycles, and 189.0% for the dark cycles compared to the traditional ITO anode-based BPV devices.

The factor that influences increasing values of open potential and power density are because of unique properties of 3D structure of the rGO electrodes. Highly porous 3D rGO film enables higher surface area and attachment of the biofilm, which may affect more surface contact between *Chlorella sp.* and the surface of the film. Xie and co-workers employed 3D Carbon Nanotube (CNT)-coated macroporous sponge as the anode and achieved a maximum current density of 10.63 mA cm^{-3}, which is higher than the CNT-textile electrode (Xie et al., 2012). They studies conclude that larger surface area and high conductivity of the 3D electrode providing nearly perfect electrical coupling for ensuring intimate contact between biomolecule and nano to macro electrode surface (Xie et al., 2012). Furthermore, the large surface area of porous 3D rGO film could provide more charge ability than 2D graphene films with the same geometrical area. In contrast, 3D architecture can effectively improve electrical simulation or performance of conductive film (Li et al., 2013). The 3D porous graphene structure is also advantageous for rapid transport of ions, fuel molecules and electrons (Li et al., 2013). Another factor that may affect the remarkable high power density is due to the fact that GO-based electrode materials incorporate unique capabilities for electrical sensing of biological systems due to their inherently abundant functional groups (Fan et al., 2010; Geim et al., 2007; Singh et al., 2014; Wahid et al., 2013; Zuo et al., 2013).

In the event of measuring the power curve for both light and dark cycles, it appears that higher power output was observed during the dark cycle. This might be due to the metabolism of organic substances stored within the algal cells discharged out during the dark phase (Fu et al., 2009; He et al., 2009). In addition, many species of *Chlorella sp.* perform heterotropic nutrition, which may lead to the current production through oxidation of the organic compound (He et al., 2009).

Since the *Chlorella sp.* (UMACC 313) used in this work was isolated from organic palm mill effluent (POME), it would certainly possess heterotrophic abilities. (Phang et al., 1988). *Chlorella* from waste water does exhibit mixtrophic features where organic compound are also metabolized in the presence of light (Ng et al., 2014). In addition, power density from dark to light cycle for both ITO and rGO was observed to increase to about 67% and 120%, respectively. These might be due to the combined contribution of autotrophy (photosynthesis) and mixotrophy processes during current generation (Ng et al., 2014).

CHAPTER 5

CONCLUSIONS AND FUTURE WORKS

5.1 Conclusions

The work carried-out has demonstrated a remarkable improvement in term of its power relative density, which increased to 118.6% and 189.0% in the light and dark conditions, respectively. The key factor is the controllability of the morphological structure of the electrode in the anode compartment using the LB technique. Using this technique, the size of the pores was restructured to around 1.2 to 3.8 µm, which is similar to the dimensions of spherically shaped algae. This enables effective encapsulation of the algae cells within the rGO pores, allowing more surface contact and mass transfer.

This achievement is due to the accomplishment of the three objectives of this thesis. The first is the development of the high porosity rGO film and its characterization. During this stage, we discovered that the roughness of the film could be controlled from nano to micron size due to the layer-by-layer LB deposition technique employed. The other impact is that the controlled size of the roughness led to the formation of optimized pores. For the second objective, we managed to identify the best anode film, which is the anode with six rGO depositions as the pore size correspondingly fits the algae size. For the last objective, we managed to obtain an outstanding result demonstrating that the six depositions of rGO layers have the potential to replace traditional anode materials in BPV platforms. By using Ohm's law, by applying different resistants of 10 MΩ, 5.6 MΩ, 560 kΩ, 240 kΩ, 62 kΩ, 22 kΩ, 9.1 kΩ, 3.3 kΩ, and 1.1 kΩ, a polarization curve was plotted. The results show that by using 3D rGO thin film, the power density was increased to about 0.139 mWm^{-2} in the dark cycle compared to the ITO based BPV device. In the light cycle meanwhile, the power density was increased to about 0.148 mWm^{-2}.

Furthermore, we have invented two new techniques for achieving the best high porosity film. This work has established the unconventional protocol involving dipping mechanism at breaking point instead of dip-coating at solid state. This will allow rGO to stretch and crumble similar to a piece of tissue being crumpled forming 3D characteristics. Due to the repeated dipping process and thermal annealing, different pores and roughness sizes can be formed and controlled. Study of the morphological structures by using FESEM and AFM confirmed this findings.

The other novel technique applied to encounter the problem pertaining to the formation of the clouded areas of the rGO flakes was the methanol vapour assisted process for separating the flakes. This technique is crucial to enable smoother and more desirable monolayer resulting in higher qualities and better re-engineering of the rGO thin film in molecular scale dimensions.

5.2 Future Works

Development of 3D rGO thin film by using LB assembly method has opened-up a lot of potential in biophysics applications. The outcome from this work may provide a future development of renewable energy technology, electrochemical deposition, supercapacitor, medicine, and sensor. Further, the fundamental studies for investigating the interaction between biocatalyst and algae could be performed to study the mass transfer, electron transfer, and electrochemical studies.

Figure 5.1 shows the possible roadmap highlighting the major outcomes that may arise from the current studies reported in this thesis.

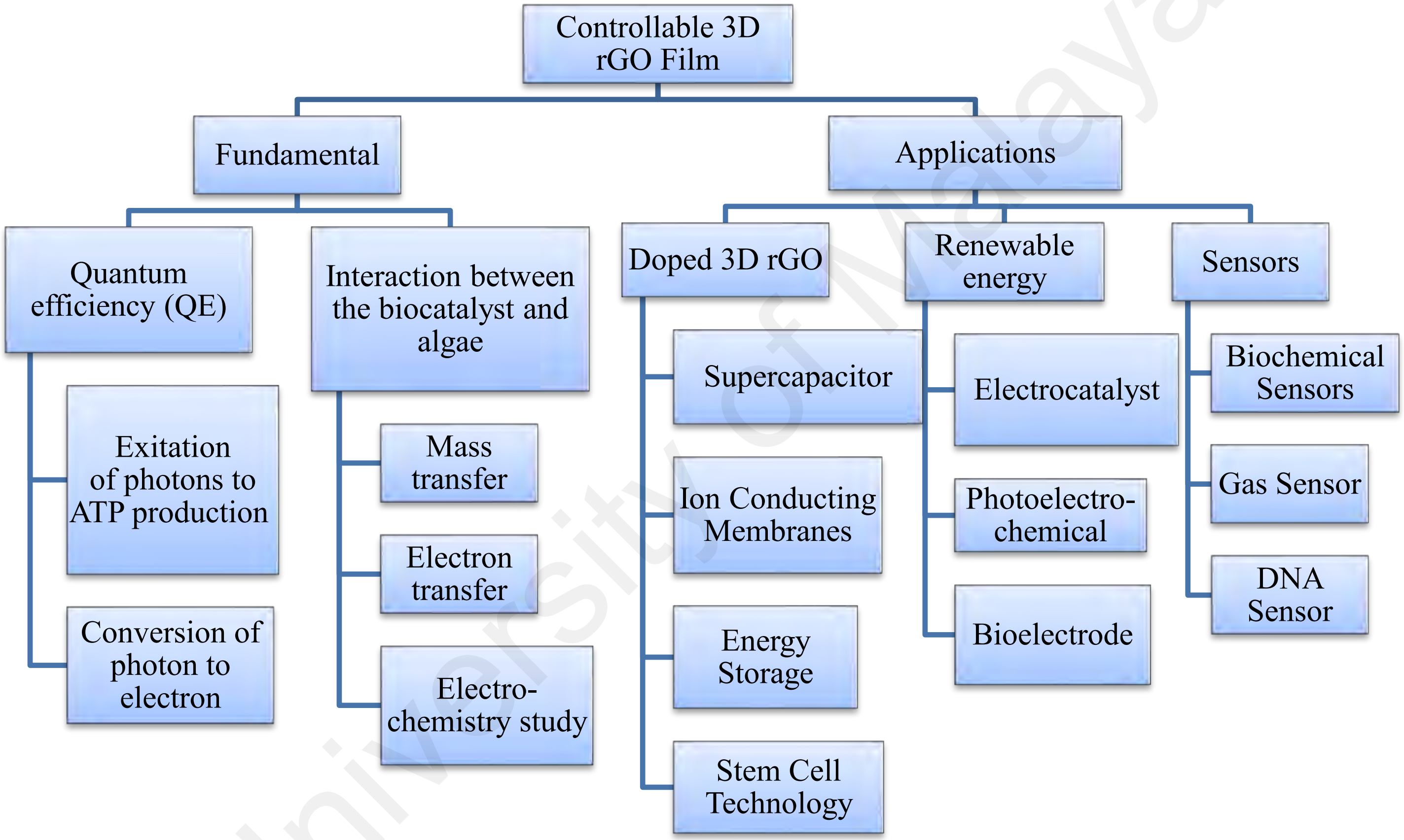

Figure 5.1: Possible outcomes arising from the development of controlled 3D rGO film as demonstrated in our work.

REFERENCES

Almasoud, A. H., & Gandayh, H. M. (2015). Future of solar energy in saudi arabia. *Journal of King Saud University - Engineering Sciences, 27*(2), 153-157.

Antonopoulou, G., Stamatelatou, K., Bebelis, S., & Lyberatos, G. (2010). Electricity generation from synthetic substrates and cheese whey using a two chamber microbial fuel cell. *Biochemical Engineering Journal, 50*(1–2), 10-15.

Atomic-force microscopy (2008). Retrieved 30 December 2016 from https://en.wikipedia.org/wiki/Atomic-force_microscopy

Averill, B., & Eldredge, P. (2013). *General chemistry : Principles, patterns, and applications*. Waashington DC: Saylor Academy

Azhagan, M. V. K., Vaishampayan, M. V., & Shelke, M. V. (2014). Synthesis and electrochemistry of pseudocapacitive multilayer fullerenes and MnO_2 nanocomposites. *Journal of Materials Chemistry A, 2*(7), 2152-2159.

Badwal, S. P. S., Giddey, S. S., Munnings, C., Bhatt, A. I., & Hollenkamp, A. F. (2014). Emerging electrochemical energy conversion and storage technologies. *Frontiers in Chemistry, 2*(79), 1-28.

Bard;, A. J., & Faulkner;, L. R. (2001). *Electrochemical methods: Fundamentals and applications* New York, NY: John Wiley & Son, Inc.

Becerril, H. A., Mao, J., Liu, Z., Stoltenberg, R. M., Bao, Z., & Chen, Y. (2008). Evaluation of solution-processed reduced graphene oxide films as transparent conductors. *ACS Nano, 2*(3), 463-470.

Berk, R. S., & Canfield, J. H. (1964). Bioelectrochemical energy conversion. *Applied Microbiology, 12*, 10-12.

Berker, R., (31 July 2015). *World population expected to reach 9.7 billion by 2050.* Retrieved from http://news.nationalgeographic.com/2015/07/world-population-expected-to-reach-9-7-billion-by-2050/

Bikkarolla, S. K., Cumpson, P., Joseph, P., & Papakonstantinou, P. (2014). Oxygen reduction reaction by electrochemically reduced graphene oxide. *Faraday Discussions, 173*(0), 415-428.

Biochemistry: The chemistry of life (2015). Retrieved 24 Nov 2015 from https://chemistry-batz.wikispaces.com/24+Biochemistry

Biswas, S., & Drzal, L. T. (2009). A novel approach to create a highly ordered monolayer film of graphene nanosheets at the liquid-liquid interface. *Nano Letters, 9*(1), 167-172.

Blodgett, K. B. (1953). Method of forming semiconducting layers on glass and article formed thereby: Google Patents.

Bobyn, J. D., Wilson, G. J., MacGregor, D. C., Pilliar, R. M., & Weatherly, G. C. (1982). Effect of pore size on the peel strength of attachment of fibrous tissue to porous-surfaced implants. *Journal of Biomedical Materials Research, 16*(5), 571-584.

Bombelli, P., Bradley, R. W., Scott, A. M., Philips, A. J., McCormick, A. J., Cruz, S. M., . . . Fisher, A. C. (2011). Quantitative analysis of the factors limiting solar power transduction by synechocystis sp. Pcc 6803 in biological photovoltaic devices. *Energy & Environmental Science, 4*(11), 4690-4698.

Bombelli, P., McCormick, A., Bradley, R., Yunus, K., Philips, J., Anderson, X., . . . Fisher, A. (2011). Harnessing solar energy by bio-photovoltaic (bpv) devices. *Communications in Agricultural and Applied Biological Sciences, 76*(2), 89-91.

Bombelli, P., Zarrouati, M., Thorne, R. J., Schneider, K., Rowden, S. J. L., Ali, A., . . . McCormick, A. J. (2012). Surface morphology and surface energy of anode materials influence power outputs in a multi-channel mediatorless bio-photovoltaic (BPV) system. *Physical Chemistry Chemical Physics, 14*(35), 12221-12229.

Bradley, Robert W., Bombelli, P., Rowden, Stephen J. L., & Howe, Christopher J. (2012). Biological photovoltaics: Intra- and extra-cellular electron transport by cyanobacteria. *Biochemical Society Transactions, 40*(6), 1302.

Brauker, J. H., Carr-Brendel, V. E., Martinson, L. A., Crudele, J., Johnston, W. D., & Johnson, R. C. (1995). Neovascularization of synthetic membranes directed by membrane microarchitecture. *Journal of Biomedical Materials Research, 29*(12), 1517-1524.

Brodie, B. C. (1859). On the atomic weight of graphite. *Philosophical Transactions of the Royal Society of London, 149*, 249-259.

Burnett, D., Barbour, E., & Harrison, G. P. (2014). The UK solar energy resource and the impact of climate change. *Renewable Energy, 71*, 333-343.

Calkins, J. O., Umasankar, Y., O'Neill, H., & Ramasamy, R. P. (2013). High photo-electrochemical activity of thylakoid-carbon nanotube composites for photosynthetic energy conversion. *Energy & Environmental Science, 6*(6), 1891-1900.

Castro Neto, A. H., Guinea, F., Peres, N. M. R., Novoselov, K. S., & Geim, A. K. (2009). The electronic properties of graphene. *Reviews of Modern Physics, 81*(1), 109-162.

Chan, H.-Y., Riffat, S. B., & Zhu, J. (2010). Review of passive solar heating and cooling technologies. *Renewable and Sustainable Energy Reviews, 14*(2), 781-789.

Chandler, D. (2005). Interfaces and the driving force of hydrophobic assembly. *Nature, 437*(7059), 640-647.

Chang, H., Lv, X., Zhang, H., & Li, J. (2010). Quantum dots sensitized graphene: In situ growth and application in photoelectrochemical cells. *Electrochemistry Communications, 12*(3), 483-487.

Chen, D., Feng, H., & Li, J. (2012). Graphene oxide: Preparation, functionalization, and electrochemical applications. *Chemical Reviews, 112*(11), 6027-6053.

Chen, D. M., Shenai, P. M., & Zhao, Y. (2011). Tight binding description on the band gap opening of pyrene-dispersed graphene. *Physical Chemistry Chemical Physics, 13*(4), 1515-1520.

Chen, Z., Ren, W., Gao, L., Liu, B., Pei, S., & Cheng, H.-M. (2011). Three-dimensional flexible and conductive interconnected graphene networks grown by chemical vapour deposition. *Nature Materials, 10*(6), 424-428.

Clark, P., Connolly, P., Curtis, A. S., Dow, J. A., & Wilkinson, C. D. (1987). Topographical control of cell behaviour. I. Simple step cues. *Development, 99*(3), 439-448.

Compton, O. C., & Nguyen, S. T. (2010). Graphene oxide, highly reduced graphene oxide, and graphene: Versatile building blocks for carbon-based materials. *Small, 6*(6), 711-723.

Cooper, D. R., D'Anjou, B., Ghattamaneni, N., Harack, B., Hilke, M., Horth, A., . . . Yu, V. (2012). Experimental review of graphene. *ISRN Condensed Matter Physics, 2012*, 1-56.

Cote, L. J., Kim, F., & Huang, J. X. (2009). Langmuir-blodgett assembly of graphite oxide single layers. *Journal of the American Chemical Society, 131*, 1043-1049.

Darvas, F., Dormán, G., & Hessel, V. (2014). *Flow chemistry*. Berlin: De Gruyter Textbook.

Davis, J. B., & Yarbrough, H. F. (1962). Preliminary experiments on a microbial fuel cell. *Science, 137*(3530), 615.

De, M., Chou, S. S., & Dravid, V. P. (2011). Graphene oxide as an enzyme inhibitor: Modulation of activity of α-Chymotrypsin. *Journal of the American Chemical Society, 133*(44), 17524-17527.

BP P.L.C. (2015) *Bp energy outlook 2015: Growing gas and shifting flows*. London. Dudley, B.

Dürkop, T., Getty, S. A., Cobas, E., & Fuhrer, M. S. (2004). Extraordinary mobility in semiconducting carbon nanotubes. *Nano Letters, 4*(1), 35-39.

Eda, G., Fanchini, G., & Chhowalla, M. (2008). Large-area ultrathin films of reduced graphene oxide as a transparent and flexible electronic material. *Nature Nanotechnology, 3*(5), 270-274.

Eda;, G., & Chhowalla;, M. (2010). Chemically derived graphene oxide: Towards large-area thin film electronics and opto-electronics. *Advanced Materials, 22*(22), 2392-2415.

El Chaar, L., lamont, L. A., & El Zein, N. (2011). Review of photovoltaic technologies. *Renewable and Sustainable Energy Reviews, 15*(5), 2165-2175.

Evans, J. W., Thiel, P. A., & Bartelt, M. C. (2006). Morphological evolution during epitaxial thin film growth: Formation of 2D islands and 3D mounds. *Surface Science Reports, 61*(1–2), 1-128.

Ėvarestov, R. A. (2007). *Quantum chemistry of solids : The lcao first principles treatment of crystals*. Berlin: Springer.

Fan, H., Wang, L., Zhao, K., Li, N., Shi, Z., Ge, Z., & Jin, Z. (2010). Fabrication, mechanical properties, and biocompatibility of graphene-reinforced chitosan composites. *Biomacromolecules, 11*(9), 2345-2351.

Fradkin, E. (1986). Critical behavior of disordered degenerate semiconductors. II. Spectrum and transport properties in mean-field theory. *Physical Review B, 33*(5), 3263-3268.

Frank, I. W., Tanenbaum, D. M., van der Zande, A. M., & McEuen, P. L. (2007). Mechanical properties of suspended graphene sheets. *Journal of Vacuum Science & Technology B, 25*(6), 2558-2561.

Franklin, B., Brownrigg, W., & Farish, M. (1774). Of the stilling of waves by means of oil. Extracted from sundry letters between Benjamin Franklin, ll. D. F. R. S. William Brownrigg, M. D. F. R. S. And the reverend Mr. Farish. *Philosophical Transactions, 64*, 445-460.

Fu, C.-C., Su, C.-H., Hung, T.-C., Hsieh, C.-H., Suryani, D., & Wu, W.-T. (2009). Effects of biomass weight and light intensity on the performance of photosynthetic microbial fuel cells with spirulina platensis. *Bioresource Technology, 100*(18), 4183-4186.

Fuchs, J., (18 June 2013). *What is surface tension?* Retrieved from http://www.ctgclean.com/tech-blog/2013/06/what-is-surface-tension/

Geim, A. K., & Novoselov, K. S. (2007). The rise of graphene. *Nature Materials, 6*(3), 183-191.

Gerster, D., Reichert, J., Bi, H., Barth, J. V., Kaniber, S. M., Holleitner, A. W., . . . Carmeli, I. (2012). Photocurrent of a single photosynthetic protein. *Nature Nanotechnology, 7*(10), 673-676.

Ghasemi, M., Wan Daud, W. R., Ismail, M., Rahimnejad, M., Ismail, A. F., Leong, J. X., . . . Ben Liew, K. (2013). Effect of pre-treatment and biofouling of proton exchange membrane on microbial fuel cell performance. *International Journal of Hydrogen Energy, 38*(13), 5480-5484.

Gibney, E. (2015). The super materials that could trump graphene. *Nature, 522*(7556), 274-276.

Gijs, M. A. M., Scholten, D., van Rooy, T., & Ijsselsteijn, R. (1989). Proximity effect in thin film $Y_1Ba_2Cu_3O_{7-\delta}$ -Ag Pb structures. *Physica C: Superconductivity, 162*, 1615-1616.

Gilgueng, H., Acosta, J. C., Vela, E., Haliyo, S., & Regnier, S. (2009, 21-23 Sept. 2009). *Graphene as thin film infrared optoelectronic sensor.* Paper presented at the Optomechatronic Technologies, 2009. ISOT 2009. International Symposium on Optomechatronic Technologies.

Goki, E., Giovanni, F., & Manish, C. (2008). Large-area ultrathin films of reduced graphene oxide as a transparent and flexible electronic material. *Nature Nanotechnology, 3*, 270-274.

Gómez-Navarro, C., Burghard, M., & Kern, K. (2008). Elastic properties of chemically derived single graphene sheets. *Nano Letters, 8*(7), 2045-2049.

Gómez-Navarro, C., Weitz, R. T., Bittner, A. M., Scolari, M., Mews, A., Burghard, M., & Kern, K. (2007). Electronic transport properties of individual chemically reduced graphene oxide sheets. *Nano Letters, 7*(11), 3499-3503.

Griggs, C. S., & Medina, V. F. (2016). Graphene and graphene oxide membranes for water treatment. In *AccessScience*. McGraw-Hill Education. https://doi.org/10.1036/1097-8542.YB150695.

Haldane, F. D. M. (1988). Model for a quantum hall effect without landau levels: Condensed-matter realization of the "parity anomaly". *Physical Review Letters, 61*(18), 2015-2018.

Hamelers, H. V. M., Heijne, A., Sleutels, T. H. J. A., Jeremiasse, A. W., Strik, D. P. B. T. B., & Buisman, C. J. N. (2009). New applications and performance of bioelectrochemical systems. *Applied Microbiology and Biotechnology, 85*(6), 1673-1685.

He, Q., Wu, S., Gao, S., Cao, X., Yin, Z., Li, H., . . . Zhang, H. (2011). Transparent, flexible, all-reduced graphene oxide thin film transistors. *ACS Nano, 5*(6), 5038-5044.

He, Z., Kan, J., Mansfeld, F., Angenent, L. T., & Nealson, K. H. (2009). Self-sustained phototrophic microbial fuel cells based on the synergistic cooperation between photosynthetic microorganisms and heterotrophic bacteria. *Environmental Science & Technology, 43*(5), 1648-1654.

Hernandez, Y., Nicolosi, V., Lotya, M., Blighe, F. M., Sun, Z., De, S., . . . Coleman, J. N. (2008). High-yield production of graphene by liquid-phase exfoliation of graphite. *Nature Nanotechnology, 3*(9), 563-568.

History of langmuir and langmuir-blodgett films (2014). Retrieved 24 November 2015 from http://www.biolinscientific.com/ksvnima/applications/?card=KA13

Hummers, W. S., & Offeman, R. E. (1958). Preparation of graphitic oxide. *Journal of the American Chemical Society, 80*(6), 1339-1339.

Jeong, H. Y., Kim, J. Y., Kim, J. W., Hwang, J. O., Kim, J.-E., Lee, J. Y., . . . Choi, S.-Y. (2010). Graphene oxide thin films for flexible nonvolatile memory applications. *Nano Letters, 10*(11), 4381-4386.

Jiang, L., & Fan, Z. (2014). Design of advanced porous graphene materials: From graphene nanomesh to 3D architectures. *Nanoscale, 6*(4), 1922-1945.

Jorio, A., Saito, R., Dresselhaus, G., & Dresselhaus, M. S. (2011). The sp^2 nanocarbons: Prototypes for nanoscience and nanotechnology *Raman spectroscopy in graphene related systems* (pp. 1-15): Wiley-VCH Verlag GmbH & Co. KGaA.

Kandilli, C., & Külahlı, G. (2017). Performance analysis of a concentrated solar energy for lighting-power generation combined system based on spectral beam splitting. *Renewable Energy, 101*, 713-727.

Kang, S., Pinault, M., Pfefferle, L. D., & Elimelech, M. (2007). Single-walled carbon nanotubes exhibit strong antimicrobial activity. *Langmuir, 23*(17), 8670-8673.

Kannan, N., & Vakeesan, D. (2016). Solar energy for future world: - A review. *Renewable and Sustainable Energy Reviews, 62*, 1092-1105.

Institute of Southeast Asian Studies. (2008) *Energy for growth: Singapore's national energy policy*. Singapore. Keong, P. K., & Thomson, E.

Kim, F., Cote, L. J., & Huang, J. (2010). Graphene oxide: Surface activity and two-dimensional assembly. *Advanced Materials, 22*(17), 1954-1958.

Kim, K. S., Zhao, Y., Jang, H., Lee, S. Y., Kim, J. M., Kim, K. S., . . . Hong, B. H. (2009). Large-scale pattern growth of graphene films for stretchable transparent electrodes. *Nature, 457*(7230), 706-710.

Kovtyukhova, N. I., Ollivier, P. J., Martin, B. R., Mallouk, T. E., Chizhik, S. A., Buzaneva, E. V., & Gorchinskiy, A. D. (1999). Layer-by-layer assembly of ultrathin composite films from micron-sized graphite oxide sheets and polycations. *Chemistry of Materials, 11*(3), 771-778.

Lake, A., Rezaie, B., & Beyerlein, S. (2017). Review of district heating and cooling systems for a sustainable future. *Renewable and Sustainable Energy Reviews, 67*, 417-425.

Landau, L. D. (1937). Zur theorie der phasenumwandlungen ii. *Phys. Z. Sowjetunion, 11*, 26-35.

Landau, L. D., & Lifshitz, E. M. (1957). *Statistical physic* (Vol. 11). London: Pergamon Press.

Langmuir, I. (1916). The constitution and fundamental properties of solids and liquids. Part I. Solids. *Journal of the American Chemical Society, 38*(11), 2221-2295.

Laughlin, R. G. (1994). *The aqueous phase behavior of surfactants*. London: Academic Press.

Lemme, M. C. (2009, 20 October 2009). *Current status of graphene transistors.* Paper presented at the Solid State Phenomena.

Letchford, K., & Burt, H. (2007). A review of the formation and classification of amphiphilic block copolymer nanoparticulate structures: Micelles, nanospheres, nanocapsules and polymersomes. *European Journal of Pharmaceutics and Biopharmaceutics, 65*(3), 259-269.

Lewis, N. S., & Nocera, D. G. (2006). Powering the planet: Chemical challenges in solar energy utilization. *Proceedings of the National Academy of Sciences, 103*(43), 15729-15735.

Li, D., Muller, M. B., Gilje, S., Kaner, R. B., & Wallace, G. G. (2008). Processable aqueous dispersions of graphene nanosheets. *Nature Nanotechnology, 3*(2), 101-105.

Li, J., & Östling, M. (2013). Prevention of graphene restacking for performance boost of supercapacitors—A review. *Crystals, 3*(1), 163.

Li, M. (2007). Peak oil, the rise of china and india, and the global energy crisis. *Journal of Contemporary Asia, 37*(4), 449-471.

Li, N., Zhang, Q., Gao, S., Song, Q., Huang, R., Wang, L., . . . Cheng, G. (2013). Three-dimensional graphene foam as a biocompatible and conductive scaffold for neural stem cells. *Scientific Reports, 3*, 1604.

Li, X., Cai, W., An, J., Kim, S., Nah, J., Yang, D., . . . Ruoff, R. S. (2009). Large-area synthesis of high-quality and uniform graphene films on copper foils. *Science, 324*(5932), 1312-1314.

Li, X., MacEwan, M. R., Xie, J., Siewe, D., Yuan, X., & Xia, Y. (2010). Fabrication of density gradients of biodegradable polymer microparticles and their use in guiding neurite outgrowth. *Advanced Functional Materials, 20*(10), 1632-1637.

Li, X., Zhang, G., Bai, X., Sun, X., Wang, X., Wang, E., & Dai, H. (2008). Highly conducting graphene sheets and langmuir-blodgett films. *Nature Nanotechnology, 3*(9), 538-542.

Liu, B., Sun, Z., Zhang, X., & Liu, J. (2013). Mechanisms of DNA sensing on graphene oxide. *Analytical Chemistry, 85*(16), 7987-7993.

Liu, M., Steven Tay, N. H., Bell, S., Belusko, M., Jacob, R., Will, G., . . . Bruno, F. (2016). Review on concentrating solar power plants and new developments in high temperature thermal energy storage technologies. *Renewable and Sustainable Energy Reviews, 53*, 1411-1432.

Liu, S.-J., Wen, Q., Tang, L.-J., & Jiang, J.-H. (2012). Phospholipid–graphene nanoassembly as a fluorescence biosensor for sensitive detection of phospholipase D activity. *Analytical Chemistry, 84*(14), 5944-5950.

Logan, B. E. (2009). Exoelectrogenic bacteria that power microbial fuel cells. *Nature Reviews Microbiology, 7*(5), 375-381.

Logan, B. E., Hamelers, B., Rozendal, R., Schröder, U., Keller, J., Freguia, S., . . . Rabaey, K. (2006). Microbial fuel cells: Methodology and technology. *Environmental Science & Technology, 40*(17), 5181-5192.

Lovley, D. R. (2011). Live wires: Direct extracellular electron exchange for bioenergy and the bioremediation of energy-related contamination. *Energy & Environmental Science, 4*(12), 4896-4906.

Luo, H., Xu, P., Jenkins, P. E., & Ren, Z. (2012). Ionic composition and transport mechanisms in microbial desalination cells. *Journal of Membrane Science, 409–410*, 16-23.

Mao, L., & Verwoerd, W. S. (2013). Selection of organisms for systems biology study of microbial electricity generation: A review. *International Journal of Energy and Environmental Engineering, 4*(1), 1-18.

Mazzio, K. A., & Luscombe, C. K. (2015). The future of organic photovoltaics. *Chemical Society Reviews, 44*(1), 78-90.

McCormick, A. J., Bombelli, P., Bradley, R. W., Thorne, R., Wenzel, T., & Howe, C. J. (2015). Biophotovoltaics: Oxygenic photosynthetic organisms in the world of bioelectrochemical systems. *Energy & Environmental Science, 8*(4), 1092-1109.

Mermin, N. D. (1968). Crystalline order in two dimensions. *Physical Review, 176*(1), 250-254.

Mugnier, D., Fedrizzi, R., Thygesen, R., & Selke, T. (2015). New generation solar cooling and heating systems with IEA SHC task 53: Overview and first results. *Energy Procedia, 70*, 470-473.

Najafpour, G., Rahimnejad, M., & Ghoreshi, A. (2011). The enhancement of a microbial fuel cell for electrical output using mediators and oxidizing agents. *Energy Sources, Part A: Recovery, Utilization and Environmental Effects, 33*(24), 2239-2248.

Ng, F.-L., Jaafar, M. M., Phang, S.-M., Chan, Z., Salleh, N. A., Azmi, S. Z., . . . Periasamy, V. (2014). Reduced graphene oxide anodes for potential application in algae biophotovoltaic platforms. *Scientific Reports, 4*, 7562.

Niu, Z., Chen, J., Hng, H. H., Ma, J., & Chen, X. (2012). A leavening strategy to prepare reduced graphene oxide foams. *Advanced Materials, 24*(30), 4144-4150.

Novoselov, K. S., Geim, A. K., Morozov, S. V., Jiang, D., Katsnelson, M. I., Grigorieva, I. V., . . . Firsov, A. A. (2005). Two-dimensional gas of massless dirac fermions in graphene. *Nature, 438*(7065), 197-200.

Novoselov, K. S., Geim, A. K., Morozov, S. V., Jiang, D., Zhang, Y., Dubonos, S. V., . . . Firsov, A. A. (2004). Electric field effect in atomically thin carbon films. *Science, 306*(5696), 666-669.

Novoselov, K. S., Jiang, D., Schedin, F., Booth, T. J., Khotkevich, V. V., Morozov, S. V., & Geim, A. K. (2005). Two-dimensional atomic crystals. *Proceedings of the National Academy of Sciences of the United States of America, 102*(30), 10451-10453.

Osman, M. H., Shah, A. A., & Walsh, F. C. (2011). Recent progress and continuing challenges in bio-fuel cells. Part I: Enzymatic cells. *Biosensors and Bioelectronics, 26*(7), 3087-3102.

Pant, D., Singh, A., Van Bogaert, G., Irving Olsen, S., Singh Nigam, P., Diels, L., & Vanbroekhoven, K. (2012). Bioelectrochemical systems (BES) for sustainable energy production and product recovery from organic wastes and industrial wastewaters. *RSC Advances, 2*(4), 1248-1263.

Parida, B., Iniyan, S., & Goic, R. (2011). A review of solar photovoltaic technologies. *Renewable and Sustainable Energy Reviews, 15*(3), 1625-1636.

Park, S., & Ruoff, R. S. (2009). Chemical methods for the production of graphenes. *Nature Nanotechnology, 4*(4), 217-224.

Peierls, R. E. (1935). Quelques propriétés typiques des corps solides. *Annales de l'institut Henri Poincaré, 5*, 177-222.

Periasamy, V. (2012). Mechanical and thermodynamic properties of chlorophyll-A surfactants at air-water interface. *Advanced Materials Research, 535-537*, 1119-1125.

Petty, M. C. (1996). *Langmuir-blodgett films : An introduction*. Cambridge, United Kingdom: Cambridge University Press.

Phang, S.-M., & Kim-Chong, O. (1988). Algal biomass production in digested palm oil mill effluent. *Biological Wastes, 25*(3), 177-191.

Pimenta, M. A., Dresselhaus, G., Dresselhaus, M. S., Cancado, L. G., Jorio, A., & Saito, R. (2007). Studying disorder in graphite-based systems by raman spectroscopy. *Physical Chemistry Chemical Physics, 9*(11), 1276-1290.

Ping, Q., Cohen, B., Dosoretz, C., & He, Z. (2013). Long-term investigation of fouling of cation and anion exchange membranes in microbial desalination cells. *Desalination, 325*, 48-55.

Pockels, A. (1891). Suface tension. *Nature, 43*, 437-439.

Potter, M. C. (1911). Electrical effects accompanying the decomposition of organic compounds. *Proceedings of the Royal Society of London B: Biological Sciences, 84*(571), 260-276.

Rahimnejad, M. (2011). Effect of mass transfer on performance of microbial fuel cell. *Mass Transfer in Chemical Engineering Processes, 5*, 233-250.

Rambaut, M., & Vigier, J. P. (1989). The simultaneous existence of Em Grassmann-Lorentz forces (acting on charged particles) and Ampère forces (acting on charged conducting elements) does not contradict relativity theory. *Physics Letters A, 142*(8), 447-452.

Rao, J. R., Richter, G. J., Von Sturm, F., & Weidlich, E. (1976). The performance of glucose electrodes and the characteristics of different biofuel cell constructions. *Bioelectrochemistry and Bioenergetics, 3*(1), 139-150.

Rasuli, R., Iraji Zad, A., & Ahadian, M. M. (2010). Mechanical properties of graphene cantilever from atomic force microscopy and density functional theory. *Nanotechnology, 21*(18), 185503.

Reina, A., Jia, X. T., Ho, J., Nezich, D., Son, H. B., Bulovic, V., . . . Kong, J. (2009). Layer area, few-layer graphene films on arbitrary substrates by chemical vapor deposition. *Nano Letters, 9*(8), 3087-3087.

Rosenbaum, M. A., & Henrich, A. W. (2014). Engineering microbial electrocatalysis for chemical and fuel production. *Current Opinion in Biotechnology, 29*, 93-98.

Sauer, K., Rickard, A., & Davies, D. (2007). Biofilms and biocomplexity. *Microbe Magazine, 2*, 347-353.

Schedin, F., Geim, A. K., Morozov, S. V., Hill, E. W., Blake, P., Katsnelson, M. I., & Novoselov, K. S. (2007). Detection of individual gas molecules adsorbed on graphene. *Nature Materials, 6*(9), 652-655.

Schwartz, D. K. (1997). Langmuir-blodgett film structure. *Surface Science Reports, 27*(7–8), 245-334.

Semenoff, G. W. (1984). Condensed-matter simulation of a three-dimensional anomaly. *Physical Review Letters, 53*(26), 2449-2452.

Shao, Y., Wang, J., Wu, H., Liu, J., Aksay, I. A., & Lin, Y. (2010). Graphene based electrochemical sensors and biosensors: A review. *Electroanalysis, 22*(10), 1027-1036.

Sharma, Y., & Li, B. (2010). The variation of power generation with organic substrates in single-chamber microbial fuel cells (SCMFCs). *Bioresource Technology, 101*(6), 1844-1850.

Sheka, E. F. (2014). The uniqueness of physical and chemical natures of graphene: Their coherence and conflicts. *International Journal of Quantum Chemistry, 114*(16), 1079-1095.

Sindhu, S., Nehra, V., & Luthra, S. (2016). Solar energy deployment for sustainable future of india: Hybrid SWOC-AHP analysis. *Renewable and Sustainable Energy Reviews*.

Singh, G., Botcha, V. D., Sutar, D. S., Narayanam, P. K., Talwar, S. S., Srinivasa, R. S., & Major, S. S. (2014). Near room temperature reduction of graphene oxide langmuir-blodgett monolayers by hydrogen plasma. *Physical Chemistry Chemical Physics, 16*(23), 11708-11718.

Singhvi, R., Stephanopoulos, G., & Wang, D. I. (1994). Effects of substratum morphology on cell physiology. *Biotechnology and Bioengineering 43*(8), 764-771.

Sluiter, M. H. F., & Kawazoe, Y. (2003). Cluster expansion method for adsorption: Application to hydrogen chemisorption on graphene. *Physical Review B, 68*(8), 085410.

Sovacool, B. K. (2010). A critical evaluation of nuclear power and renewable electricity in asia. *Journal of Contemporary Asia, 40*(3), 369-400.

Strik, D. P. B. T. B., Timmers, R. A., Helder, M., Steinbusch, K. J. J., Hamelers, H. V. M., & Buisman, C. J. N. (2011). Microbial solar cells: Applying photosynthetic and electrochemically active organisms. *Trends in Biotechnology, 29*(1), 41-49.

Tan, X., Feng, L., Zhang, J., Yang, K., Zhang, S., Liu, Z., & Peng, R. (2013). Functionalization of graphene oxide generates a unique interface for selective serum protein interactions. *ACS Applied Materials & Interfaces, 5*(4), 1370-1377.

Tloughran, T., (15 September 2011). *The scanning electron microscope.* Retrieved from https://sjhsrc.wikispaces.com/Week+of+Sep+15

Torres, C. (2012). Improving microbial fuel cells. *Membrane Technology, 2012*(8), 8-9.

Tuersun, P., Han, X. e., & Ren, K. F. (2015). Backscattering properties of gold nanoshells: Quantitative analysis and optimization for biological imaging. *Procedia Engineering, 102*, 1511-1519.

Ultraviolet–visible spectroscopy (2005). Retrieved 30 December 2016 from https://en.wikipedia.org/wiki/Ultraviolet–visible_spectroscopy

Venables, J. A., Spiller, G. D. T., & Hanbucken, M. (1984). Nucleation and growth of thin films. *Reports on Progress in Physics, 47*(4), 399.

Vieira de Souza, L. E., & Gilmanova Cavalcante, A. M. (2016). Concentrated solar power deployment in emerging economies: The cases of China and Brazil. *Renewable and Sustainable Energy Reviews*.

Wahid, M. H., Eroglu, E., Chen, X., Smith, S. M., & Raston, C. L. (2013). Entrapment of chlorella vulgaris cells within graphene oxide layers. *RSC Advances, 3*(22), 8180-8183.

Wallace, P. R. (1947). The band theory of graphite. *Physical Review, 71*(9), 622-634.

Wang, D.-W., Du, A., Taran, E., Lu, G. Q., & Gentle, I. R. (2012). A water-dielectric capacitor using hydrated graphene oxide film. *Journal of Materials Chemistry, 22*(39), 21085-21091.

Wang, H., Leonard, S. L., & Hu, Y. H. (2012). Promoting effect of graphene on dye-sensitized solar cells. *Industrial & Engineering Chemistry Research, 51*(32), 10613-10620.

Wang, S., Hsia, B., Carraro, C., & Maboudian, R. (2014). High-performance all solid-state micro-supercapacitor based on patterned photoresist-derived porous carbon electrodes and an ionogel electrolyte. *Journal of Materials Chemistry A, 2*(21), 7997-8002.

Wang, X., Zhi, L., & Mullen, K. (2008). Transparent, conductive graphene electrodes for dye-sensitized solar cells. *Nano Letters, 8*(1), 323-327.

Wang, Y.-X., Fan, W.-X., Wang, G.-L., & Ji, M.-X. (2011). New insight into the graphene based films prepared from carbon fibers. *Materials Sciences and Application,, 2*, 834-838.

Wang, Y., Wan, Y., & Zhang, D. (2010). Reduced graphene sheets modified glassy carbon electrode for electrocatalytic oxidation of hydrazine in alkaline media. *Electrochemistry Communications, 12*(2), 187-190.

Watcharotone, S., Dikin, D. A., Stankovich, S., Piner, R., Jung, I., Dommett, G. H., . . . Ruoff, R. S. (2007). Graphene-silica composite thin films as transparent conductors. *Nano Letters, 7*(7), 1888-1892.

Wen, X., Garland, C. W., Hwa, T., Kardar, M., Kokufuta, E., Li, Y., . . . Tanaka, T. (1992). Crumpled and collapsed conformation in graphite oxide membranes. *Nature, 355*(6359), 426-428.

Xie, X., Ye, M., Hu, L., Liu, N., McDonough, J. R., Chen, W., . . . Cui, Y. (2012). Carbon nanotube-coated macroporous sponge for microbial fuel cell electrodes. *Energy & Environmental Science, 5*(1), 5265-5270.

Xiuyi, L., Jingjing, J., Yousefi, N., Xi, S., & Jang-Kyo, K. (2012, 13-16 Dec. 2012). *Highly transparent conducting graphene films produced by langmuir blodgett assembly as flexible electrodes.* Paper presented at the Electronic Materials and Packaging (EMAP), 2012 14th International Conference on Electronic Materials and Packaging (EMAP).

Yang, J., & Gunasekaran, S. (2013). Electrochemically reduced graphene oxide sheets for use in high performance supercapacitors. *Carbon, 51*(0), 36-44.

Yang, Y., Yang, X., Yang, W., Li, S., Xu, J., & Jiang, Y. (2014). Ordered and ultrathin reduced graphene oxide LB films as hole injection layers for organic light-emitting diode. *Nanoscale Research Letters, 9*(1).

Yehezkeli, O., Tel-Vered, R., Wasserman, J., Trifonov, A., Michaeli, D., Nechushtai, R., & Willner, I. (2012). Integrated photosystem ii-based photo-bioelectrochemical cells. *Nature Communications, 3*, 742.

Zahid, M., Saeed, M., Rogan, E. G., & Cavalieri, E. L. (2010). Benzene and dopamine catechol quinones could initiate cancer or neurogenic disease. *Free Radical Biology & Medicine, 48*(2), 318-324.

Zambari, I. F., Hui, C. Y., & Mohamed, R. (2013). Development of wireless energy transfer module for solar energy harvesting. *Procedia Technology, 11*, 882-894.

Zhang, L., Zhang, F., Yang, X., Long, G., Wu, Y., Zhang, T., . . . Chen, Y. (2013). Porous 3D graphene-based bulk materials with exceptional high surface area and excellent conductivity for supercapacitors. *Scientific Reports, 3*, 1408.

Zhang, Y., Tan, Y.-W., Stormer, H. L., & Kim, P. (2005). Experimental observation of the quantum hall effect and berry's phase in graphene. *Nature, 438*(7065), 201-204.

Zheng, Q.-b., Shi, L.-f., & Yang, J.-h. (2012). Langmuir-blodgett assembly of ultra-large graphene oxide films for transparent electrodes. *Transactions of Nonferrous Metals Society of China, 22*(10), 2504-2511.

Zheng, Q., Ip, W. H., Lin, X., Yousefi, N., Yeung, K. K., Li, Z., & Kim, J.-K. (2011). Transparent conductive films consisting of ultralarge graphene sheets produced by langmuir–blodgett assembly. *ACS Nano, 5*(7), 6039-6051.

Zheng, Q., Shi, L., Ma, P.-C., Xue, Q., Li, J., Tang, Z., & Yang, J. (2013). Structure control of ultra-large graphene oxide sheets by the langmuir-blodgett method. *RSC Advances, 3*(14), 4680-4691.

Zhu, J., & He, J. (2012). Facile synthesis of graphene-wrapped honeycomb MnO_2 nanospheres and their application in supercapacitors. *ACS Applied Materials & Interfaces, 4*(3), 1770-1776.

Zhu, Y. W., Cai, W. W., Piner, R. D., Velamakanni, A., & Ruoff, R. S. (2009). Transparent self-assembled films of reduced graphene oxide platelets. *Applied Physics Letters, 95*(10), 103104.

Zhu;, Y., Murali;, S., Cai;, W., Li;, X., Suk;, J. W., Potts;, J. R., & Ruoff;, R. S. (2010). Graphene and graphene oxide: Synthesis, properties, and applications. *Advanced Materials, 22*(35), 3906–3924.

Zuo, P.-P., Feng, H.-F., Xu, Z.-Z., Zhang, L.-F., Zhang, Y.-L., Xia, W., & Zhang, W.-Q. (2013). Fabrication of biocompatible and mechanically reinforced graphene oxide-chitosan nanocomposite films. *Chemistry Central Journal, 7*(1), 1-11.

LIST OF PUBLICATIONS AND PATENT

1. Fong-Lee Ng, **Muhammad Musoddiq Jaafar**, Siew-Moi Phang, Zhijian Chan, Nurul Anati Salleh, Siti Zulfikriyah Azmi, Kamran Yunus, Adrian C. Fisher, Vengadesh Periasamy, "Reduced Graphene Oxide Anodes for Potential Application in Algae Biophotovoltaic Platforms," *Scientific Reports***,** vol. 4, p. 7562, 2014.
2. **M. Musoddiq Jaafar**, Gustavo P.M.K. Ciniciato. S. Aisyah Ibrahim, S.M. Phang, K. Yunus, Adrian C Fisher, M. Iwamoto, P. Vengadesh, "Preparation of Three-Dimensional Reduced Graphene Oxide Layers by using Langmuir-Blodgett Method", *Langmuir*, 2015, 31 (38), 10426–10434
3. G. P. M. K. Ciniciato, Fong-Lee Ng, S.M. Phang, **Muhammad Musoddiq Jaafar**, Adrian C. Fisher, K. Yunus, P. Vengadesh, "Investigating the association between photosynthetic efficiency and generation of biophotoelectricity in autotrophic microbial fuel cells" *Scientific Reports*, 2016, vol. 6, p. 3119, 2016.
4. Method of Fabricating Graphene-based Algal Biofilm Electrode for Application in a Biophotovoltaic Device, Vengadesh Periasamy, Phang Siew Moi, Ng Fong Lee, **Muhammad Musoddiq**, Adrian C. Fisher, Kamran Yunus. Application number: PI 2014703632

LIST OF CONFERENCES

1. **M. Musoddiq**, Vengadesh P., "Mechanical and Thermodynamics Properties of Reduced Graphene Oxide at Air-Water Interface", National Physics Conference (PERFIK 2014), 18-19 November 2014, Sunway Resort Hotel & Spa, Kuala Lumpur, Malaysia
2. Siti Aisyah Ibrahim, Fong-Lee Ng, **Muhammad Musoddiq Jaafar**, Kamran Yunus, Adrian C. Fisher, Siew-Moi Phang, Vengadesh Periasamy, "Characterization of Annealing Temperatures for Surface Functionalization of Reduced Graphene Oxide (rGO) Anodic Film for Improved Biophotovoltaics (BPV) Applications", National Physics Conference (PERFIK 2014), 18-19 November 2014, Sunway Resort Hotel & Spa, Kuala Lumpur, Malaysia

LIST OF AWARDS

1. Silver Medal for International Innovation, Design and Articulation 2013, 28-30 May 2013, UiTM Perlis, Perlis, Malaysia.
2. Bronze Medal for International Innovation, Design and Articulation 2014, 16-19 September 2014, UiTM Perlis, Perlis, Malaysia.
3. Silver Medal for Bioinnovation Asia Awards, 2014, 19-21 November 2014, KLCC, Kuala Lumpur, Malaysia
4. Bronze Medal for PENCIPTA 2015, 4-6 December 2015, KLCC, Kuala Lumpur, Malaysia